ANNALS OF GEOPHYSICS, 69, 4, GP, 2026; doi:10.4401/ag-9413
OPEN ACCESS

# Corrections for anomalous crustal magnetic field determined from magnetic observatory data

Anatoly Soloviev[1,2], Mikhail Nanov[*,1], Dmitriy Kudin[1]

(1) Geophysical Center of the Russian Academy of Sciences, Moscow, Russian Federation
(2) Schmidt Institute of Physics of the Earth of the Russian Academy of Sciences, Moscow, Russian Federation

Article history: received August 20, 2025; accepted June 3, 2026

## Abstract

The magnetic field of the Earth's crust provides essential information about the geological features of a region, its origin, and the spatial and temporal characteristics of the total magnetic field. Numerical estimation and consideration of the contribution of the crustal field are a necessary step in constructing accurate models of the secular variation of the main magnetic field of the Earth based on observatory data. To accurately determine the corrections for the crustal field at the locations of magnetic observatories, we apply an algorithm to process the original observatory data, which allows us to define all three orthogonal components of the crustal magnetic field vector. To assess the reliability of the obtained values, a modified standard deviation $\sigma'$ is proposed, which depends on the data series length and involves statistical indicators from long-term observation series of the benchmark observatories. As a result, updated corrections were obtained for 118 observatories using data over 1998-2025. For 65 observatories, such data are published for the first time. For the remaining observatories, the results were compared with previously acquired values. For some components and observatories, the deviations exceed $3\sigma'$, which confirms the need for regular updating the contribution of the Earth's crustal field at magnetic observatories. The results obtained also made it possible to assess the accuracy of existing models of the crustal field.

Keywords: Crustal magnetic field; Magnetic observatories; Observatory bias; Magnetic anomalies; Data processing

## 1. Introduction

The magnetic field measured at any point on the Earth's surface is a superposition of several magnetic contributions generated by different sources. The dominant part of the observed magnetic field is the main Earth's magnetic field (EMF), which is internal in origin and is caused by electric currents in the Earth's liquid outer core. This part of the field varies on time scales from several months to decades and longer. The field of the Earth's crust, which is associated with the remanent and induced magnetization of rocks, is also of internal origin (Merrill et al., 1998). Its value generally varies from fractions of nT to hundreds of nT, but in some regions it reaches values of several thousand nT. External fields are caused by ionospheric and magnetospheric current systems. The values of these fields on the Earth's surface during periods of reduced magnetic activity are several tens of nT, and during magnetic storms and related processes they can reach several thousand nT. External fields change over time with periods from fractions of a second to 11 years, which constitutes a half-period of a full solar cycle (Jacobs, 1987; Gvishiani and Soloviev, 2020).

For accurate determination of the main EMF signal and its time variations, data from low-orbit satellite observations and ground-based stationary magnetic observatories located around the world are used. Modern standards of magnetic observatory data are maintained by INTERMAGNET network (https://intermagnet.org). The institutions from around the world that joined this consortium developed an infrastructure for data exchange and management, as well as methods for data processing and verification (Love, Chulliat, 2013). Obviously, when extracting the signal of the main EMF from observatory data, the contributions of other sources must be determined and taken into account as accurately as possible. Note that the error in determining the signal of the main EMF without correction due to the contribution of the magnetic field of the Earth's crust can exceed 10%, which is unacceptable for determining its secular variation and using such data to build the corresponding analytical models of the EMF.

In recent years, two different methods have been used to determine the crustal field corrections in observatory data. One is to directly estimate the corrections as additional unknowns during the inversion of observatory and satellite data when adjusting the coefficients for the spherical harmonic model of the EMF (Langel et al., 1982; Sabaka et al., 2002). Another method is to compare the values of magnetic field components measured at observatories with the values according to the model of the main EMF based on satellite data solely (e.g., Gubbins and Bloxham, 1985; Bloxham and Gubbins, 1986). Most of the published corrections are tied to specific epochs and were calculated based on satellite data for one or more months (Mandea and Langlais, 2002). However, some researchers have also studied the time variations of corrections for observatories over long periods and compared their annual averages with models that span different epochs (Verbanac et al., 2007, 2015). In this paper we use the latter approach.

It is evident that the accuracy of crustal field corrections depends on the duration of continuous vector recordings available at an observatory. This raises the problem of estimating the reliability of the obtained values for different lengths of original observation series. Herein, we analyze the reliability of the crustal field determination depending on the length of the data used and the variability of the cumulative values of its components. For this purpose, we introduce a modified standard deviation (MSD) $\sigma'$, which depends on the data series length and involves statistical indicators based on long-term observation series from benchmark observatories. This approach enables accurate estimation of corrections when data are available only for a short period of time. We show that using the standard deviation to evaluate the reliability of the derived crustal field corrections is often inadequate. This is because even refined data contain complex, hardly accountable signals associated with seasonal solar activity, as well as the 11-year solar cycle. The analysis also reveals that for observatories located in the polar regions high latitude phenomena significantly distort the data and inhibits a reliable estimation of the anomalous crustal field corrections using the methodology outlined by Califf et al. (2022).

Using data over 1998-2025 from 118 observatories, we analyze monthly means separately for three orthogonal components of the crustal magnetic field vector: $X_a$ (Northern), $Y_a$ (Eastern), and $Z_a$ (vertical), as well as for the anomalous declination $D_a$. The temporal changes in the corrections are estimated on time scales from several months (short-term variations) to decades (long-term trends). We believe that long-term trends are likely to be of internal origin and related to changes in crustal magnetization or induction effects in lithospheric conductivity anomalies. Short-term variations are likely related to the unaccounted contribution of external fields. The influence of different solar cycle phases on the correction values for observatories is also studied. The second part of the paper compares the obtained results with the corrections for the anomalous crustal field calculated earlier, and presents new results for those magnetic observatories, the data of which have not been analyzed before. The discrepancies between the obtained corrections and the data on magnetic anomalies according to existing models and digital maps are also estimated.

## 2. Theoretical foundations

As is known, the geomagnetic field $\mathbf{B}_{\mathrm{obs}}$ at any given time at the geographic location of an observatory can be represented as a vector sum:

$$\mathbf{B}_{\mathrm{obs}} = \mathbf{B}_{\mathrm{m}} + \mathbf{B}_{\mathrm{c,\,rem}} + \mathbf{B}_{\mathrm{c,\,ind}} + \mathbf{B}_{\mathrm{e}} + \mathbf{B}_{\mathrm{err}}, \tag{1}$$

where
$\mathbf{B}_m$ – main field,
$\mathbf{B}_{c,\,rem}$ – remanent field of the Earth's crust,
$\mathbf{B}_{c,\,ind}$ – induced field of the Earth's crust of both internal and external origin,
$\mathbf{B}_e$ – external field,
$\mathbf{B}_{err}$ – other contributions that contain any possible errors.

Since it is difficult to distinguish between the remanent and induced crustal field (Lesur and Gubbins, 2000), we consider the sum $\mathbf{B}_{c,\,rem} + \mathbf{B}_{c,\,ind}$ as the desired anomalous crustal field $\mathbf{B}_a$.

Let us determine the bias in observatory data $\mathbf{B}_{bias}$

$$\mathbf{B}_{bias} = \mathbf{B}_a + \varepsilon, \tag{2}$$

where $\varepsilon$ comprises the influence of the external field and the error in the input data ($\varepsilon = \mathbf{B}_e + \mathbf{B}_{err}$).

We assume that the contamination of both the external and crustal fields is minimized in the models of the main EMF obtained from satellite data. Taking this into account, the biases in the data of the three components at the observatory ($X_{bias}$, $Y_{bias}$, $Z_{bias}$) can be calculated as the differences between the component values measured at the given observatory ($X_{obs}$, $Y_{obs}$, $Z_{obs}$) and the model main field values at the location of this observatory ($X_m$, $Y_m$, $Z_m$).

To study the temporal variability of both bias terms given in (2), we apply the following steps. First, the mean bias value for each observatory is calculated over the period of study (1998-2025) and the temporal variations around this value are analyzed. Two different types of such temporal variations are possible: a short-term oscillatory behavior and a long-term trend around the mean bias. In this study we assume that $\mathbf{B}_a$ does not change noticeably during the time interval under consideration (Sebera et al., 2019). Thus, our purpose is to exclude all types of variations from observatory records. In this case, the mean bias is a good approximation of the crustal field over 28 years of study, and the short-term oscillating variation around the mean bias corresponds to $\varepsilon$. The long term variation suggests that $\mathbf{B}_a$ has indeed changed over the period under study, as the time-varying core field produces also a time-varying lithospheric field by induction (Sebera et al., 2019). Then the sum of the average bias and the long-term trend in the variation relative to this average will be a representative estimate of the crustal field. In this case, the variations relative to the crustal field that remain after subtraction of average bias of the trend correspond to $\varepsilon$. Then there is the possibility of studying the long-term trend of $\varepsilon$ associated with the phases of the solar cycle, as well as the remaining short-term variations of $\varepsilon$ associated with the external field.

## 3. Initial data

The fundamental material in this study are the hourly means of definitive and quasi-definitive data provided by magnetic observatories. Both standards are regulated by a global network of magnetic observatories INTERMAGNET, which provides the highest quality of EMF observations (Love and Chulliat, 2013; Bracke, 2025). Both types of data are time series of complete values of the three components of the magnetic induction vector ($X$, $Y$, $Z$), cleared of artificial disturbances (including effects from electrified structures and metal constructions) and baseline adjusted. Each value has a time reference in the UTC system. The definitive data, officially approved and published on the INTERMAGNET website (http://intermagnet.org), become available with a delay of more than a year. Quasi-definitive data are vector field measurements corrected using temporary baselines immediately after registration. According to the INTERMAGNET protocol, their discrepancy with the definitive data should not exceed 5 nT (Peltier and Chulliat, 2010). At the same time, the delay in the provision of such data should not exceed three months, but for some observatories it actually does not exceed 1 month. Today, only a quarter of the observatories of the INTERMAGNET global network are capable of producing satisfactory quasi-definitive data, which are extremely valuable for solving a number of scientific problems (construction of operational models and study of rapid variations of the main EMF, calculation of geomagnetic activity indices, etc.) (Khomutov, 2025). In the Russian segment of the observatory network, the accelerated preparation of quasi-definitive data is largely supported by the MAGNUS hardware-software system, which is the core of the Interregional Analytical Geomagnetic Data Center (http://mag.gcras.ru/). In particular, this system provides almost automated recognition of man-made disturbances in data coming from observatories

(Kudin et al., 2021) and temperature correction of vector magnetometer records (Kudin et al., 2023). It significantly facilitates data checking and validation, which are carried out manually by an expert at the final stage of definitive data preparation. However, even definitive data may contain jumps caused, for example, by magnetometer displacement. Apparently, such jumps introduce distortions when calculating corrections. Therefore, for all observatories under consideration, we manually select the longest data periods without jumps.

To exclude the influence of external fields, we select observatory data recorded during low geomagnetic activity periods according to space weather parameters. They include the values of the planetary Kp index of geomagnetic activity, the RC index of the intensity of magnetospheric ring current (Karinen and Mursula, 2005) and data on the interplanetary magnetic field (IMF). The Kp index characterizes the global disturbance of the geomagnetic field due to space weather events in a three-hour time range on a scale from 0 to 9 and is calculated based on data from 13 magnetic observatories located in the subauroral zone of the Northern and Southern hemispheres (Bartels et al., 1939; Gvishiani and Soloviev, 2020). The RC index is calculated based on global measurements of the horizontal component of the geomagnetic field from a network of observatories located at low and mid-latitudes. It reflects the contribution of the ring current to geomagnetic field disturbances, similar to the Dst index, but with a higher time resolution (1 minute). RC index is much more consistent with direct observations of the ring current effect made by the CHAMP satellite than Dst index, and it is widely used in development of current geomagnetic field models (Olsen et al., 2014; Onovughe, 2018). From the IMF parameters we use the values of its most geoeffective components *By* (azimuthal in the ecliptic plane) and *Bz* (perpendicular to the ecliptic plane).

To calculate the values of the components of the main EMF for the considered period of observatory data (1998-2023), we use the CHAOS-8.2 model (Finlay et al., 2020). The CHAOS family models have been developed at the Technical University of Denmark (DTU Space) since 2005. The model is built primarily on the basis of satellite (Oersted, CHAMP, SAC-C and Swarm) and observatory (160 observatories) monthly means and represents a solution of the full inverse problem. This means that the parameters defined in the model describe different sources contributing to the measured EMF values, including sources located inside the Earth in the liquid core and lithosphere, as well as large scale magnetospheric field. The maximum degree of the polynomials describing large-scale internal sources is $N = 90$. The model describes the EMF for the period from 1997 to 2025. In the time-dependent part, polynomials with degrees $n$ from 1 to 20 are used. Unlike other models of the main EMF, which have a time step from 1 to 5 years, the CHAOS model has a time resolution of 1 month.

To assess the discrepancies between the obtained corrections and previously reported data on the anomalous crustal field at the locations of the observatories, we analyze existing grids of magnetic anomalies for certain epochs and model values of the components of the crustal magnetic field vector. The first are digital global maps of magnetic anomalies WDMAM 2.2 for 1990 (Lesur et al., 2016) (hereinafter WDMAM), EMAG2v3 for 2000 (Meyer et al., 2017) (hereinafter EMAG) and the map of anomalies of the former USSR territory for 1965 compiled by VSEGEI (Ivanov et al., 1957) (hereinafter VSEGEI). These maps provide gridded $\Delta T$ values, which are essentially the difference between the measured total field intensity and that predicted by a core magnetic field model adjusted for diurnal variations. The WDMAM map is plotted with a 3 arc-minute resolution at an altitude of 5 km above the WGS84 ellipsoid for the continental part and at an altitude of 0 km for the maritime regions. The EMAG map is plotted with a 2 arc-minute resolution at an altitude of 4 km above the WGS84 ellipsoid for the continental part and at an altitude of 0 km for the maritime regions. The VSEGEI historical map is constructed at an altitude of 400 m and has a spatial resolution of 2.5 arc minutes.

The model values of the components of the crustal magnetic field vector are derived using the model by Thébault et al., (2021) (hereinafter The1050), the model underlying the construction of WDMAM digital map (hereinafter WDMAM model), the model xDLFI (Thébault and Hulot, 2025) (hereinafter xDLFI) and the model EMM2017 based on the latest release of the EMAG2v3 grid (hereinafter EMM2017). The degree and order of expansion of The1050 model are 1050, which corresponds to a spatial resolution of about 10 arc minutes. The degree and order of expansion of the WDMAM model are 800, which provides a spatial resolution of about 14 arc minutes. The degree and order of expansion of the xDLFI model are 1500, which provides a spatial resolution of about 7 arc minutes. The degree and order of expansion of the EMM2017 model are 790, which provides a spatial resolution of about 14 arc minutes.

# 4. Method for extracting crustal magnetic field signal from observatory data

As stated above, to extract the signal of the crustal magnetic field from the geomagnetic observations at the magnetic observatory, it is necessary to eliminate the contributions of the main and external fields. To eliminate the contribution of the main EMF from the obtained hourly means, we subtract the model values of the three components for the corresponding UT time stamps at the geographic location of the observatory, calculated using the CHAOS model. In the model, we use the expansion of the geomagnetic potential into spherical harmonics up to the 15$^{th}$ degree and order, which corresponds to the spectrum of the main EMF. The CHAOS family model also allows us to take into account the contribution of large-scale near and far magnetic fields of the magnetosphere. For convenience, the values obtained by subtracting these three contributions will be called the residual field.

To eliminate unaccounted disturbances caused by external sources, the values obtained during magnetically quiet time periods are selected from the hourly means of the residual field. Data selection is carried out according to approach suggested by Califf et al. (2022), in compliance with the following criteria:

1) local time in the range from 01:00 to 05:00;
2) planetary Kp-index less than 3;
3) the rate of change of the RC index |dRC/dt| does not exceed 4 nT/h;
4) the value of the Bz component of the IMF in the range from 0 to 6 nT;
5) the value of the By component of the IMF in the range from –6 to 6 nT.

Next, for those days in the UTC system in which the residual field values remained as a result of the selection, their daily means are calculated, followed by monthly means derivation. At the final stage, the median for each component of the magnetic field is calculated based on the monthly means for the entire period under consideration. We attribute the annual period of variations in the $\varepsilon$ component to the seasonal contribution of the external field, caused by the Earth's rotation around the Sun. Other signals that contribute to $\varepsilon$ and are superimposed on the dominant signal of external fields are related to possible noise in the original data. These oscillations in the residual magnetic field are almost regular. This allows us to conclude that the derived median values reliably estimate the local contributions of the anomalous crustal field $\mathbf{B}_\mathrm{a}$ to the observatory recordings at a given point.

Estimation of the correction for the anomalous declination of the crustal magnetic field, which is the angle between the vectors of the total internal (main + crustal) and main fields, also is of great practical value. Based on the horizontal components of the anomalous crustal field Ba and the main field Bm from the CHAOS-8.2 model, we derive Da as

$$D_a = \arccos\left(\frac{\mathbf{B}_m^{XY} \cdot \mathbf{B}_t^{XY}}{|\mathbf{B}_m^{XY}||\mathbf{B}_t^{XY}|}\right),$$

where $\mathbf{B}_m^{XY}$ are the CHAOS-8.2 values given for 2025.0 epoch at observatory location, $\mathbf{B}_t^{XY} = \mathbf{B}_m^{XY} + \mathbf{B}_a^{XY}$. Since the value $D_a$ is calculated using the vector dot product, it does not indicate the direction of the deviation (i.e., east or west).

Indeed, even a weak anomalous crustal magnetic field can lead to a large anomaly in declination $D_a$ (several degrees) depending on its direction in the horizontal plane *XY*. This is shown schematically in Fig. 1a. Failure to take into account a large correction for the anomalous declination can lead to significant errors in navigation tasks based on observations of the total EMF.

Next, we estimate the accuracy of the derived crustal field corrections for each component. We calculate unnormalized nonparametric skew as the modulus of the difference between the mean and the median in order to estimate errors in nanotesla according to INTERMAGNET quality standards (Bracke, 2025). A preliminary analysis of the root mean square (RMS) and unnormalized nonparametric skew shows a statistically significant difference (>5 nT) starting from 60° quasi-dipole geomagnetic latitude (QD latitude) in both hemispheres (see Fig. 2). This is because the data processing methodology does not account for electromagnetic processes typical for high latitudes, which lead to data distortion. Therefore, to obtain reliable results we limit the analysis to data from 118 observatories located at QD latitudes less than 60 degrees in both hemispheres. Of these, we select benchmark observatories with continuous data series exceeding 11 years, i.e. one solar cycle, spanning all the considered latitudes. Based on these data, we calculate the anomalous crustal field values sequentially over periods starting from 27 days up to 11 years with an increment of 27 days. Figure 3 shows that adding more data reduces seasonal and 11-year variations in the crustal field components and stabilizes its derivation. Long-term drift observed in the $Y_a$ component has an amplitude smaller than 1 nT and we attribute it to modeling uncertainty. We consider the values obtained over the entire 11-year period (and longer) true, and calculate the absolute errors for all other values obtained over shorter periods. We use the envelope of these errors as a function of the observation period to construct the reliability parameter, which we call the modified standard deviation (MSD, $\sigma'$):

$$MSD(T < 11\ years) = \sqrt{O(T)^2 + \sigma^2}, \quad O(T) = \max_{i=1,\dots n_{ben}} O_i^{ben}(T), \tag{3}$$

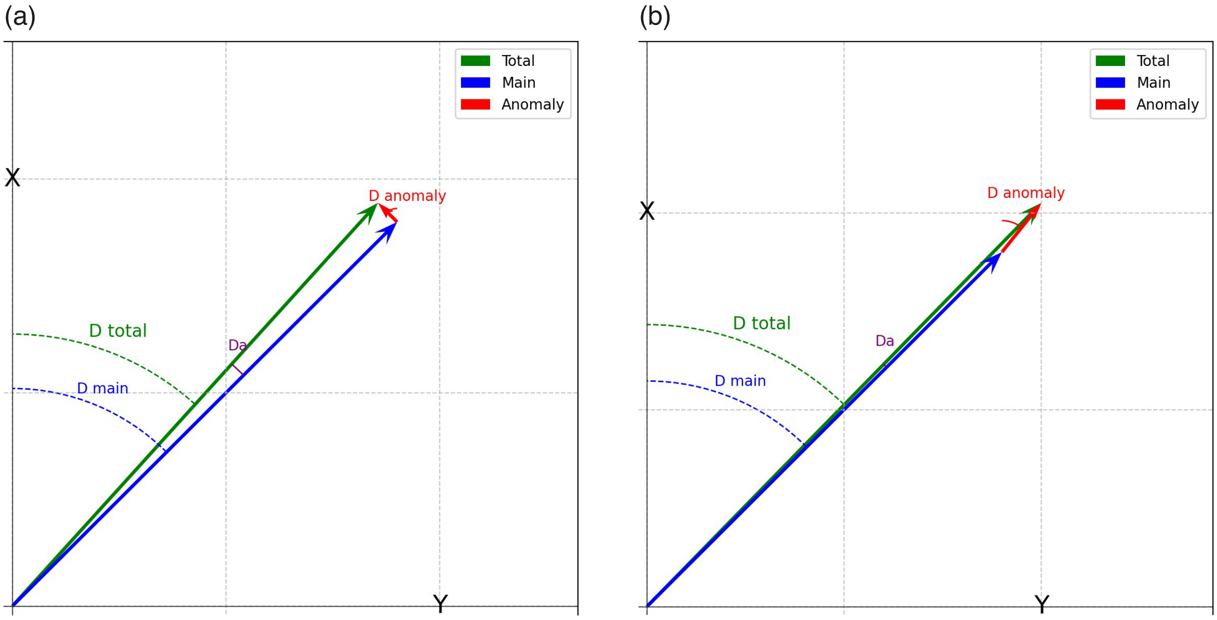


**Figure 1.** Schematic illustration of the contribution of the anomalous crustal field vector $\mathbf{B}_a$ to the declination anomaly $D_a$ due to its direction and length in the $XY$ plane: with a small length of $\mathbf{B}_a$ and its non-colinearity with $\mathbf{B}_m$, the declination $D_a$ is significant (a), with a large length of $\mathbf{B}_a$ and its colinearity with $\mathbf{B}_m$, the declination $D_a$ is minimal (b).

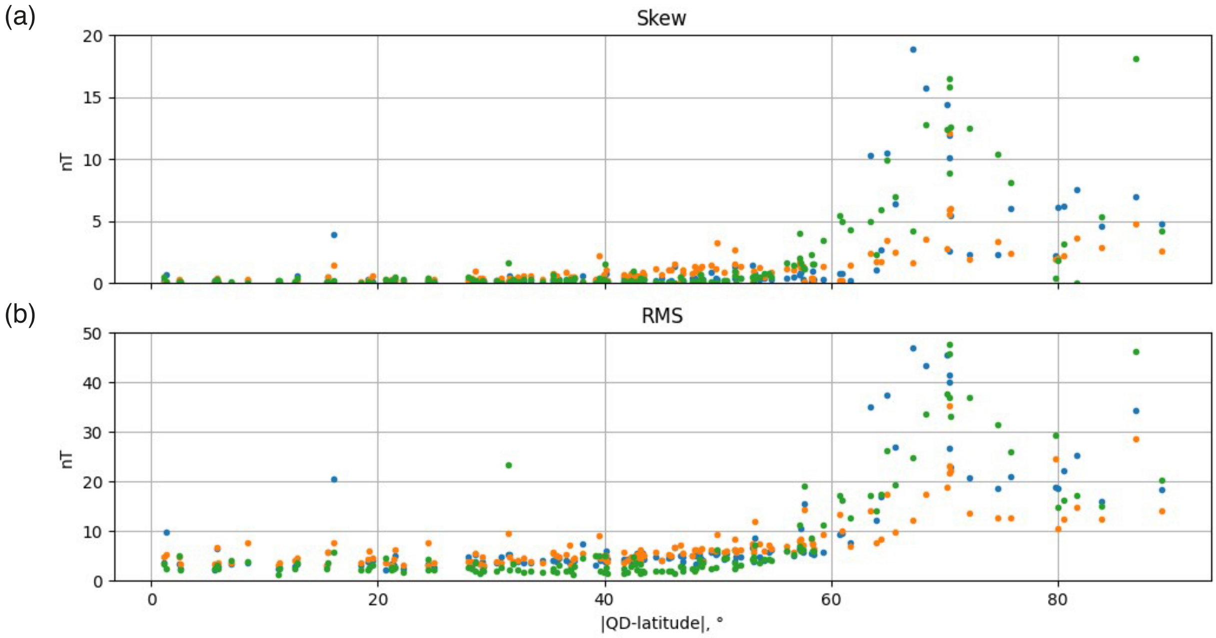


**Figure 2.** The dependence of the nonparametric skew (a) and the RMS (b) of the selected residuals for $X$ (blue), $Y$ (orange) and $Z$ (green) components on the quasi-dipole geomagnetic latitude of 143 observatories located in both hemispheres.

where $T$ is the data period for which the crustal field corrections are computed, $O_i^{ben}(T)$ is the absolute error for the period $T$ at the benchmark observatory $i$, $n_{ben}$ is the number of benchmark observatories, and $\sigma$ is standard deviation. Note that for observatories with data records longer than 11 years, MSD equals to the standard deviation.

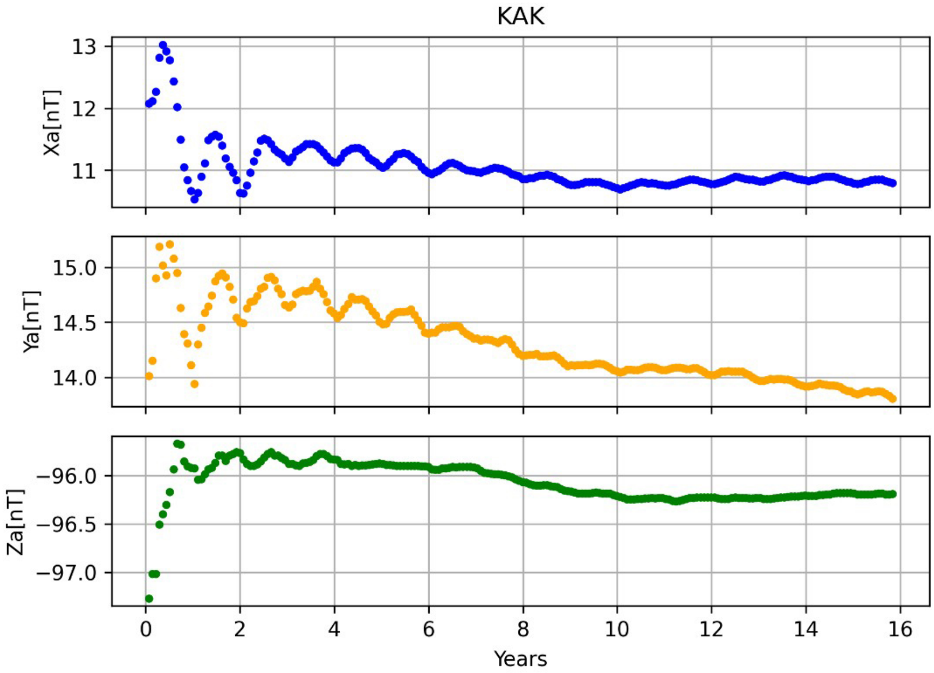


**Figure 3.** The anomalous crustal field values at Kakioka observatory calculated sequentially over periods starting from 27 days up to 11 years with an increment of 27 days.

Equation (3) is valid for the three orthogonal components ($X_a$, $Y_a$, $Z_a$) of the crustal magnetic field vector. To derive MSD for the declination anomaly $D_a$ we use the equation, which involves uncertainty using partial derivatives (Ku, 1966):

$$MSD(D_a) = \sqrt{MSD(X_a)^2 * \left(\frac{\partial D^*}{\partial x}\right)^2 + MSD(Y_a)^2 * \left(\frac{\partial D^*}{\partial y}\right)^2}, \quad (4)$$

where

$$D^* = \arctan\left(\frac{Y_a}{X_a}\right).$$

Figure 4 shows the MSD values as a function of quasi-dipole geomagnetic latitude and suggests that there is no clear latitudinal dependence. To maintain a consistent approach, further comparisons of the obtained corrections for the anomalous crustal field with other estimates in the following sections will be based on the MSD values.

Theoretically, geomagnetic coast effect can also affect the accuracy of $\mathbf{B}_a$ estimation. However, in practice it does not influence the result anyhow because of three main reasons. Firstly, the applied method smooths out any periodic variations. Secondly, the considered time ranges are much longer than the period of the coast effect fluctuations (Olsen and Kuvshinov, 2004). Thirdly, the magnitude of this effect is less than typical MSD values.

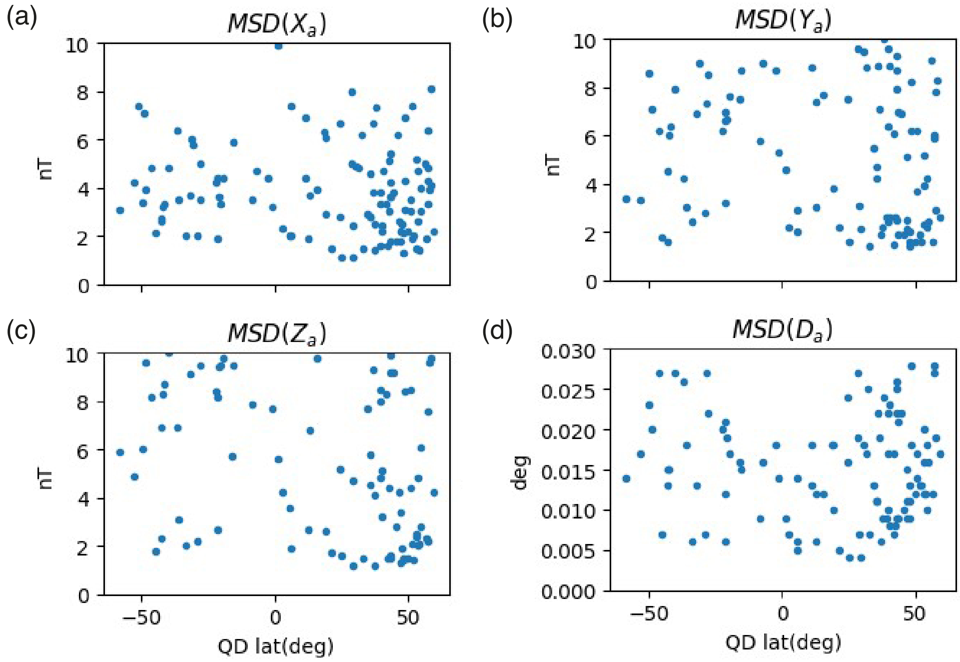


**Figure 4.** The dependence of the MSD for $X_a$ (a), $Y_a$ (b), $Z_a$ (c) and $D_a$ (d) on the quasi-dipole geomagnetic latitude of 118 observatories with |QD latitude|<60° considered in this study.

## 5. Results

In this paper, we analyze data from 118 magnetic observatories, 15 of which transmit data to the Interregional Analytical Geomagnetic Data Center (http://mag.gcras.ru). Of these, 10 are official members of the international INTERMAGNET network, and 5 are fully equipped according to INTERMAGNET standards (Bracke, 2025), but are not yet included in the network. Among 118 observatories, we select data from 27 benchmark observatories of the INTERMAGNET network to determine the reliability parameter MSD (see the previous section). As stated earlier, we limit the choice of observatories by 60° quasi-dipole geomagnetic latitude in both hemispheres to reduce data contamination due to high latitude geomagnetic activity. The locations of the observatories under consideration are shown on the map in Fig. 5; their complete list is given in Table A1 of the Appendix. The time intervals of available data from these observatories range from 0.5 to 23 years. To prevent the text from becoming too large, for further consideration we selected a representative sample of 25 observatories from different regions with available data intervals between 5 and 20 years (Table 1). The calculation results for all observatories are given in full tables of the Appendix; interpretations given in the text apply to all observatories.

Figures 6-8 show the consecutive procedure for calculating the residual field values, their selection, daily averaging, monthly averaging, and the median determination. As can be seen from the figures, the selection process allows us to discard a large amount of data that deviate significantly from the general trend due to sporadic magnetic field disturbances. For example, the significant increase in the scatter of hourly means of the residual field in 2011 at LER observatory (Fig. 6) is associated with the rapid increase in geomagnetic activity at the peak of the 24$^{th}$ solar cycle. It should be noted that among the three examples given (Figs. 6-8), LER observatory is the highest-latitude, which makes its data the most sensitive to the influence of space weather. An analysis of the outliers exceeding the deviation from the median by 200 nT in absolute value shows that all of them were observed during strong magnetic storms. The selection procedure by a set of geomagnetic activity indicators and subsequent monthly averaging minimize variations in the data associated with magnetospheric and ionospheric sources.

To study the short-term and long-term variability of the obtained values, we consider the variations of the monthly means of the residual field relative to the medians. Figures 9-11 display the corresponding plots for several observatories, where the variations are shown in dark blue, and the medians of these values are given in red. For reference, the Kp index values are also provided. A simple oscillatory pattern relative to the median values is observed in all time series of the monthly means of the residual field, which indicates that the crustal field has not changed

**Table 1.** Selection of 25 observatories under consideration, their geodetic coordinates and time intervals of the analyzed data. In all tables throughout the paper, the observatories are sorted by decreasing absolute quasi-dipole geomagnetic latitude (GM Lat) given for 2025.0 epoch. The observatories for which the corrections for the anomalous crustal field are published for the first time are marked with an asterisk. The complete list is given in Table A1 of Appendix.

| № | IAGA code | GM Lat (°) | Lat (°) | Lon (°) | Alt (km) | Start Date (yyyy-mm-dd) | End Date (yyyy-mm-dd) | Duration (years) |
|---|---|---|---|---|---|---|---|---|
| 1 | SIT | 59.3 | 57.06 | −135.33 | 0.02 | 2004-03-02 | 2019-12-30 | 15.83 |
| 2 | LER | 57.52 | 60.14 | −1.18 | 0.09 | 2004-04-01 | 2021-12-31 | 17.75 |
| 3 | SPG* | 57.28 | 60.54 | 29.72 | 0.05 | 2016-01-03 | 2024-12-31 | 8.92 |
| 4 | YAK* | 57.18 | 61.96 | 129.66 | 0.1 | 2011-01-01 | 2018-12-31 | 8 |
| 5 | UPS | 56.65 | 59.9 | 17.35 | 0.05 | 2004-03-03 | 2019-12-31 | 15.83 |
| 6 | BOX | 54.75 | 58.07 | 38.23 | 0.12 | 2004-04-29 | 2022-04-18 | 17.58 |
| 7 | EYR* | −49.94 | −43.47 | 172.39 | 0.1 | 2005-03-01 | 2020-12-31 | 15.58 |
| 8 | FRD | 46.9 | 38.2 | −77.37 | 0.07 | 2004-02-29 | 2019-12-30 | 15.92 |
| 9 | FRN | 42.55 | 37.09 | −119.72 | 0.33 | 2004-03-02 | 2019-12-30 | 15.83 |
| 10 | GNG | −42.31 | −31.36 | 115.72 | 0.05 | 2012-01-02 | 2019-12-30 | 7.75 |
| 11 | THY | 42.07 | 46.9 | 17.89 | 0.19 | 2004-03-03 | 2019-12-31 | 15.83 |
| 12 | AAA* | 39.52 | 43.25 | 76.92 | 1.3 | 2005-01-06 | 2014-12-31 | 10 |
| 13 | HBK* | −36.02 | −25.88 | 27.71 | 1.55 | 2004-03-03 | 2019-12-31 | 15.58 |
| 14 | IZN* | 35.51 | 40.5 | 29.72 | 0.26 | 2007-01-01 | 2019-12-31 | 12.83 |
| 15 | BMT* | 35.43 | 40.3 | 116.2 | 0.18 | 2010-01-01 | 2019-12-30 | 10 |
| 16 | SPT | 32.85 | 39.55 | −4.35 | 0.92 | 2004-03-01 | 2019-12-31 | 15.67 |
| 17 | KAK | 29.32 | 36.23 | 140.19 | 0.04 | 2004-03-03 | 2019-12-30 | 15.83 |
| 18 | SJG | 24.43 | 18.11 | −66.15 | 0.42 | 2004-02-29 | 2016-12-30 | 12.92 |
| 19 | IPM* | −19.55 | −27.17 | −109.42 | 0.08 | 2010-01-01 | 2015-09-14 | 5.67 |
| 20 | PHU* | 15.53 | 21.03 | 105.96 | 0.01 | 2005-01-06 | 2010-05-13 | 5.25 |
| 21 | BNG* | −7.06 | 4.33 | 18.57 | 0.4 | 1998-01-01 | 2003-10-12 | 5.83 |
| 22 | GUA | 5.91 | 13.59 | 144.87 | 0.14 | 2004-03-03 | 2020-12-31 | 16.75 |
| 23 | MBO | 2.49 | 14.39 | −16.96 | 0.01 | 1998-01-03 | 2018-08-03 | 20.33 |
| 24 | AAE* | 1.37 | 9.04 | 38.77 | 2.44 | 2004-03-03 | 2013-12-31 | 9.75 |
| 25 | HUA* | −1.15 | −12.04 | −75.32 | 3.34 | 2013-09-01 | 2021-12-30 | 8.33 |

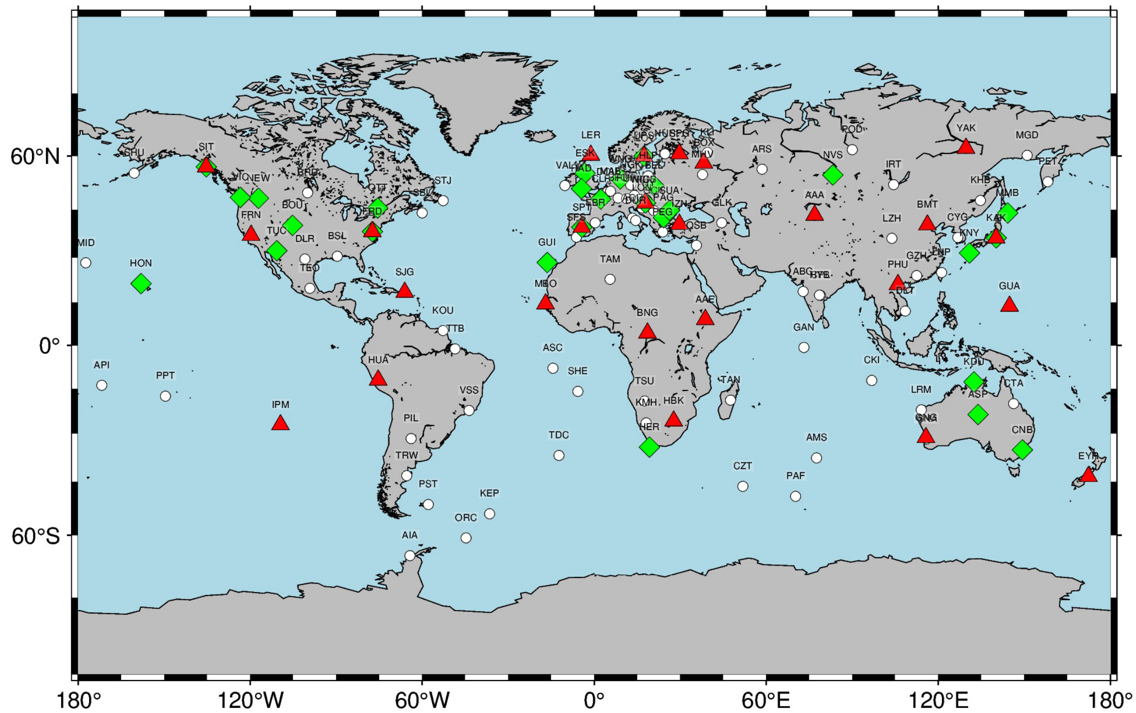


**Figure 5.** The locations of 118 observatories under consideration with their IAGA codes indicated. 27 benchmark INTERMAGNET observatories, whose data are used to derive the reliability parameter MSD, are marked with green; 25 observatories selected for analysis in the main part of the paper are marked with red.

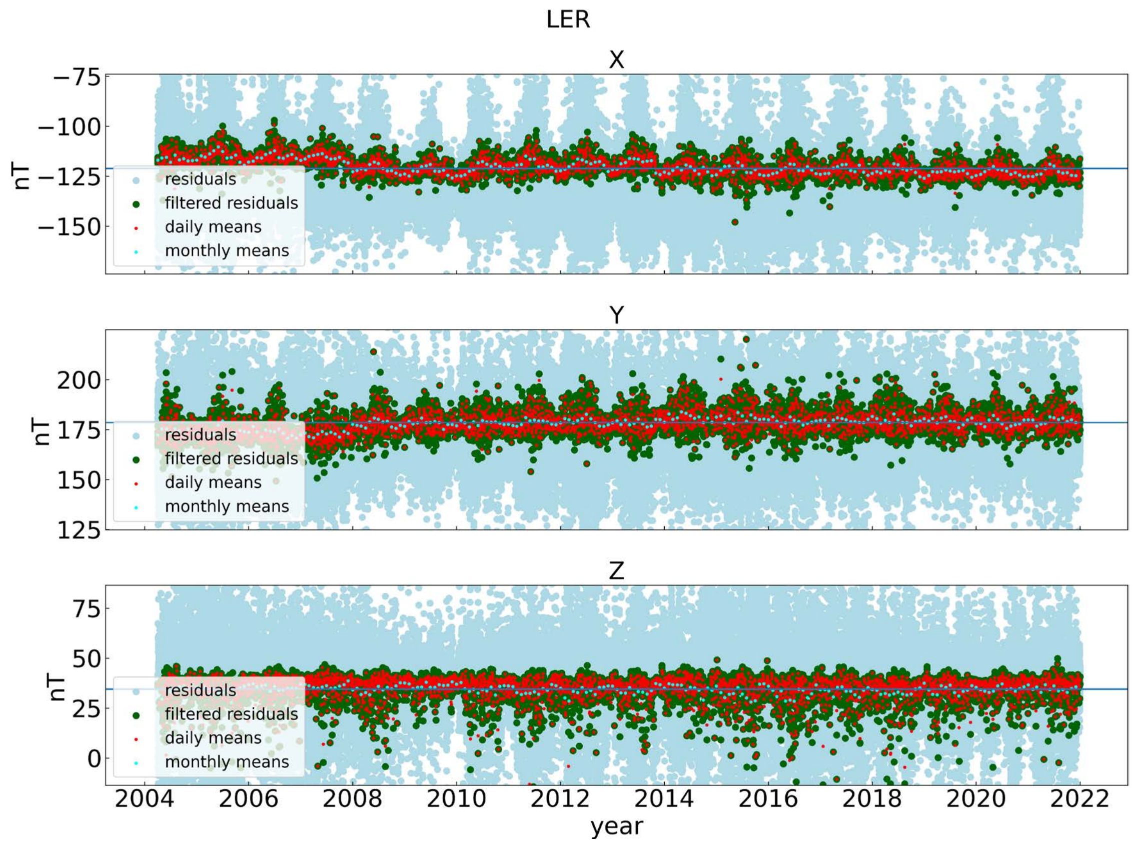


**Figure 6.** An example of sequential calculation of the anomalous crustal field values using the data from the Lerwic observatory (IAGA code LER): the residual field values are marked in blue, the selected residuals are marked in green, their daily means are marked in red, monthly means are marked in cyan, and the median is marked in black.

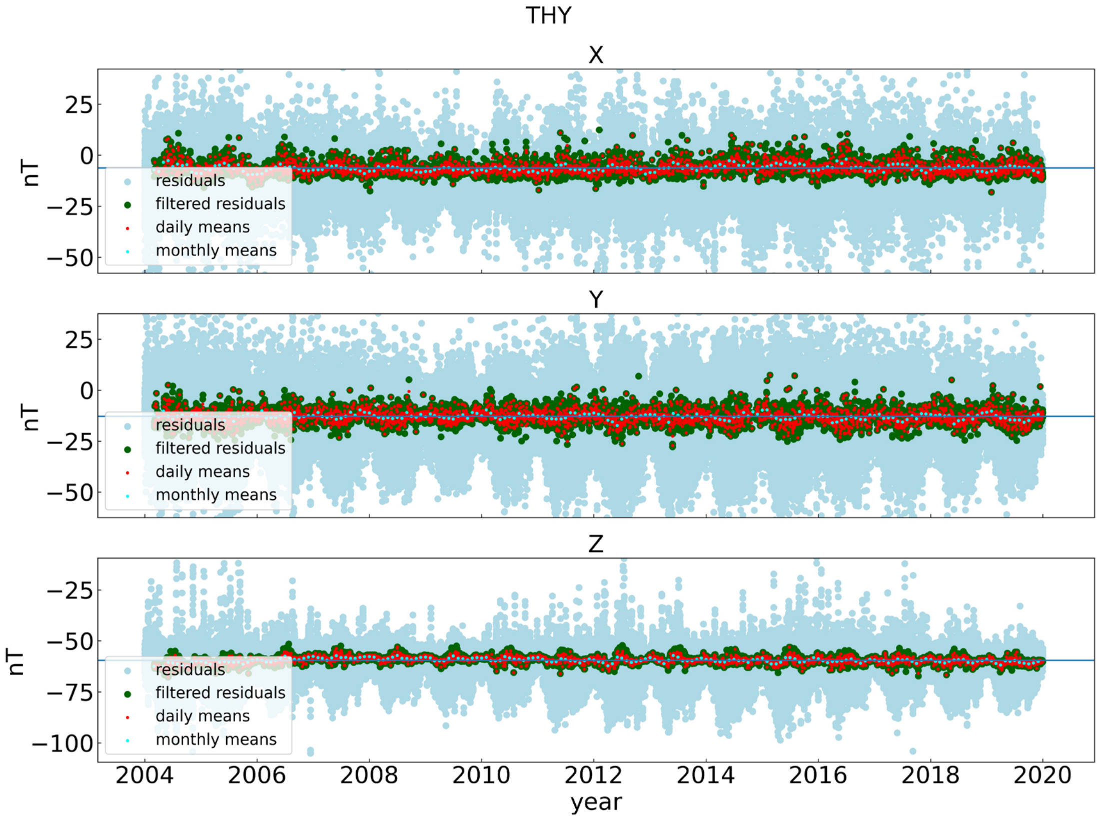


**Figure 7.** An example of sequential calculation of the anomalous crustal field values using data from the Tihany observatory (IAGA code THY), the designations are similar to Fig. 6.

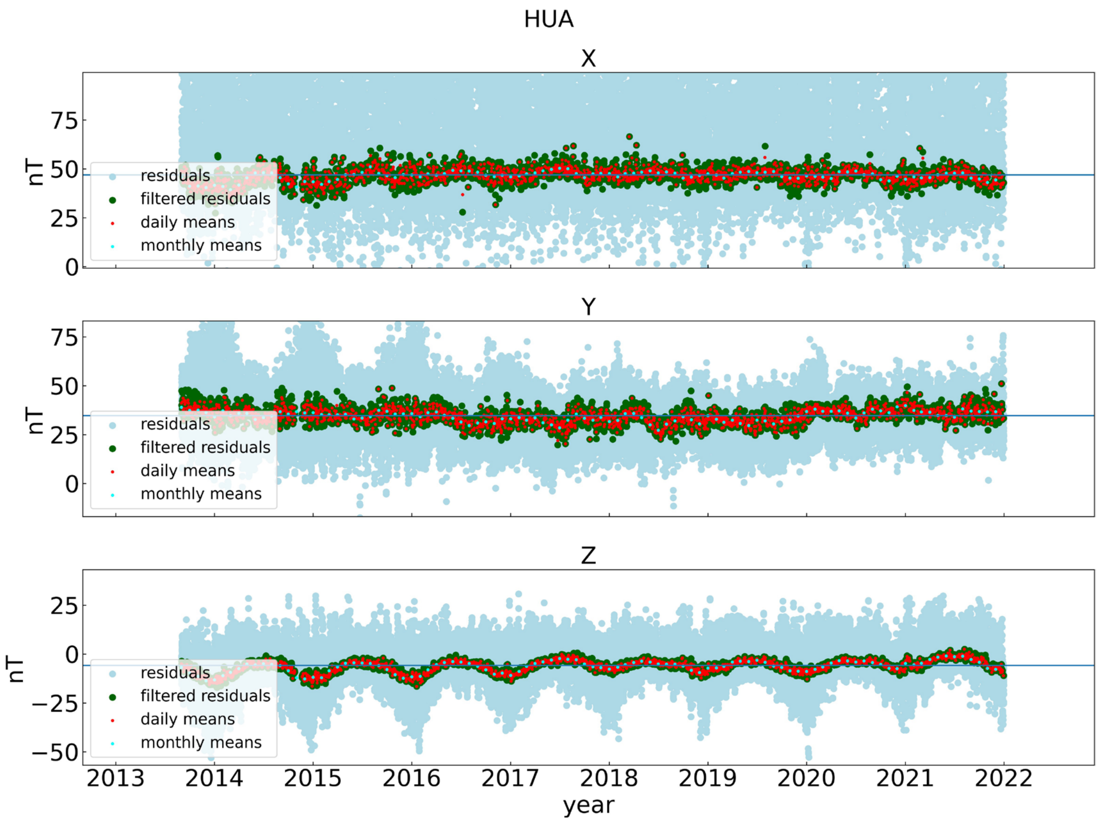


**Figure 8.** An example of sequential calculation of the anomalous crustal field values using the Huancayo observatory data (IAGA code HUA), the designations are similar to Fig. 6.

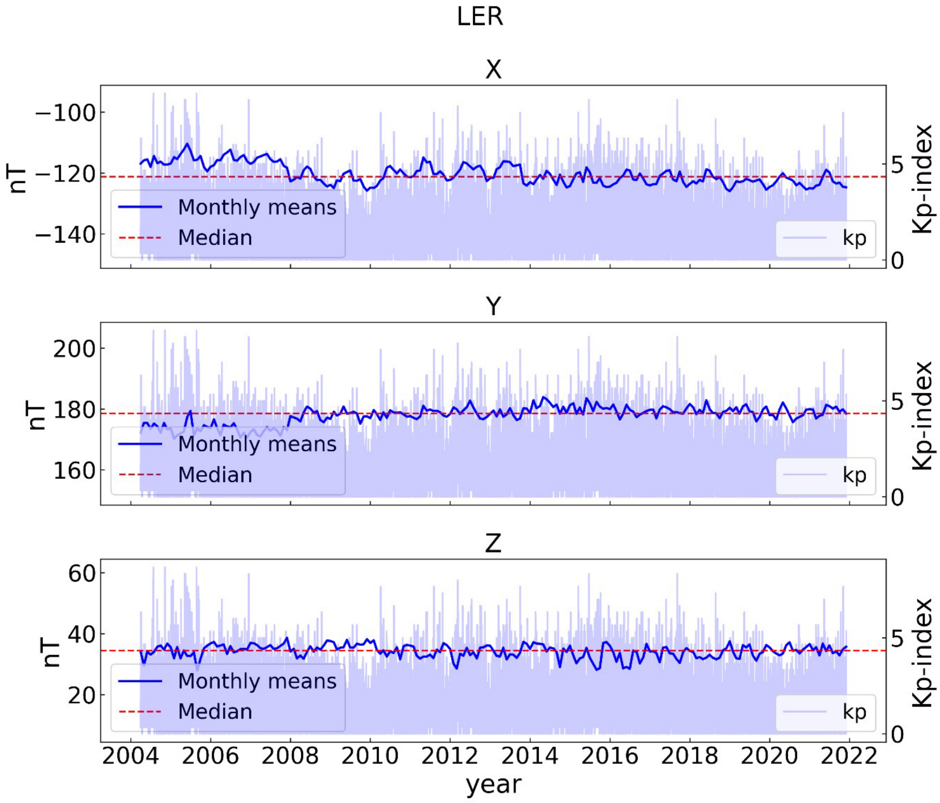


**Figure 9.** Deviations of the monthly means of the residual field at the Lerwic observatory (IAGA code LER) for 17,75 years (blue curve) from the median values for the entire period under consideration (red dashed line) and Kp index of geomagnetic activity (blue bars).

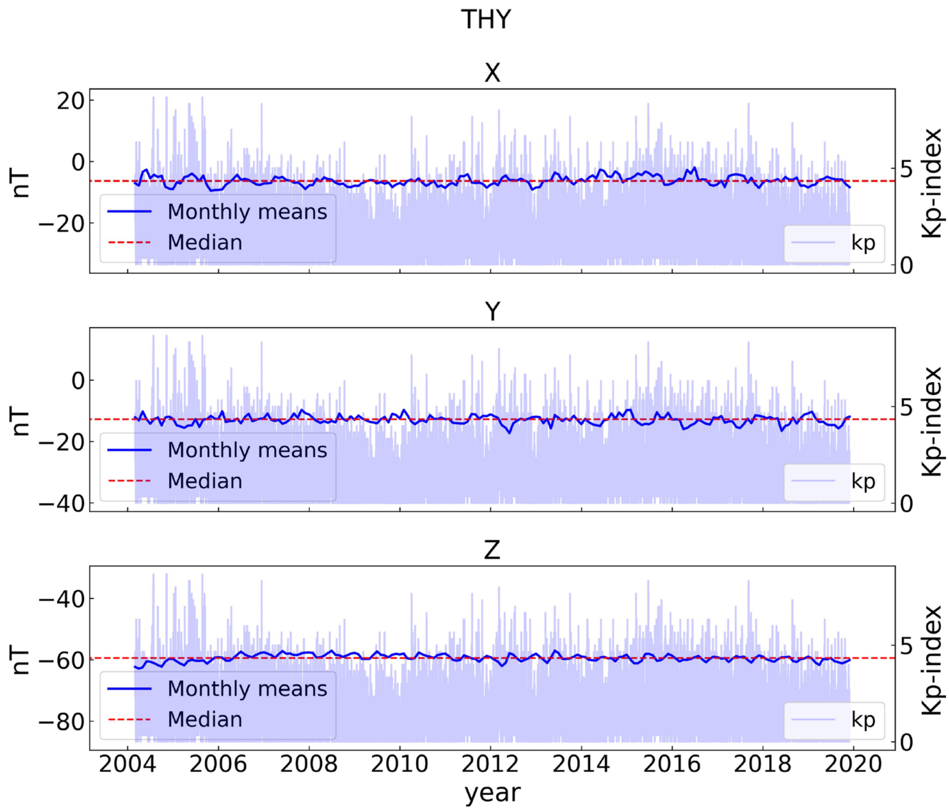


**Figure 10.** Deviations of the monthly means of the residual field at the Tihany observatory (IAGA code THY) for 15.83 years, designations are similar to Fig. 9.

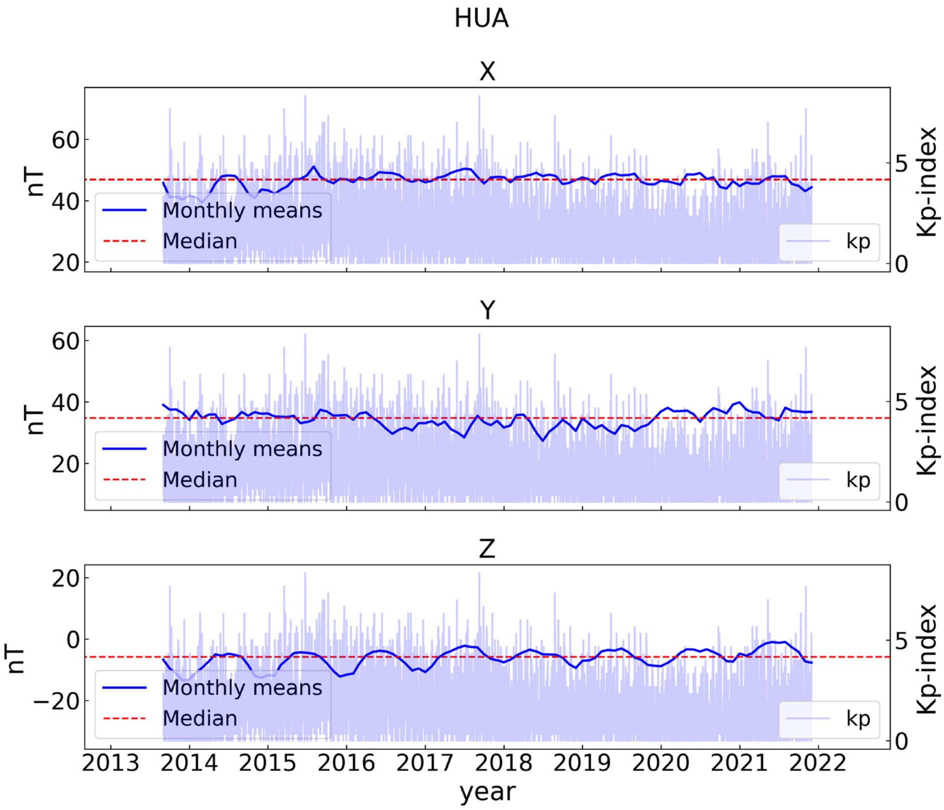


**Figure 11.** Deviations of the monthly means of the residual field at the Huancayo observatory (IAGA code HUA) for 8,33 years, designations are similar to Fig. 9.

over the period under consideration. This oscillation is associated with the seasonal variation of the geomagnetic field. Such variations in the components around the obtained medians for a given observatory can be balanced using $\varepsilon$. As it can be seen, seasonal variations are mostly evident in the horizontal $X$ and $Y$ components as they are sensitive to the natural variations of the magnetic field, whereas $Z$ component is subject to local man-made disturbances.

Although the above algorithm is aimed at minimizing the contribution of external fields, some graphs show a long-period variation associated with the 11-year cyclicity of solar activity. In particular, it can be observed in the $X$ component at LER observatory (Fig. 9, upper graph). The maximum amplitude of variations among all components and observatories considered reaches 57.4 nT.

For a graphical generalization of the obtained results, Fig. 12 shows the component-wise deviations of the monthly means of the residual field from the median for the selected observatories listed in Table 1, which are arranged in descending order of quasi-dipole geomagnetic latitude. The alternation of the graph colors again indicates remaining seasonal variations that could not be eliminated from the data during their selection. However, due to their periodic nature, their influence on the determined median value, which approximates the desired signal of the anomalous crustal field, is insignificant.

Table 2 represents the obtained estimations of the contribution of the anomalous crustal field $\mathbf{B}_a$ to the total values of the Cartesian components and the declination of the magnetic induction vector measured at magnetic observatories.

The results show that the sum of absolute values is the largest in the $Z$ component, while more than half of the values do not exceed 200 nT in absolute magnitude. This conclusion correlates well with the results of the previous similar studies, which considered observation series for June 2000-August 2009 (Verbanac et al., 2015) and for January 1998-July 2020 (Califf, 2022). This applies to all observatories given in Table A2 of Appendix.

Taking into account an extremely small number of operational observatories worldwide (less than 200), as well as the proposed uncertainty estimation parameter MSD, which considers the time series length, we believe that even rough estimates of the crustal field based on short data records are important for modeling and calibrating satellite observations. Therefore, in Table 3 we give the derived corrections for anomalous crustal field and their MSDs for those observatories where the available data interval is less than 5 years.

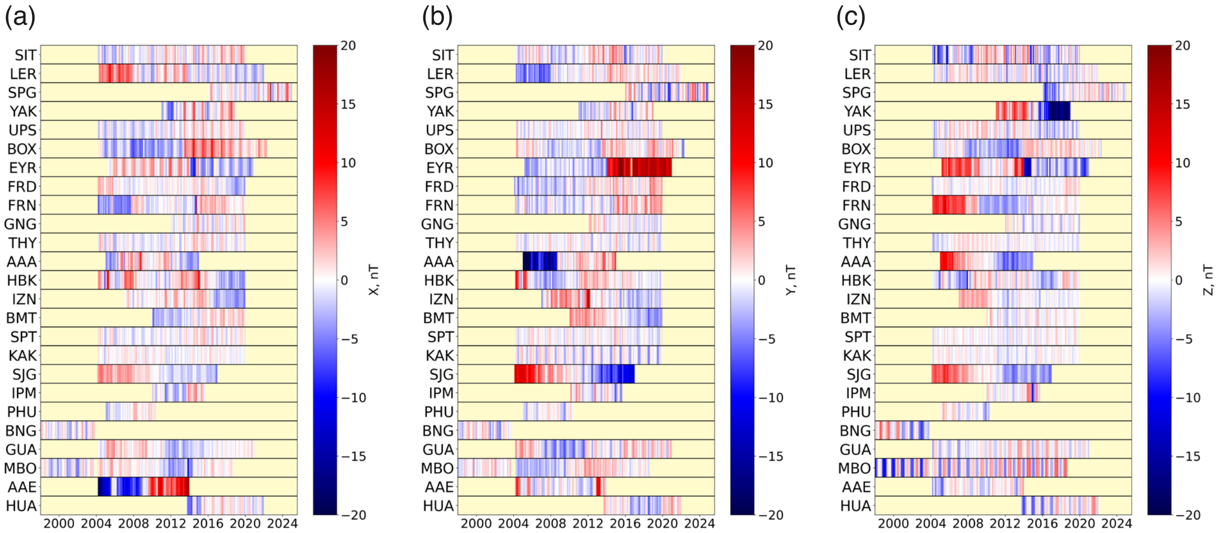


**Figure 12.** Variations of the monthly means of the residual field relative to the medians over 1998-2025 for the selected observatories listed in Table 1: $X$ component (a), $Y$ component (b) and $Z$ component (c); data gaps are marked in yellow. The observatories are sorted by decreasing quasi-dipole geomagnetic latitude. Complete graphs are given in Fig. A1 of Appendix.

Table 4 shows the relative errors of the modelled full values of the EMF components. The later are defined as the sum of the values of the main field components according to CHAOS-8.2 model and the crustal field components according to The1050 model. To define the full component values at observatories, $X$, $Y$ and $Z$ recordings were selected according to the five criteria (see Section 4 above) to eliminate the influence of external fields. For the time stamps of each remaining value, modelled full values were selected. The relative error $\gamma$ was derived for each component as

$$\gamma = median\left(\frac{Obs - (CHAOS + The1050)}{median(Obs)}\right) * 100\%,$$

where *Obs* are the selected observatory data, *CHAOS* are the main EMF values according to CHAOS-8.2 model, *The1050* are the anomalous crustal field values according to The1050 model.

As already noted, the estimation of the error in the total value of magnetic declination $D$ is also of great practical importance. In turn, the error in determining the magnetic declination (in degrees) is calculated using the equation (Ku, 1966):

$$\Delta_D = \sqrt{\left(\frac{\partial D}{\partial X}\right)^2 {\Delta_X}^2 + \left(\frac{\partial D}{\partial Y}\right)^2 {\Delta_Y}^2}.$$

By definition of $H^2 = X^2 + Y^2$ and $D = \arctan\left(\frac{Y}{X}\right)$, knowing that

$$(\arctan f)' = \frac{1}{1 + f^2},$$

it follows

$$\Delta_D = \frac{1}{H^2}\sqrt{Y^2{\Delta_X}^2 + X^2{\Delta_Y}^2},$$

where $\Delta_X$, $\Delta_Y$ are the medians of the differences between the observed and modelled full values for the corresponding components, $X$, $Y$ are full model values of the components.

**Table 2.** Calculated corrections for anomalous crustal field by components $X_a$, $Y_a$, $Z_a$ (nT) and declination $D_a$ (°) ($D_a$ is valid for 2025.0 epoch), as well as the obtained values of the MSD at the selected observatories listed in Table 1. Complete list is given in Table A2 of Appendix.

| IAGA code | $X_a$ (nT) | $Y_a$ (nT) | $Z_a$ (nT) | $D_a$ (°) | MSD($X_a$) (nT) | MSD($Y_a$) (nT) | MSD($Z_a$) (nT) | MSD($D_a$) (°) |
|---|---|---|---|---|---|---|---|---|
| SIT | 19.7 | −14.7 | −91.3 | 0.1 | 2.2 | 2.6 | 4.2 | 0.009 |
| LER | −121.2 | 178.5 | 34.5 | 0.7 | 3.3 | 2.9 | 2.2 | 0.009 |
| SPG* | 200.9 | −75 | −188.9 | 0.4 | 4.8 | 5.9 | 7.6 | 0.066 |
| YAK* | 53.9 | −1191.2 | 102.8 | 4.5 | 4.3 | 6 | 13 | 0.031 |
| UPS | 151.8 | −13.2 | −125.5 | 0.1 | 1.9 | 1.6 | 2.3 | 0.03 |
| BOX | 4.4 | 2 | −353.8 | 0 | 4 | 2.4 | 2.8 | 0.011 |
| EYR* | 24.4 | −25.4 | 81.1 | 0.1 | 3.4 | 8.6 | 6 | 0.023 |
| FRD | 78.2 | −43.5 | 121.4 | 0.1 | 1.8 | 2.5 | 1.3 | 0.043 |
| FRN | 9.3 | −16.6 | −246.6 | 0 | 3 | 2.6 | 4.4 | 0.024 |
| GNG | 5 | −38.5 | 173.5 | 0.1 | 3.2 | 6 | 8.3 | 0.006 |
| THY | −6.3 | −12.8 | −59.5 | 0 | 1.6 | 1.5 | 1.5 | 0.034 |
| AAA* | 154.1 | 36 | −233.3 | 0.1 | 3.8 | 9.6 | 8 | 0.01 |
| HBK* | 106.2 | −19.2 | 41.1 | 0.1 | 3.5 | 3 | 3.1 | 0.014 |
| IZN* | 146.3 | −20.1 | 3.6 | 0.1 | 2.8 | 4.2 | 4.5 | 0.007 |
| BMT* | 323.1 | −615.2 | 151.5 | 1.2 | 2.8 | 4.7 | 5.8 | 0.007 |
| SPT | 11.7 | 9.6 | −26.6 | 0 | 1.5 | 1.4 | 1.5 | 0.014 |
| KAK | 10.9 | 14.2 | −96.1 | 0 | 1.1 | 2.1 | 1.2 | 0.008 |
| SJG | −53.1 | 128.2 | 131.3 | 0.2 | 2.8 | 7.5 | 5.2 | 0.013 |
| IPM* | 12 | 254.2 | −586.7 | 0.5 | 4.4 | 7.6 | 9.8 | 0.015 |
| PHU* | 13.9 | 11.1 | −17.7 | 0 | 3.9 | 7.7 | 9.8 | 0.005 |
| BNG* | −80.3 | 12 | 342.8 | 0 | 4.7 | 9 | 11.1 | 0.008 |
| GUA | 123.7 | 78.4 | 49.3 | 0.1 | 2 | 2.9 | 1.9 | 0.038 |
| MBO | 111.1 | 38 | 63.8 | 0.1 | 2.3 | 2.2 | 4.2 | 0.034 |
| AAE* | 724.3 | −107.6 | 534.6 | 0.2 | 9.9 | 4.6 | 5.6 | 0.012 |
| HUA* | 46.9 | 34.7 | −5.8 | 0.1 | 3.2 | 5.3 | 7.7 | 0.017 |

**Table 3.** Calculated corrections for anomalous crustal field at the observatories with an available data interval less than 5 years. Designations are the same as in the Table 2.

| IAGA code | $X_a$ (nT) | $Y_a$ (nT) | $Z_a$ (nT) | $D_a$ (°) | MSD($X_a$) (nT) | MSD($Y_a$) (nT) | MSD($Z_a$) (nT) | MSD($D_a$) (°) |
|---|---|---|---|---|---|---|---|---|
| POD* | 38.4 | −3.8 | −295.7 | 0 | 8.1 | 12.7 | 11.8 | 0.066 |
| NUR* | 303.2 | −109.2 | 102 | 0.6 | 6.4 | 11.3 | 11.6 | 0.043 |
| MHV* | −399.5 | 499.8 | −312.8 | 1.9 | 7.4 | 11.3 | 12 | 0.038 |
| AIA* | 94.9 | −95 | 430.1 | 0.3 | 7.4 | 12.5 | 11.7 | 0.035 |
| ORC* | −17.6 | 12.5 | −3.5 | 0 | 7.1 | 12 | 11.7 | 0.039 |
| VAL | 130.7 | −42.8 | −25.4 | 0.1 | 6.9 | 12.1 | 11.8 | 0.035 |
| MAB* | 24.4 | −13.8 | 165.9 | 0 | 6.2 | 11.1 | 11.5 | 0.032 |
| LON* | −18.3 | −3.9 | −36.1 | 0 | 4.7 | 8.9 | 10.5 | 0.023 |
| DLR* | 120.5 | 80.8 | 52.9 | 0.2 | 7.3 | 10 | 11.4 | 0.023 |
| GLK* | −143.5 | −40.2 | −251.8 | 0.1 | 6.7 | 12.3 | 11.9 | 0.028 |
| DUR* | 49.8 | 56.2 | 25.7 | 0.1 | 4.6 | 8.9 | 10.5 | 0.02 |
| PEG* | −27.1 | 40.3 | −21.9 | 0.1 | 6.2 | 11.2 | 11.6 | 0.024 |
| TRW* | −6.2 | −28.7 | 113 | 0.1 | 6 | 10.4 | 11.3 | 0.033 |
| TSU* | 48.5 | −57.5 | 80.3 | 0.2 | 5.8 | 9 | 10.8 | 0.036 |
| CYG | −51.7 | 51.8 | −99.8 | 0.1 | 4.9 | 9.5 | 10.8 | 0.018 |
| QSB* | 96.4 | −120.1 | −51.2 | 0.3 | 5 | 9.6 | 10.9 | 0.019 |
| TEO* | 7.5 | 42.4 | −112.7 | 0.1 | 8 | 12.9 | 12 | 0.027 |
| MID* | 859.9 | 223.2 | 1034.4 | 0.2 | 6.7 | 12 | 11.7 | 0.024 |
| LNP* | 44.5 | 47.8 | 37.8 | 0.1 | 6.1 | 11.2 | 11.5 | 0.018 |
| GZH* | 422.3 | 159.4 | −1504.6 | 0.3 | 6.3 | 11.4 | 11.7 | 0.017 |
| HYB | 258.2 | 25.8 | 473.5 | 0 | 4.4 | 8.8 | 10.6 | 0.013 |
| CPL* | 64.3 | −48.7 | −158.5 | 0.1 | 6.9 | 12.2 | 11.7 | 0.018 |
| TTB* | 11.5 | −52.3 | 106.7 | 0.1 | 4.4 | 8.7 | 10.4 | 0.018 |

The analysis of $\gamma$ shows that for most observatories the error in the $X$ and $Z$ components does not exceed 1%. As is known, the $Y$ component, as the smallest of all in modulus, is the most sensitive to absolute errors, which is confirmed by the observed errors (Table 4). The errors $\Delta_D$ for some observatories stand out significantly, which is due to the complex structure of the anomalous crustal field in the regions of their location. As an example, let us consider YAK observatory more in detail, for which $\Delta_D = 3.19°$. Such huge error in declination anomaly modeling can be explained by the uncertainty of source data used to build such models. According to available digital maps of magnetic anomalies, there is a positive anomaly $\Delta T$ extended in the North-South direction in the area of YAK observatory (Fig. 13). At the same time, the estimated magnitude of the anomaly differs significantly: WDMAM and VSEGEI maps estimate its value at about 1000 nT, whereas according to EMAG map its maximum is close to 5000 nT. We don't know exactly which anomaly grid is correct. Considering that all models under study are based on WDMAM grid, probably WDMAM and VSEGEI grids are not accurate enough.

**Table 4.** Errors of the full model values of the EMF components (CHAOS + The1050) relative to observatory data for the selected observatories listed in Table 1. Complete list is given in Table A3 of Appendix.

| IAGA code | $\gamma(X)$ (%) | $X$ | $\gamma(Y)$ (%) | $Y$ | $\gamma(Z)$ (%) | $\Delta_D$ (°) |
|---|---|---|---|---|---|---|
| SIT | 0.4 | 14826.8 | 12.9 | 5535.6 | −1.7 | 2.41 |
| LER | 0.2 | 15013.6 | 7.1 | −613.6 | 0.2 | 0.24 |
| SPG* | −0.3 | 14450.8 | 0.1 | 2786.2 | 0.5 | 0.05 |
| YAK* | −0.3 | 13467.6 | −17.1 | −4955.8 | 0.4 | 3.19 |
| UPS | 0.2 | 15153 | −0.6 | 1286.5 | 0 | 0.13 |
| BOX | 0 | 15295.2 | −1.8 | 3168 | 0.1 | 0.27 |
| EYR* | −0.2 | 19322.9 | 0.4 | 8349.1 | 0.1 | 0.04 |
| FRD | 0 | 20936.7 | −0.6 | −3881.5 | −0.1 | 0.05 |
| FRN | 0 | 22891.3 | −0.2 | 5481.5 | 0.1 | 0.01 |
| GNG | 0.1 | 24004.1 | −1.5 | −693.1 | 0 | 0.02 |
| THY | 0.1 | 21492.9 | −1.3 | 1388.2 | 0 | 0.11 |
| AAA* | 0 | 24856.8 | −0.3 | 2115.8 | 0.5 | 0.03 |
| HBK* | −0.3 | 12343 | −1 | −3929.1 | −0.2 | 0.24 |
| IZN* | −0.4 | 25073.1 | 1.7 | 2136.2 | 0 | 0.05 |
| BMT* | −1 | 28031 | −14.7 | −3871.1 | −0.4 | 1.18 |
| SPT | 0 | 25916.5 | −0.4 | −750.1 | 0.1 | 0.04 |
| KAK | −0.1 | 29745.7 | 0.4 | −3765.8 | 0.1 | 0.04 |
| SJG | 0.6 | 26324.8 | −0.4 | −5849.9 | −0.5 | 0.11 |

| IAGA code | $\gamma(X)$ (%) | $X$ | $\gamma(Y)$ (%) | $Y$ | $\gamma(Z)$ (%) | $\Delta_D$ (°) |
|---|---|---|---|---|---|---|
| IPM* | −1.2 | 25144.2 | −3 | 7122.7 | −2.4 | 0.48 |
| PHU* | 0 | 38958.3 | 0.7 | −806.9 | 0.1 | 0.02 |
| BNG* | −0.4 | 31960.5 | 18.2 | −517.5 | −0.2 | 0.16 |
| GUA | −0.3 | 35720.2 | −10.2 | 765 | −0.4 | 0.08 |
| MBO | −0.1 | 32015.9 | 1.5 | −4652.3 | −0.9 | 0.15 |
| AAE* | −2 | 36187.5 | 11.9 | 1047.4 | −32.6 | 0.22 |
| HUA* | −0.2 | 24745.8 | −0.2 | −1380.4 | −1.4 | 0.03 |

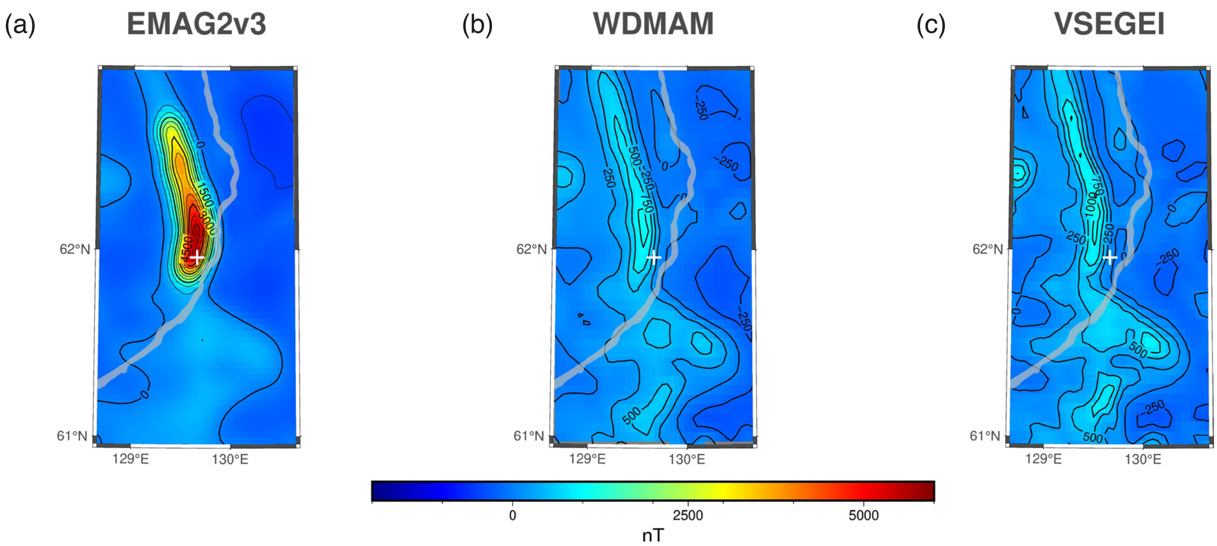


**Figure 13.** Anomalies $\Delta T$ of the crustal magnetic field according to the digital maps EMAG (a), WDMAM (b) and VSEGEI (c) in the vicinity of YAK observatory (marked with a white cross). The gray curve represents Lena river.

# 6. Comparison with previously obtained results

## 6.1 Comparison with calculated corrections for anomalous crustal field based on observatory data

Comparisons with the results by Verbanac et al. (2015) show that from the 84 values obtained in both works (3 components from 28 observatories), 24 values fall within the $2\sigma'$ range relative to the average values we obtained. The full comparison results are represented in Table 5, which includes all observatories used by both Verbanac et al. (2015) and us. The dashes in the table indicate values with a deviation greater than $3\sigma'$.

**Table 5.** Comparison of the obtained values with the results by Verbanac et al. (2015): $X_{Ver}$, $Y_{Ver}$, $Z_{Ver}$ are correction values from the cited work; $|\Delta_X|$, $|\Delta_Y|$, $|\Delta_Z|$ are absolute differences between these values and the corrections we obtained; err_X, err_Y, err_Z are MSDs within which the absolute differences lie.

| IAGA code | $X_{Ver}$ (nT) | $Y_{Ver}$ (nT) | $Z_{Ver}$ (nT) | $\|\Delta_X\|$ (nT) | $\|\Delta_Y\|$ (nT) | $\|\Delta_Z\|$ (nT) | err_X | err_Y | err_Z |
|---|---|---|---|---|---|---|---|---|---|
| PAF | 439.9 | −141.9 | −322.3 | 26.3 | 1.3 | 47.6 | — | $1\sigma'$ | — |
| LER | −136.2 | 176.2 | 57.3 | 15 | 2.3 | 22.8 | — | $1\sigma'$ | — |
| OTT | 122.5 | −133.9 | 149.5 | 20.8 | 7.7 | 23 | — | — | — |
| VIC | 16.2 | 6.7 | −269.2 | 17.4 | 4.7 | 13.8 | — | $3\sigma'$ | — |
| CZT | −761.8 | 1092.1 | 147.7 | 22.1 | 3.5 | 3 | — | $2\sigma'$ | $1\sigma'$ |
| ESK | 1.1 | −32.5 | −35.8 | 19.1 | 0.7 | 25.6 | — | $1\sigma'$ | — |
| NVS | 44.7 | −54.3 | 34.6 | 30.4 | 2.1 | 17.8 | — | $2\sigma'$ | — |
| HLP | 37.6 | −163.7 | −86 | 26.3 | 1.8 | 17.6 | — | $1\sigma'$ | — |
| STJ | 32.1 | 44.2 | 32.2 | 20.7 | 2.5 | 17.4 | — | $1\sigma'$ | $3\sigma'$ |
| WNG | 43.8 | 46.6 | −53.2 | 13.1 | 4.6 | 10.6 | — | $3\sigma'$ | — |
| VAL | 106.9 | −42.4 | −1 | 23.8 | 0.4 | 24.4 | — | $1\sigma'$ | $3\sigma'$ |
| BOU | −27.1 | 32.2 | −125.4 | 32.2 | 5.6 | 16.5 | — | $3\sigma'$ | — |
| NGK | −31.6 | 1 | −62.3 | 23 | 0.8 | 19.5 | — | $1\sigma'$ | — |
| BEL | 105.2 | 140.2 | 324.9 | 26.6 | 3.8 | 15.8 | — | $3\sigma'$ | — |
| HAD | −51.7 | 18.3 | 91.3 | 18.8 | 3.2 | 21.1 | — | $2\sigma'$ | — |
| FRD | 56.9 | −51.4 | 137.9 | 21.3 | 7.9 | 16.5 | — | — | — |
| DOU | 5.4 | −15.5 | 99.6 | 21.3 | 2.5 | 24.2 | — | $2\sigma'$ | — |
| HRB | 11.1 | −18.3 | −67 | 25.2 | 2.2 | 19.9 | — | $1\sigma'$ | $2\sigma'$ |
| CLF | −82.1 | −13 | 124.8 | 22.8 | 2.3 | 25.2 | — | $1\sigma'$ | — |
| GNA | −35.5 | −100.8 | 96.5 | 23 | 5.9 | 22.9 | — | $2\sigma'$ | — |
| THY | −28.9 | −10.1 | −40.5 | 22.6 | 2.7 | 19 | — | $2\sigma'$ | — |
| EBR | −16.8 | 3.8 | 15.7 | 18.5 | 2.5 | 19.9 | — | $1\sigma'$ | $3\sigma'$ |
| KAK | −14.8 | 10.1 | −86.2 | 25.7 | 4.1 | 9.9 | — | $2\sigma'$ | — |

| IAGA code | $X_{Ver}$ (nT) | $Y_{Ver}$ (nT) | $Z_{Ver}$ (nT) | $\|\Delta_X\|$ (nT) | $\|\Delta_Y\|$ (nT) | $\|\Delta_Z\|$ (nT) | err_X | err_Y | err_Z |
|---|---|---|---|---|---|---|---|---|---|
| HON | −185.2 | 80.8 | −320.6 | 21.2 | 7.5 | 5.8 | — | — | — |
| PPT | −922 | −1039.7 | −398.6 | 31.4 | 6.1 | 9.6 | $2\sigma'$ | $1\sigma'$ | $2\sigma'$ |
| ABG | −99.4 | 434.1 | 713.9 | 8.6 | 17.7 | 36 | $3\sigma'$ | $3\sigma'$ | — |
| GUA | 108.6 | 74.5 | 45 | 15.1 | 3.9 | 4.3 | — | $2\sigma'$ | $3\sigma'$ |
| MBO | 100.7 | 38.7 | 75.9 | 10.4 | 0.7 | 12.1 | — | $1\sigma'$ | $3\sigma'$ |

When comparing the values we obtained with those found by Califf et al. (2022), the percentage of deviations within the $2\sigma'$ range is higher (118 out of 147) than in the previous case. At the same time, the algorithm we used to calculate the corrections for the anomalous crustal field was borrowed from this cited article. The discrepancies can be explained by the fact that the contribution of the anomalous crustal field was determined using data from different observation periods – the time overlap was slightly more than 85% of the period we studied. Also, the detailed analysis of Califf et al. (2022) results revealed that they used incorrect coordinates for some observatories, which led to significant errors in the crustal field determination at observatory sites. For example, for San Fernando observatory (IAGA code SFS) they used 36.462°N, 6.205°W instead of 36.667°N, 5.945°W where the observatory is actually located. Here, we present the comparison results for those observatories from Table 1, which were analyzed by Califf et al. (2022) (see Table 6). The compete information for all observatories studied by both Califf et al. (2022) and us is given in Table A4 of Appendix. As before, the dashes indicate values with a deviation greater than $3\sigma'$. Since Califf et al. (2022) present the values of the EMF vector components in geocentric spherical coordinates, for correct comparison our data were preliminarily transformed from the NED coordinate system (N – north, E – east, D – down) to the geocentric one.

**Table 6.** Comparison of the obtained values with the results by Califf et al. (2022) for selected 12 observatories (the values of the EMF components are given in geocentric spherical coordinates): $Br_{Cal}$, $B\theta_{Cal}$, $B\varphi_{Cal}$ are the values from the cited work; $|\Delta_{Br}|$, $|\Delta_{B\theta}|$, $|\Delta_{B\varphi}|$ are absolute differences between these values and the corrections we obtained; err_Br, err_B$\theta$, err_B$\varphi$ are MSDs within which the absolute differences lie. Complete list is given in Table A4 of Appendix.

| IAGA code | $Br_{Cal}$ (nT) | $B\theta_{Cal}$ (nT) | $B\varphi_{Cal}$ (nT) | $\|\Delta_{Br}\|$ (nT) | $\|\Delta_{B\theta}\|$ (nT) | $\|\Delta_{B\varphi}\|$ (nT) | err_Br | err_B$\theta$ | err_B$\varphi$ |
|---|---|---|---|---|---|---|---|---|---|
| SIT | 85.6 | −27.2 | −16 | 5.6 | 7.2 | 1.3 | $2\sigma'$ | — | $1\sigma'$ |
| LER | −40.1 | 126.2 | 175.9 | 6 | 4.9 | 2.6 | $3\sigma'$ | $2\sigma'$ | $1\sigma'$ |
| UPS | 119.9 | −151.9 | −14.5 | 5.1 | 0.3 | 1.3 | $3\sigma'$ | $1\sigma'$ | $1\sigma'$ |
| BOX | 349.8 | −2.6 | 1.8 | 3.9 | 2.9 | 0.2 | $2\sigma'$ | $1\sigma'$ | $1\sigma'$ |
| FRD | −110.6 | −83.2 | −44.4 | 11 | 5.4 | 0.9 | — | — | $1\sigma'$ |
| FRN | 235.7 | −5.4 | −16.9 | 10.9 | 4.7 | 0.3 | $3\sigma'$ | $2\sigma'$ | $1\sigma'$ |
| GNG | −164.8 | −0.9 | −38.5 | 8.7 | 4.6 | 0 | $2\sigma'$ | $2\sigma'$ | $1\sigma'$ |

| IAGA code | $Br_{Cal}$ (nT) | $B\theta_{Cal}$ (nT) | $B\varphi_{Cal}$ (nT) | $\lvert\Delta_{Br}\rvert$ (nT) | $\lvert\Delta_{B\theta}\rvert$ (nT) | $\lvert\Delta_{B\varphi}\rvert$ (nT) | err_Br | err_B$\theta$ | err_B$\varphi$ |
|---|---|---|---|---|---|---|---|---|---|
| THY | 57.3 | 5.5 | −12.9 | 2.2 | 0.6 | 0.1 | $2\sigma'$ | $1\sigma'$ | $1\sigma'$ |
| SPT | 26.9 | −13.7 | 9.1 | 0.4 | 1.9 | 0.5 | $1\sigma'$ | $2\sigma'$ | $1\sigma'$ |
| KAK | 98 | −14.3 | 14.4 | 2 | 3.1 | 0.2 | $2\sigma'$ | $3\sigma'$ | $1\sigma'$ |
| SJG | −127.2 | 51.6 | 131.3 | 4 | 1.8 | 3.1 | $1\sigma'$ | $1\sigma'$ | $1\sigma'$ |
| GUA | −54.2 | −126.1 | 78.9 | 4.7 | 2.5 | 0.5 | $3\sigma'$ | $2\sigma'$ | $1\sigma'$ |

## 6.2 Comparison with models of magnetic anomalies

As noted earlier, analytical spherical harmonic models of the anomalous crustal field provide the possibility of component-by-component evaluation of its contribution to the total internal field. We compare the corrections we obtained for the anomalous crustal field (Table A2) with the values of individual components of the anomalous crustal field according to: (1) The1050 model, (2) WDMAM model, and (3) xDLFI model. For the discrepancy estimations, absolute ($\Delta$) and relative ($\delta$) errors for each component are calculated. Here, it is necessary to take into account the fact that errors in the original measurements penetrate into the models constructed on their basis. In this regard, the values of relative errors for each component are calculated using the equation of the inverse problem of the error theory (Bakhvalov et al., 1987). First, the contributions of errors of individual components $X$, $Y$ and $Z$ to the modulus of the vector of the full EMF are estimated, which are considered equivalent in accordance with the principle of equal influences:

$$V_i^{err} = \frac{T^{err}}{n * \left|\frac{\partial F}{\partial V_i}\right|}, \tag{5}$$

where $i = 1, 2, 3$, $V_i$ are the components $X$, $Y$, $Z$ respectively, $n$ is the number of components, $F = \sqrt{X^2 + Y^2 + Z^2}$ is the modulus of the vector of the main EMF with the components $X$, $Y$, $Z$ taken for 2025.0 epoch according to the CHAOS model at the coordinates of each observatory, and $T^{err}$ is the established original measurement error for a given region; these errors were published by Meyer et al. (2017) for each initial data set used for modeling the anomalous crustal field.

Next, the values of relative errors for each component are calculated as

$$\delta_i = \frac{|\Delta V_i|}{V_i^{err}} * 100\%,$$

where $\Delta V_i$ is the difference between the value from Table A2 for the given component and the modelled one. Values $\delta$ less than 100% indicate that the error in determining the component value according to a particular model does not exceed the measurement error in the region.

The results are represented in Tables 7-10.

**Table 7.** Comparison of the model values of the crustal field components according to The1050 with the values we obtained for the selected observatories from Table 1. Complete list is given in Table A5 of Appendix.

| IAGA code | X_The1050 | | Y_The1050 | | Z_The1050 | |
|---|---|---|---|---|---|---|
| | Δ (nT) | δ (%) | Δ (nT) | δ (%) | Δ (nT) | δ (%) |
| SIT | 60 | 145.7 | 717.3 | 554.5 | −910.9 | 7694.8 |
| LER | 30.9 | 46.7 | −43 | 0.4 | 125.3 | 608.5 |
| SPG* | −45.6 | 62 | 1.9 | 0.6 | 234.5 | 1146.8 |
| YAK* | −40.1 | 28.2 | 847.8 | 173.6 | 251.6 | 772.9 |
| UPS | 26.2 | 38.2 | −8.8 | 1.7 | 9.1 | 44.2 |
| BOX | −6.8 | 6.1 | −56.7 | 11.9 | 52.6 | 159 |
| EYR* | −35.5 | 30.5 | 35.1 | 13.7 | −54.3 | 130.8 |
| FRD | −5.7 | 22.6 | 23.9 | 17.6 | −41.1 | 347 |
| FRN | −1.3 | 6 | −10.8 | 10.5 | 53 | 434.6 |
| GNG | 13.7 | 18.3 | 10.3 | 0.3 | 24.6 | 71.3 |
| THY | 26.3 | 58.9 | −17.9 | 3.7 | 19.1 | 87.2 |
| AAA* | 2.1 | 2.9 | −6.9 | 0.9 | 246.3 | 699.3 |
| HBK* | −36.1 | 31 | 38 | 11.7 | 43.1 | 73.6 |
| IZN* | −113.1 | 299.4 | 37.8 | 10.4 | −13.8 | 59.6 |
| BMT* | −293.5 | 202.4 | 570 | 51.9 | −180.6 | 215.8 |
| SPT | −8.6 | 25.6 | 2.7 | 0 | 22.8 | 93.6 |
| KAK | −28.5 | 74.3 | −14.4 | 5.2 | 26.3 | 83 |
| SJG | 160.8 | 303.8 | 23.6 | 10.8 | −120.3 | 205.1 |
| IPM* | −290.5 | 588.5 | −215 | 116.4 | 460.6 | 697.4 |
| PHU* | −18.7 | 22 | −5.8 | 0.2 | 21.2 | 15.4 |
| BNG* | −130.4 | 323.5 | −93.8 | 6.5 | 16.8 | 12.2 |
| GUA | −105.3 | 266.5 | −77.9 | 1.3 | −28.4 | 15.2 |
| MBO | −30.6 | 78.2 | −69.2 | 18.5 | −43 | 11.4 |
| AAE* | −729 | 1880.7 | 123.5 | 12.4 | −531.3 | 79.2 |
| HUA* | −37.5 | 96.6 | 2.3 | 0.5 | 4.1 | 0.3 |

**Table 8.** Comparison of the model values of the crustal field components according to WDMAM with the values we obtained for the selected observatories from Table 1. Complete list is given in Table A6 of Appendix.

| IAGA code | X_WDMAM | | Y_WDMAM | | Z_WDMAM | |
|---|---|---|---|---|---|---|
| | Δ (nT) | δ (%) | Δ (nT) | δ (%) | Δ (nT) | δ (%) |
| SIT | −35.4 | 85.9 | 217.5 | 168.2 | −358.4 | 3027.3 |
| LER | 65.1 | 98.3 | −123.6 | 1.1 | 189.6 | 920.3 |
| SPG* | −110.4 | 150.2 | −3.2 | 0.9 | 165.8 | 810.8 |
| YAK* | 72.5 | 50.9 | 616.6 | 126.2 | 409.4 | 1257.6 |
| UPS | 29.3 | 42.7 | −20.3 | 3.8 | 44 | 214 |
| BOX | −10.1 | 9 | −66.7 | 14 | 12.2 | 36.8 |
| EYR* | −45.6 | 39.2 | 24.8 | 9.7 | −51.2 | 123.3 |
| FRD | −14 | 55.7 | 45.1 | 33.2 | −106.1 | 896.9 |
| FRN | −34.1 | 150.8 | 51.2 | 49.7 | 93.1 | 764.2 |
| GNG | 11.2 | 14.9 | 6.6 | 0.2 | 53.4 | 154.7 |
| THY | 12.7 | 28.6 | −19.9 | 4.2 | 29.2 | 133.3 |
| AAA* | −13.2 | 18.2 | −13.5 | 1.7 | 272.9 | 775 |
| HBK* | −38 | 32.6 | 12.2 | 3.7 | 89.8 | 153.4 |
| IZN* | −121.8 | 322.5 | 48.4 | 13.4 | −18.5 | 79.9 |
| BMT* | −322.7 | 222.6 | 592.5 | 54 | −159.8 | 190.9 |
| SPT | −2.4 | 7.2 | −8.8 | 0.1 | 29 | 119.3 |
| KAK | −31.7 | 82.9 | −49.3 | 18 | −13.7 | 43.2 |
| SJG | 182.3 | 344.5 | −71.4 | 32.6 | −38.2 | 65.1 |
| IPM* | −294.8 | 597.1 | −301.6 | 163.2 | 404.9 | 613.1 |
| PHU* | −16.3 | 19.2 | −4.4 | 0.2 | 48.3 | 35.2 |
| BNG* | −132.5 | 328.7 | −133.4 | 9.2 | 63.9 | 46.3 |
| GUA | −147.1 | 372.2 | −67.6 | 1.1 | −63 | 33.8 |
| MBO | −40.3 | 103 | −60.9 | 16.3 | −35.1 | 9.3 |
| AAE* | −732.2 | 1889 | 129.8 | 13 | −519.4 | 77.5 |
| HUA* | −41.9 | 107.9 | 5.7 | 1.2 | −21.2 | 1.6 |

**Table 9.** Comparison of the model values of the crustal field components according to xDLFI with the values we obtained for the selected observatories from Table 1. Complete list is given in Table A7 of Appendix.

| IAGA code | X_xDLFI | | Y_xDLFI | | Z_xDLFI | |
|---|---|---|---|---|---|---|
| | Δ (nT) | δ (%) | Δ (nT) | δ (%) | Δ (nT) | δ (%) |
| SIT | 271.1 | 658.4 | −101.4 | 78.4 | −35.7 | 301.7 |
| LER | 39.6 | 59.9 | −155.4 | 1.4 | −106.3 | 516 |
| SPG* | −95.9 | 130.4 | −75.4 | 21.8 | 284.6 | 1391.8 |
| YAK* | −45.7 | 32.1 | 1068.1 | 218.7 | 522.4 | 1604.9 |
| UPS | −60.4 | 88.2 | 17.2 | 3.2 | 323.6 | 1575.2 |
| BOX | 46.3 | 41.2 | −36.4 | 7.6 | 232.7 | 703.4 |
| EYR* | 26.4 | 22.7 | 62.2 | 24.4 | −163.8 | 394.3 |
| FRD | −113.8 | 453.6 | 14 | 10.3 | −44.4 | 374.9 |
| FRN | 75.5 | 334.1 | 65 | 63.1 | 146.9 | 1205.6 |
| GNG | 15.7 | 21 | 28.2 | 0.9 | −55.5 | 160.9 |
| THY | 12.9 | 28.8 | −16.4 | 3.4 | 75.3 | 343.3 |
| AAA* | −142.2 | 195.7 | 35.7 | 4.4 | 223.8 | 635.5 |
| HBK* | −41.6 | 35.7 | −4.8 | 1.5 | −116.8 | 199.4 |
| IZN* | −127.1 | 336.5 | 17.5 | 4.8 | −29.7 | 128.5 |
| BMT* | −351.3 | 242.3 | 587.1 | 53.5 | −170.9 | 204.2 |
| SPT | −9.7 | 29 | −5.9 | 0.1 | 0.4 | 1.5 |
| KAK | −9.8 | 25.5 | −84.4 | 30.8 | 122.6 | 386.6 |
| SJG | 21.8 | 41.1 | −51.5 | 23.5 | −215.9 | 368.2 |
| IPM* | −111.6 | 226 | −354.8 | 192 | 990.3 | 1499.4 |
| PHU* | 5.8 | 6.9 | −9.3 | 0.3 | 90.6 | 66 |
| BNG* | −185.7 | 460.8 | 38.6 | 2.7 | −105.6 | 76.7 |
| GUA | −157.7 | 399 | −76.4 | 1.2 | −67.1 | 35.9 |
| MBO | −134.2 | 343.3 | −29.5 | 7.9 | 33.3 | 8.9 |
| AAE* | −719.4 | 1856 | 102.2 | 10.2 | −547.8 | 81.7 |
| HUA* | −23.6 | 60.7 | −4.8 | 1 | 65.3 | 5 |

**Table 10.** Comparison of the model values of the crustal field components according to EMM2017 with the values we obtained for the selected observatories from Table 1. Complete list is given in Table A8 of Appendix.

| IAGA code | X_EMM2017 | | Y_ EMM2017 | | Z_ EMM2017 | |
|---|---|---|---|---|---|---|
| | Δ (nT) | δ (%) | Δ (nT) | δ (%) | Δ (nT) | δ (%) |
| SIT | 42.9 | 104.3 | 7.1 | 5.5 | 10.3 | 87.1 |
| LER | 170.9 | 258.2 | −213.3 | 1.9 | 72.7 | 352.9 |
| SPG* | 9.9 | 13.4 | −76 | 22 | 248.9 | 1217.2 |
| YAK* | 32.7 | 23 | 445 | 91.1 | 3647.1 | 11204.2 |
| UPS | 22.2 | 32.4 | −31.5 | 5.9 | 96.3 | 468.8 |
| BOX | 87.7 | 78 | 2.5 | 0.5 | 184.2 | 556.8 |
| EYR* | 2.7 | 2.3 | 16 | 6.3 | −131.4 | 316.2 |
| FRD | 0.7 | 2.8 | 36.8 | 27.1 | −92 | 777.3 |
| FRN | 110 | 486.8 | 27.8 | 27 | 147.3 | 1209 |
| GNG | 51.3 | 68.5 | 7.8 | 0.3 | 16.7 | 48.5 |
| THY | −17.3 | 38.7 | 4.1 | 0.8 | 7.5 | 34.3 |
| AAA* | −51.6 | 71.1 | 31.8 | 3.9 | 283.3 | 804.3 |
| HBK* | −67 | 57.5 | 20.1 | 6.2 | −43.2 | 73.9 |
| IZN* | −73.1 | 193.4 | −31.3 | 8.7 | 3.8 | 16.7 |
| BMT* | −309.6 | 213.6 | 646.1 | 58.9 | −197.7 | 236.1 |
| SPT | −27.3 | 81.7 | 16.6 | 0.2 | 14.9 | 61.4 |
| KAK | −37.9 | 98.8 | −23.7 | 8.7 | 50.3 | 158.5 |
| SJG | −17.7 | 33.4 | −111.1 | 50.7 | 9.4 | 16 |
| IPM* | −65 | 131.7 | −210.3 | 113.8 | 581.2 | 879.9 |
| PHU* | −23 | 27 | −18.6 | 0.7 | 31.2 | 22.7 |
| BNG* | −99.5 | 247 | −163.3 | 11.3 | −19.3 | 14 |
| GUA | −137.1 | 347 | −80.6 | 1.3 | 3.3 | 1.7 |
| MBO | −71.5 | 182.8 | −30.1 | 8 | −77.5 | 20.6 |
| AAE* | −725.6 | 1872 | 106.2 | 10.6 | −564.8 | 84.2 |
| HUA* | −18.1 | 46.7 | 33.7 | 7.1 | −30.7 | 2.4 |

By analyzing the errors of the crustal field models, it is possible to trace the preservation of the error of the original measurements, used for their construction. For example, this applies to the observatories YAK, SIT, IPM, FRD and FRN – the relative error in determining crustal field components using the models under study can reach hundreds and thousands of percent (Tables 7-10). These errors do not have a pronounced latitude dependence, which is likely due to predominant contribution from the error in original aeromagnetic surveys. The absolute magnitude of $\Delta T$ error can exceed 100 nT, which is an order of magnitude greater than the error in modeling the main EMF in the auroral zone (IGRF-14, 2024), where space weather effects introduce the greatest distortion.

Table 11 shows the median relative errors of the considered anomalous crustal field models.

**Table 11.** Generalized assessment of the accuracy of the crustal field models for all observatories.

| Model | Median relative error (%) | | |
|---|---|---|---|
| | *X* | *Y* | *Z* |
| The1050 | 60.55 | 7.7 | 159.45 |
| WDMAM | 79.05 | 5.95 | 134.45 |
| xDLFI | 101.3 | 10.2 | 300.95 |
| EMM2017 | 90.95 | 6.35 | 213.65 |

Despite the degree and order of the xDLFI model is the highest, this model provides the lowest accuracy in estimation of all three components. At the same time, the WDMAM model, which provides only 800$^{th}$ degree and order of expansion, shows the highest accuracy in estimating $Y_a$ and $Z_a$ components. The models EMM2017 and WDMAM have similar degree and order of expansion (790 and 800 respectively), but differ in errors, especially in $Z$ component. This difference is caused by different initial data sets used for the model construction: EMM2017 model is based on EMAG2v3 grid, while WDMAM model is based on WDMAM anomaly grid. The WDMAM model tends to be the most accurate in terms of the sum of the median relative errors. From this perspective, models EMM2017 and xDLFI show the worst results, as the sum of their median relative errors exceeds 300 and 400 per cent, respectively. Fig. 14 graphically represents the discrepancies between the model predictions and the values we obtained for all 118 observatories under consideration.

Table 12 shows the sums of the absolute differences between our estimations and the model predictions for each component for all 118 observatories under consideration. Here, we exclude YAK observatory having the most significant outliers exceeding 3000 nT for $Z$ component according to the EMM2017 model (see Table 10 and Fig. 14). In terms of the absolute total error, the The1050 model is the most accurate, while the xDLFI model shows the worst results.

**Table 12.** Component-wise sums of the absolute differences between the crustal field estimations obtained in this study and the model predictions at all 118 observatories under consideration.

| Model | Sum of absolute discrepancies (nT) | | | |
|---|---|---|---|---|
| | *X* | *Y* | *Z* | Total |
| The1050 | 16787.3 | 13951.7 | 20175 | 50914 |
| WDMAM | 17351.2 | 14062.6 | 19736 | 51149.8 |
| xDLFI | 18731.9 | 15992.6 | 23803.3 | 58527.8 |
| EMM2017 | 18051.5 | 13740 | 20981.7 | 52773.2 |

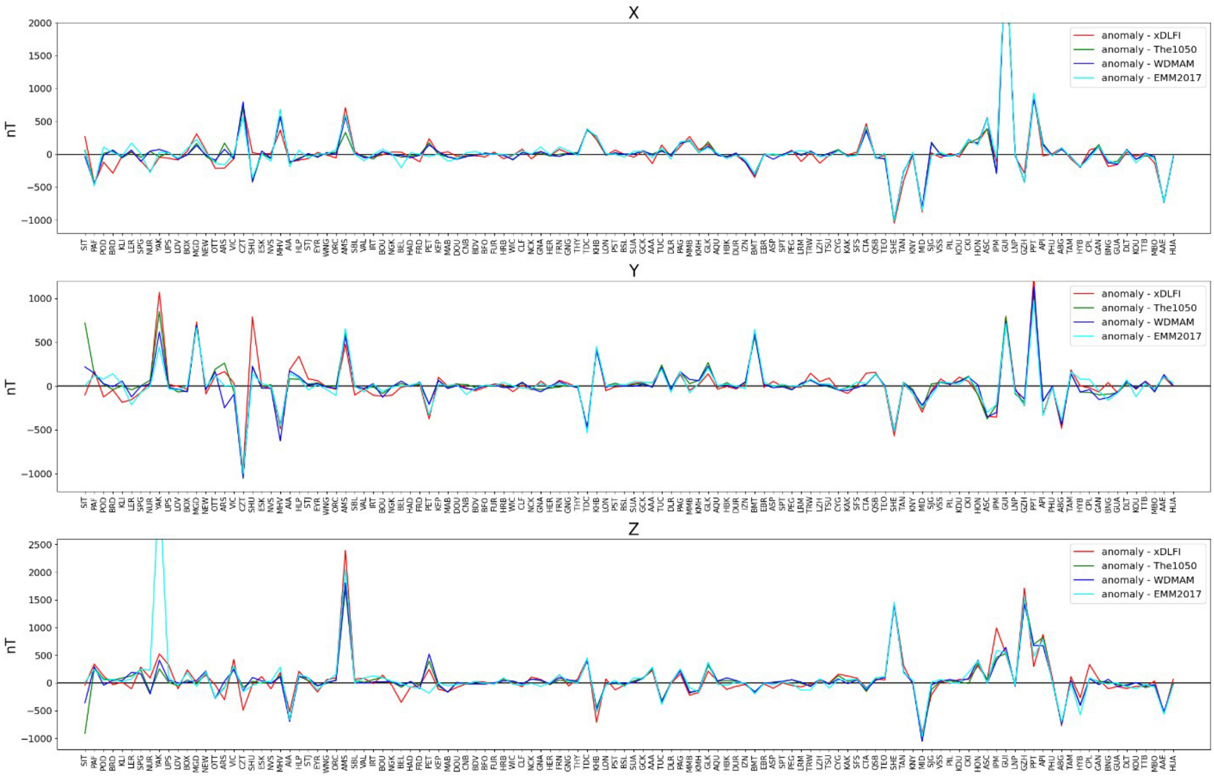


**Figure 14.** Component-wise differences between the crustal field estimations obtained in this study and the model predictions for all 118 observatories under consideration. The observatories are sorted by decreasing absolute quasi-dipole geomagnetic latitude from left to right.

## 7. Conclusions

The observed discrepancy between ground measurements and models based on satellite data is of a fundamental nature and is determined by regional features of the distribution of remanent and induced magnetization in the Earth's crust as well as the influence of external magnetospheric and ionospheric fields. Neglecting their contribution leads to errors in the models of the main EMF, reaching a total of 10%. We analyzed the temporal evolution of these discrepancies at 118 observatories for 28 years (from 1998 to 2025 inclusively). Separately, we identified long-term trends, reflecting different phases of the 11-year cycle of solar activity, and short-term variations with a period of about a year, associated with the rotation of the Earth around the Sun. The amplitudes of the latter also increase with increasing solar activity. It was shown that the calculated medians of the selected residual field values for each component are a reliable estimate of the contribution of the anomalous field of the Earth's crust at the observatories under consideration. Our results suggest that the method of Califf et al. (2022) for determining the crustal field corrections provides accurate results for observatories located at quasi-dipole geomagnetic latitudes lower than 60°.

Based on these findings, updated corrections for the anomalous crustal field were obtained for the three Cartesian components and declination at 118 observatories. For 65 observatories, such data were obtained for the first time. The largest values are observed in the $Z$ component. The same component shows the maximum changes over different epochs, which may indicate an induced magnetic field. Information on declination anomalies in the region is of critical importance for practical navigation tasks based on observations of the total EMF. Its value depends significantly not so much on the length of the anomalous crustal field vector as on its direction in the horizontal $XY$ plane.

We studied the influence of the data series length on the accuracy of determination of the crustal field contribution. This is crucial for some observatories, which possess continuous data recordings over limited time intervals. A computational experiment utilizing long-term observation series from 27 benchmark observatories of the INTERMAGNET network quantified the corresponding errors depending on the data availability period. Based on this approach we introduced the modified standard deviation $\sigma'$ parameter for estimating the reliability of the determined crustal field values. This methodological enhancement enabled the estimation of the preliminary corrections for the crustal field at observatories, which were set in operation not that long ago.

The results of comparison of the derived corrections with similar results obtained for 2000-2009 (Verbanac et al., 2015) and 1998-2020 (Califf et al., 2022) show that the crustal field as a whole has not changed much over the past three decades, but for some components and observatories the deviations exceeded $3\sigma'$. This is due to the slow induction produced by the time-varying core field, which leads also to time variations of the lithospheric field (Sebera et al., 2019). This once again emphasizes the importance of periodically updating the contribution of the anomalous crustal field at magnetic observatories. The obtained data also made it possible to estimate the accuracy of existing models of the anomalous crustal field. Analysis of the values of its individual components according to the The1050, WDMAM, xDLFI and EMM2017 models at the observatory sites suggests that the main contribution to the error in determining the magnetic declination of the total field is made by its crustal component, which is highly susceptible to large errors in the original measurements. The magnitude of declination error can reach several degrees.

As noted above, numerical evaluation and consideration of the contribution of the anomalous crustal field are extremely important in constructing accurate models of the secular variation of the main EMF based on observatory data. Moreover, this knowledge provides additional information on the distribution of anomaly sources in the Earth's crust associated with rocks and other geological structures, and also allows one to form a more detailed idea on the origin of the region and the spatiotemporal features of the EMF. Accurate values of the three components of the anomalous crustal field are important boundary conditions in solving the inverse problem of magnetometry based only on scalar observations. The magnetic properties of the geological section are also important for estimating the contribution of geomagnetically induced currents during strong geomagnetic disturbances (Pilipenko at al., 2023).

**Data availability statement.**

The initial data from magnetic observatories, which are transmitted and stored at the Interregional Analytical Geomagnetic Data Center, are available on the website http://mag.gcras.ru/.

Minute data from the observatories of the international INTERMAGNET network are available on the website https://intermagnet.org.

Hourly means from the observatories are available on the website of the World Data Centre for Geomagnetism in Edinburgh (https://wdc.bgs.ac.uk/).

Kp-index values are available on the website of the Helmholtz Centre for Geosciences https://kp.gfz.de/en/data#c222.

Data on the interplanetary magnetic field are available on the website of the Goddard Space Flight Center https://omniweb.gsfc.nasa.gov/.

RC-index values are available on the Technical University of Denmark website https://www.spacecenter.dk/files/magnetic-models.

The coefficients of the CHAOS-8.2 model in MatLab format are available on the Technical University of Denmark website https://www.spacecenter.dk/files/magnetic-models/CHAOS-8/.

Digital map of magnetic anomalies WDMAM 2.2 and the coefficients of the underlying model are available on the website http://www.wdmam.org.

Digital map of magnetic anomalies EMAG2v3 is available on the NOAA web resource https://www.ncei.noaa.gov/products/earth-magnetic-model-anomaly-grid-2.

Digital map of magnetic anomalies VSEGEI is available in the archive of the World Data Center for Solid Earth Physics in Moscow (http://wdcb.ru/sep).

The authors used data and services of the Collective Use Center "Analytical Geomagnetic Data Center" of the Geophysical Center of the Russian Academy of Sciences (https://ckp.gcras.ru/).

**Acknowledgements.** The research was carried out within the framework of the Russian Science Foundation project No. 24-17-00346. We express gratitude to two anonymous reviewers for their detailed study of the manuscript and numerous valuable comments.

## References


Alken, P., E. Thébault, C. D. Beggan, H. Amit et al. (2021). International Geomagnetic Reference Field: the thirteenth generation, Earth Planets Space, 73, 49, doi:10.1186/s40623-020-01288-x.

Bakhvalov, N. S., N. P. Zhidkov and G. M. Kobel'kov (1987). Numerical methods. Textbook. (Chislennye metody. Uchebnoe posobie), Nauka, Moscow.

Bartels, J., N. H. Heck and H. F. Johnston (1939). The three-hour-range index measuring geomagnetic activity, J. Geophys. Res., 44, 4, 411-454.

Bloxham, J. and D. Gubbins (1985). Geomagnetic field analysis III. Magnetic fields on the core-mantle boundary, Geophys. J. R. Astr. Soc., 80, 695-713, doi:10.1111/j.1365-246X.1985.tb05119.x.

Bloxham, J. and D. Gubbins (1986). Geomagnetic field analysis-IV. Testing the frozen-flux hypothesis, Geophys. J. R. Astr. Soc., 84, 139-152, doi:10.1111/j.1365-246X.1986.tb04349.x.

Bracke, S. (Ed.) (2025). INTERMAGNET Technical Reference Manual, Version 5.2.0.

Califf, S., P. Alken, A. Chulliat, B. Anderson et al. (2022). Investigation of geomagnetic reference models based on the Iridium constellation, Earth Planets Space, 74, 37, doi:10.1186/s40623-022-01574-w.

Finlay, C. C., C. Kloss, N. Olsen, M. D. Hammer et al. (2020). The CHAOS-7 geomagnetic field model and observed changes in the South Atlantic Anomaly, Earth Planets Space, 72, 156, doi:10.1186/s40623-020-01252-9.

Gvishiani, A. and A. Soloviev (2020). Observations, Modeling and Systems Analysis in Geomagnetic Data Interpretation, Springer, doi:10.1007/978-3-030-58969-1.

International Association of Geomagnetism and Aeronomy (2024). IGRF-14, Zenodo, doi:10.5281/zenodo.14218973.

Ivanov, M. M., N. E. Malinina, M. S. Penkevich and V. I. Pochtarev (1957). Magnitnoe pole Zemli: T. 1. Istoriya organizatsii i opisaniya rabot po general'noi magnitnoi s"emke SSSR (The Earth's Magnetic Field: Vol. 1. A History of the Organization and Description of USSR General Magnetic Survey Works), Leningrad: Gimez, 1957

Jacobs, J. A. (1987). Geomagnetism, vol. 2, Academic Press, London.

Karinen, A. and K. Mursula (2005). A new reconstruction of the Dst index for 1932-2002, Ann. Geophysicae, 23, 2, 475-485.

Khomutov, S. Y. (2025). Problems of Processing of Raw Data from Magnetic Observatories: Will Modern Mathematical Technologies Help?, Russ. J. Earth Sci., 2, 1-5, doi:10.2205/2025ES000994.

Ku, H. H. (1966). Notes on the use of propagation of error formulas, Journal of Research of the National Bureau of Standards, 70C,4, 262, doi:10.6028/jres.070c.025, ISSN 0022-4316.

Kudin, D. V., A. A. Soloviev, R. V. Sidorov, V. I. Starostenko et al. (2021). Advanced production of quasi-definitive magnetic observatory data of the INTERMAGNET standard, Geomagn. Aeron., 61, 1, 54-67, doi:10.1134/S0016793221010096.

Kudin, D., A. Soloviev, M. Matveev and O. Shevaldysheva (2023). On a novel approach to correcting temperature dependencies in magnetic observatory data, Appl. Sci., 13, 8008, doi:10.3390/app13148008.

Langel, R. A., R. H. Estes and G. D. Mead (1982). Some new methods in geomagnetic field modeling applied to the 1960-1980 epoch, J. Geomag. Geoelectr., 34, 327-349.

Lesur, V. and D. Gubbins (2000). Using geomagnetic secular variation to separate remanent and induced sources of the crustal magnetic field, Geophys. J. Int., 142, 889-897.

Lesur, V., M. Hamoudi, Y. Choi, J. Dyment et al. (2016). Building the second version of the World Digital Magnetic Anomaly Map (WDMAM), Earth Planet Space, 68, 27, doi:10.1186/s40623-016-0404-6.

Love, J. J. and A. Chulliat (2013). An International Network of Magnetic Observatories, Eos Trans. AGU, 94, 373-374, doi:10.1002/2013EO420001.

Mandea, M. and B. Langlais (2002). Observatory crustal magnetic biases during MAGSAT and Oersted satellite missions, Geophys. Res. Lett., 29, 11-15.

Merrill, R., M. McElhinny and P. McFadden (1998). The Magnetic Field of the Earth: Paleomagnetism, the Core, and the Deep Mantle, Academic Press, San Diego.

Meyer, B., A. Chulliat and R. Saltus (2017). Derivation and error analysis of the earth magnetic anomaly grid at 2 arc min resolution version 3 (EMAG2v3), Geochem. Geophys. Geosyst., 18, 4522-4537, doi:10.1002/2017GC007280.

Olsen, N. and A. Kuvshinov (2004). Modeling the ocean effect of geomagnetic storms, Earth Planets Space, 56, 525-530, doi:10.1186/BF03352512.

Olsen, N., H. Lühr, C. C. Finlay, T. J. Sabaka et al. (2014). The CHAOS-4 geomagnetic field model, Geophys. J. Int., 197, 2, 815-827.

Onovughe, E. (2018). Usage of RC index as a Good Representation for Characterising Rapid Variation Signals in Geomagnetic Field Studies, Sun and Geosphere, 13, 1, 77-87.

Peltier, A. and A. Chulliat (2010). On the feasibility of promptly producing quasi-definitive magnetic observatory data, Earth Planets Space, 62, 2, e5-e8, doi:10.5047/eps.2010.02.002.

Pilipenko, V. A., A. A. Chernikov, A. A. Soloviev, N. V. Yagova et al. (2023) Influence of Space Weather on the Reliability of the Transport System Functioning at High Latitudes. Russian J. Earth Sci. 2, 1-34.

Sabaka, T. J., N. Olsen and R. A. Langel (2002). A comprehensive model of the quiet-time, near-Earth magnetic field: phase 3, Geophys. J. Int., 151, 32-68.

Sabaka, T. J., N. Olsen and M. E. Purucker (2004). Extending comprehensive models of the Earth's magnetic field with Ørsted and CHAMP data, Geophys. J. Int., 159, 2, 521-547, doi:10.1111/j.1365-246x.2004.02421.x.

Sebera, J., R. Haagmans, E. Bakyiev and A. Bezdek (2019). On the Observability of the Time-Variable Lithospheric Signal in Satellite Magnetic Data, Surv. Geophys. 40, 5, 1-15, doi:10.1007/s10712-019-09546-8.

Thébault, E., G. Hulot, B. Langlais and P. Vigneron (2021). A spherical harmonic model of Earth's lithospheric magnetic field up to degree 1050, Geophys. Res. Lett., 48, e2021GL095147, doi:10.1029/2021GL095147.

Thébault, E. and G. Hulot (2025). Unraveling the lithospheric magnetic field masked by the Earth's main field by estimating the magnetization and magnetic crustal thickness using a statistical approach, Phys. Earth Planet. Int., 366, 107421, doi:10.1016/j.pepi.2025.107421.

Verbanac, G., M. Korte and M. Mandea (2007). On long-term trends of the European geomagnetic observatory biases, Earth Planets Space, 59, 685-695.

Verbanac, G., M. Mandea, M. Bandic and S. Subasic (2015). Magnetic observatories: biases over CHAMP satellite mission, Solid Earth, 6, 2, 775-781.

# Appendix A.

**Table A1.** Complete list of observatories under consideration, their geodetic coordinates and time intervals of the analyzed data. In all tables, the observatories are sorted by decreasing absolute quasi-dipole geomagnetic latitude (GM Lat) given for 2025.0 epoch. The observatories for which the corrections for the anomalous crustal field are published for the first time are marked with an asterisk.

| № | IAGA code | GM Lat (°) | Lat (°) | Lon (°) | Alt (km) | Start Date (yyyy-mm-dd) | End Date (yyyy-mm-dd) | Duration (years) |
|---|---|---|---|---|---|---|---|---|
| 1 | SIT | 59.3 | 57.06 | −135.33 | 0.02 | 2004-03-02 | 2019-12-30 | 15.83 |
| 2 | PAF | −58.52 | −49.4 | 70.3 | 0.04 | 2004-03-03 | 2013-12-31 | 9.83 |
| 3 | POD* | 58.32 | 61.58 | 90.03 | 0.03 | 2016-02-26 | 2016-07-14 | 0.5 |
| 4 | BRD* | 58.27 | 49.87 | −99.97 | 0.38 | 2014-01-01 | 2019-12-30 | 5.92 |
| 5 | KLI* | 57.63 | 60.85 | 39.52 | 0.14 | 2019-01-01 | 2023-12-31 | 5 |
| 6 | LER | 57.52 | 60.14 | −1.18 | 0.09 | 2004-04-01 | 2021-12-31 | 17.75 |
| 7 | SPG* | 57.28 | 60.54 | 29.72 | 0.05 | 2016-01-03 | 2024-12-31 | 8.92 |
| 8 | NUR* | 57.25 | 60.51 | 24.66 | 0.11 | 2004-03-03 | 2019-12-31 | 1.83 |
| 9 | YAK* | 57.18 | 61.96 | 129.66 | 0.1 | 2011-01-01 | 2018-12-31 | 8 |
| 10 | UPS | 56.65 | 59.9 | 17.35 | 0.05 | 2004-03-03 | 2019-12-31 | 15.83 |
| 11 | LOV* | 56.03 | 59.34 | 17.82 | 0.03 | 1998-04-01 | 2004-04-14 | 5.75 |
| 12 | BOX | 54.75 | 58.07 | 38.23 | 0.12 | 2004-04-29 | 2022-04-18 | 17.58 |
| 13 | MGD | 54.4 | 60.05 | 150.73 | 0.23 | 2012-01-02 | 2022-04-20 | 10.17 |
| 14 | NEW | 54.1 | 48.27 | −117.12 | 0.77 | 2004-03-02 | 2019-12-30 | 15.83 |
| 15 | OTT | 53.64 | 45.4 | −75.55 | 0.07 | 1998-01-01 | 2021-12-31 | 22.75 |
| 16 | ARS* | 53.27 | 56.43 | 58.57 | 0.29 | 2004-03-03 | 2018-12-31 | 9.83 |
| 17 | VIC | 53.17 | 48.52 | −123.42 | 0.18 | 2004-03-02 | 2019-12-30 | 15.83 |
| 18 | CZT | −53.16 | −46.43 | 51.86 | 0.16 | 2004-03-03 | 2015-12-30 | 11.83 |
| 19 | SHU | 53.1 | 55.35 | −160.46 | 0.08 | 2005-01-06 | 2020-12-31 | 15.83 |
| 20 | ESK | 52.04 | 55.31 | −3.21 | 0.24 | 2004-03-01 | 2021-12-31 | 17.83 |
| 21 | NVS | 51.62 | 54.85 | 83.23 | 0.13 | 2004-03-03 | 2023-04-08 | 19.17 |
| 22 | MHV* | 51.5 | 54.96 | 37.77 | 0.17 | 2023-07-12 | 2025-08-04 | 2.17 |
| 23 | AIA* | −51.45 | −65.25 | −64.27 | 0.01 | 2021-01-01 | 2021-12-31 | 1 |
| 24 | HLP | 50.81 | 54.61 | 18.82 | 0 | 2004-03-03 | 2019-12-31 | 15.67 |
| 25 | STJ | 50.58 | 47.59 | −52.68 | 0.1 | 2012-01-02 | 2019-12-31 | 7.83 |
| 26 | EYR* | −49.94 | −43.47 | 172.39 | 0.1 | 2005-03-01 | 2020-12-31 | 15.58 |
| 27 | WNG | 49.82 | 53.73 | 9.05 | 0.07 | 2004-03-03 | 2019-12-31 | 15.83 |
| 28 | ORC* | −49.42 | −60.74 | −44.74 | 0.01 | 2019-01-02 | 2019-12-31 | 1 |
| 29 | AMS* | −48.73 | −37.8 | 77.57 | 0.05 | 2004-03-03 | 2009-12-31 | 5.83 |
| 30 | SBL | 48.59 | 43.93 | −60.01 | 0.01 | 2013-01-01 | 2019-12-30 | 7 |
| 31 | VAL | 48.42 | 51.94 | −10.25 | 0.01 | 2002-01-02 | 2003-10-12 | 1.83 |
| 32 | IRT* | 48.41 | 52.17 | 104.45 | 0.48 | 2015-01-09 | 2019-12-30 | 5 |
| 33 | BOU | 48.08 | 40.14 | −105.24 | 1.68 | 2004-03-02 | 2021-12-31 | 17.83 |

| № | IAGA code | GM Lat (°) | Lat (°) | Lon (°) | Alt (km) | Start Date (yyyy-mm-dd) | End Date (yyyy-mm-dd) | Duration (years) |
|---|---|---|---|---|---|---|---|---|
| 34 | NGK | 47.91 | 52.07 | 12.68 | 0.08 | 2004-03-03 | 2019-12-31 | 15.83 |
| 35 | BEL | 47.75 | 51.84 | 20.79 | 0.18 | 2004-03-03 | 2019-12-31 | 15.75 |
| 36 | HAD | 46.95 | 50.99 | −4.48 | 0.1 | 2007-06-08 | 2019-12-31 | 12.58 |
| 37 | FRD | 46.9 | 38.2 | −77.37 | 0.07 | 2004-02-29 | 2019-12-30 | 15.92 |
| 38 | PET | 46.72 | 52.97 | 158.25 | 0.05 | 2009-09-25 | 2022-04-08 | 12.58 |
| 39 | KEP | −46.23 | −54.28 | −36.49 | 0.01 | 2013-01-01 | 2019-12-31 | 7 |
| 40 | MAB* | 45.85 | 50.3 | 5.68 | 0.44 | 2005-01-01 | 2006-12-31 | 2 |
| 41 | DOU | 45.62 | 50.1 | 4.6 | 0.23 | 2004-03-03 | 2019-12-31 | 13.83 |
| 42 | CNB | −45.04 | −35.31 | 149.36 | 0.86 | 2004-03-03 | 2019-12-30 | 15.83 |
| 43 | BDV* | 44.48 | 49.08 | 14.02 | 0.5 | 2014-01-03 | 2019-12-31 | 6 |
| 44 | BFO* | 43.52 | 48.33 | 8.32 | 0.64 | 2014-01-03 | 2019-12-31 | 6 |
| 45 | FUR* | 43.36 | 48.16 | 11.28 | 0.57 | 2004-03-03 | 2019-12-31 | 15.83 |
| 46 | HRB | 43.2 | 47.88 | 18.19 | 0.11 | 1998-01-01 | 2003-10-12 | 5.83 |
| 47 | WIC | 43.19 | 47.93 | 15.86 | 1.09 | 2015-01-01 | 2019-12-31 | 5 |
| 48 | CLF | 43.17 | 48.02 | 2.26 | 0.14 | 1998-01-01 | 2019-12-31 | 21.67 |
| 49 | NCK* | 42.87 | 47.63 | 16.72 | 0.15 | 1998-01-01 | 2003-10-12 | 5.83 |
| 50 | GNA | −42.79 | −31.78 | 115.95 | 0.06 | 2004-03-03 | 2012-12-31 | 8.83 |
| 51 | HER | −42.72 | −34.42 | 19.23 | 0.03 | 2004-03-03 | 2019-12-31 | 15.83 |
| 52 | FRN | 42.55 | 37.09 | −119.72 | 0.33 | 2004-03-02 | 2019-12-30 | 15.83 |
| 53 | GNG | −42.31 | −31.36 | 115.72 | 0.05 | 2012-01-02 | 2019-12-30 | 7.75 |
| 54 | THY | 42.07 | 46.9 | 17.89 | 0.19 | 2004-03-03 | 2019-12-31 | 15.83 |
| 55 | TDC* | −41.72 | −37.07 | −12.32 | 0.04 | 2009-10-03 | 2016-10-23 | 7 |
| 56 | KHB | 41.68 | 47.61 | 134.69 | 0.09 | 2014-06-10 | 2021-10-15 | 7.42 |
| 57 | LON* | 40.31 | 45.41 | 16.66 | 0.1 | 2016-01-03 | 2020-12-29 | 4.67 |
| 58 | PST | −40.15 | −51.7 | −57.89 | 0.14 | 2015-01-01 | 2019-12-31 | 5 |
| 59 | BSL* | 40.06 | 30.35 | −89.64 | 0.01 | 2007-01-13 | 2019-12-30 | 13 |
| 60 | SUA* | 39.95 | 44.68 | 26.25 | 0.08 | 2009-03-01 | 2021-12-31 | 12.83 |
| 61 | GCK* | 39.6 | 44.63 | 20.77 | 0.23 | 2007-01-01 | 2013-12-30 | 7 |
| 62 | AAA* | 39.52 | 43.25 | 76.92 | 1.3 | 2005-01-06 | 2014-12-31 | 10 |
| 63 | TUC | 39.22 | 32.17 | −110.73 | 0.95 | 2004-03-02 | 2019-12-30 | 15.83 |
| 64 | DLR* | 38.1 | 29.49 | −100.92 | 0.35 | 2004-02-29 | 2007-08-30 | 3.58 |
| 65 | PAG* | 37.39 | 42.52 | 24.18 | 0.56 | 2007-01-01 | 2019-12-31 | 12.83 |
| 66 | MMB | 37.2 | 43.91 | 144.19 | 0.04 | 2004-03-03 | 2019-12-30 | 15.83 |
| 67 | KMH* | −36.99 | −26.54 | 18.11 | 1.06 | 2009-01-01 | 2019-12-31 | 10.92 |
| 68 | GLK* | 36.9 | 40.94 | 44.48 | 1.47 | 2020-02-08 | 2021-01-09 | 1 |
| 69 | AQU* | 36.62 | 42.38 | 13.32 | 0.68 | 2004-03-03 | 2009-12-31 | 5.83 |
| 70 | HBK* | −36.02 | −25.88 | 27.71 | 1.55 | 2004-03-03 | 2019-12-31 | 15.58 |
| 71 | DUR* | 35.82 | 41.65 | 14.47 | 0.92 | 2016-01-03 | 2019-12-31 | 4 |

| № | IAGA code | GM Lat (°) | Lat (°) | Lon (°) | Alt (km) | Start Date (yyyy-mm-dd) | End Date (yyyy-mm-dd) | Duration (years) |
|---|---|---|---|---|---|---|---|---|
| 72 | IZN* | 35.51 | 40.5 | 29.72 | 0.26 | 2007-01-01 | 2019-12-31 | 12.83 |
| 73 | BMT* | 35.43 | 40.3 | 116.2 | 0.18 | 2010-01-01 | 2019-12-30 | 10 |
| 74 | EBR | 34.57 | 40.96 | 0.33 | 0.53 | 2012-02-01 | 2019-12-31 | 7.92 |
| 75 | ASP | −33.47 | −23.76 | 133.88 | 0.56 | 1999-01-03 | 2021-12-31 | 21.58 |
| 76 | SPT | 32.85 | 39.55 | −4.35 | 0.92 | 2004-03-01 | 2019-12-31 | 15.67 |
| 77 | PEG* | 32.32 | 38.08 | 23.93 | 0.38 | 2012-01-02 | 2013-12-30 | 2 |
| 78 | LRM | −31.92 | −22.22 | 114.1 | 0 | 2013-04-01 | 2019-12-30 | 6.75 |
| 79 | TRW* | −31.57 | −43.27 | −65.38 | 0.01 | 2004-02-29 | 2006-12-31 | 2.92 |
| 80 | LZH* | 31.57 | 36.09 | 103.84 | 1.56 | 2008-01-01 | 2019-04-22 | 11.17 |
| 81 | TSU* | −30.94 | −19.2 | 17.58 | 1.27 | 2013-03-07 | 2017-12-31 | 4.58 |
| 82 | CYG | 30.48 | 36.37 | 126.85 | 0.17 | 2014-01-03 | 2017-12-31 | 4 |
| 83 | KAK | 29.32 | 36.23 | 140.19 | 0.04 | 2004-03-03 | 2019-12-30 | 15.83 |
| 84 | SFS | 29.27 | 36.67 | −5.94 | 0.11 | 2005-01-01 | 2019-12-31 | 15 |
| 85 | CTA | −29.02 | −20.09 | 146.26 | 0.37 | 2004-03-03 | 2015-07-16 | 11.42 |
| 86 | QSB* | 28.65 | 33.87 | 35.64 | 0.53 | 2004-03-03 | 2007-11-19 | 3.67 |
| 87 | TEO* | 28.59 | 19.75 | −99.18 | 2.28 | 2002-08-04 | 2003-10-13 | 1.25 |
| 88 | SHE* | −28.29 | −15.96 | −5.75 | 0.59 | 2014-01-03 | 2019-12-31 | 6 |
| 89 | TAN* | −28.03 | −18.92 | 47.55 | 1.38 | 1998-04-02 | 2003-10-12 | 5.5 |
| 90 | KNY | 24.97 | 31.42 | 130.88 | 0.11 | 2004-03-03 | 2019-12-30 | 15.83 |
| 91 | MID* | 24.46 | 28.21 | −177.38 | 0 | 2000-02-10 | 2002-02-27 | 1.83 |
| 92 | SJG | 24.43 | 18.11 | −66.15 | 0.42 | 2004-02-29 | 2016-12-30 | 12.92 |
| 93 | VSS* | −22.24 | −22.4 | −43.65 | 0.46 | 2010-03-23 | 2019-12-31 | 7.67 |
| 94 | PIL* | −21.55 | −31.67 | −63.88 | 0.33 | 2012-01-01 | 2019-12-30 | 7.83 |
| 95 | KDU | −21.41 | −12.69 | 132.47 | 0.01 | 2004-11-28 | 2019-12-28 | 15 |
| 96 | CKI | −21.26 | −12.19 | 96.83 | 0.01 | 2013-01-01 | 2019-12-30 | 6.33 |
| 97 | HON | 21.21 | 21.32 | −158 | 0 | 2004-03-03 | 2019-12-30 | 15.83 |
| 98 | ASC | −20.67 | −7.95 | −14.38 | 0.18 | 2013-01-01 | 2019-12-31 | 6.67 |
| 99 | IPM* | −19.55 | −27.17 | −109.42 | 0.08 | 2010-01-01 | 2015-09-14 | 5.67 |
| 100 | GUI* | 19.19 | 28.32 | −16.44 | 0.87 | 2004-03-01 | 2019-12-31 | 15.5 |
| 101 | LNP* | 19.1 | 25 | 121.17 | 0.1 | 1998-01-01 | 2000-12-30 | 3 |
| 102 | GZH* | 18.52 | 23.97 | 112.45 | 0.01 | 2003-02-05 | 2005-12-30 | 2.25 |
| 103 | PPT | −16.12 | −17.57 | −149.57 | 0.36 | 2004-03-02 | 2019-06-18 | 15.25 |
| 104 | API* | −15.61 | −13.82 | −171.78 | 0 | 2012-01-02 | 2018-12-31 | 7 |
| 105 | PHU* | 15.53 | 21.03 | 105.96 | 0.01 | 2005-01-06 | 2010-05-13 | 5.25 |
| 106 | ABG | 12.88 | 18.62 | 72.87 | 0.01 | 2004-03-03 | 2019-12-31 | 11.75 |
| 107 | TAM | 12.72 | 22.79 | 5.53 | 1.37 | 2006-01-03 | 2021-12-31 | 14.58 |
| 108 | HYB | 11.37 | 17.41 | 78.55 | 0.5 | 2009-01-01 | 2012-12-31 | 4 |
| 109 | CPL* | 11.23 | 17.29 | 78.92 | 0.36 | 2021-01-01 | 2021-12-31 | 0.92 |

| № | IAGA code | GM Lat (°) | Lat (°) | Lon (°) | Alt (km) | Start Date (yyyy-mm-dd) | End Date (yyyy-mm-dd) | Duration (years) |
|---|---|---|---|---|---|---|---|---|
| 110 | GAN* | −8.53 | −0.69 | 73.15 | 0 | 2012-01-01 | 2019-12-31 | 7.67 |
| 111 | BNG* | −7.06 | 4.33 | 18.57 | 0.4 | 1998-01-01 | 2003-10-12 | 5.83 |
| 112 | GUA | 5.91 | 13.59 | 144.87 | 0.14 | 2004-03-03 | 2020-12-31 | 16.75 |
| 113 | DLT | 5.82 | 11.95 | 108.48 | 1.58 | 2012-01-02 | 2018-12-31 | 6.33 |
| 114 | KOU | 5.58 | 5.21 | −52.73 | 0.01 | 2004-04-01 | 2019-12-31 | 15.75 |
| 115 | TTB* | −2.62 | −1.21 | −48.51 | 0.01 | 2018-01-01 | 2021-12-31 | 4 |
| 116 | MBO | 2.49 | 14.39 | −16.96 | 0.01 | 1998-01-03 | 2018-08-03 | 20.33 |
| 117 | AAE* | 1.37 | 9.04 | 38.77 | 2.44 | 2004-03-03 | 2013-12-31 | 9.75 |
| 118 | HUA* | −1.15 | −12.04 | −75.32 | 3.34 | 2013-09-01 | 2021-12-30 | 8.33 |

**Table A2.** Calculated corrections for anomalous crustal field by components $X_a$, $Y_a$, $Z_a$ (nT) and declination $D_a$ (°) ($D_a$ is valid for 2025.0 epoch), as well as the obtained values of the MSDs.

| IAGA code | $X_a$ (nT) | $Y_a$ (nT) | $Z_a$ (nT) | $D_a$ (°) | MSD($X_a$) (nT) | MSD($Y_a$) (nT) | MSD($Z_a$) (nT) | MSD($D_a$) (°) |
|---|---|---|---|---|---|---|---|---|
| SIT | 19.7 | −14.7 | −91.3 | 0.1 | 2.2 | 2.6 | 4.2 | 0.009 |
| PAF | 466.2 | −143.2 | −274.7 | 1 | 3.1 | 3.4 | 5.9 | 0.01 |
| POD* | 38.4 | −3.8 | −295.7 | 0 | 8.1 | 12.7 | 11.8 | 0.066 |
| BRD* | 7.3 | −60.7 | 46 | 0.2 | 4.1 | 8.3 | 9.8 | 0.031 |
| KLI* | 54.7 | 148.6 | −202.6 | 0.5 | 3.9 | 7.8 | 9.6 | 0.03 |
| LER | −121.2 | 178.5 | 34.5 | 0.7 | 3.3 | 2.9 | 2.2 | 0.011 |
| SPG* | 200.9 | −75 | −188.9 | 0.4 | 4.8 | 5.9 | 7.6 | 0.023 |
| NUR* | 303.2 | −109.2 | 102 | 0.6 | 6.4 | 11.3 | 11.6 | 0.043 |
| YAK* | 53.9 | −1191.2 | 102.8 | 4.5 | 4.3 | 6 | 13 | 0.023 |
| UPS | 151.8 | −13.2 | −125.5 | 0.1 | 1.9 | 1.6 | 2.3 | 0.006 |
| LOV* | 54.4 | 0.5 | 4.2 | 0 | 5 | 9.1 | 10.8 | 0.034 |
| BOX | 4.4 | 2 | −353.8 | 0 | 4 | 2.4 | 2.8 | 0.009 |
| MGD | −271 | −682.9 | 33.4 | 2.4 | 3 | 4.2 | 6.1 | 0.014 |
| NEW | −23.1 | 114 | −123.4 | 0.4 | 1.4 | 2.2 | 2.1 | 0.007 |
| OTT | 143.3 | −126.2 | 126.5 | 0.3 | 2.6 | 2.3 | 2 | 0.007 |
| ARS* | 130.7 | −261.6 | 459.8 | 1 | 4.7 | 3.9 | 4.8 | 0.014 |
| VIC | 33.6 | 11.4 | −283 | 0 | 1.5 | 2.3 | 2.5 | 0.007 |
| CZT | −739.7 | 1088.6 | 150.7 | 0.3 | 4.2 | 3.3 | 4.9 | 0.013 |
| SHU | 414.6 | −233.5 | 27.7 | 0.9 | 5.2 | 5.2 | 2.4 | 0.015 |
| ESK | 20.2 | −31.8 | −61.4 | 0.1 | 2 | 1.6 | 1.4 | 0.005 |
| NVS | 75.1 | −56.4 | 16.8 | 0.2 | 1.9 | 1.9 | 2.1 | 0.007 |
| MHV* | −399.5 | 499.8 | −312.8 | 1.9 | 7.4 | 11.3 | 12 | 0.038 |
| AIA* | 94.9 | −95 | 430.1 | 0.3 | 7.4 | 12.5 | 11.7 | 0.035 |
| HLP | 63.9 | −165.5 | −103.6 | 0.6 | 3.5 | 3.7 | 4.4 | 0.012 |

| IAGA code | $X_a$ (nT) | $Y_a$ (nT) | $Z_a$ (nT) | $D_a$ (°) | MSD($X_a$) (nT) | MSD($Y_a$) (nT) | MSD($Z_a$) (nT) | MSD($D_a$) (°) |
|---|---|---|---|---|---|---|---|---|
| STJ | 52.8 | 41.7 | 14.8 | 0.2 | 3 | 6.2 | 8.5 | 0.017 |
| EYR* | 24.4 | −25.4 | 81.1 | 0.1 | 3.4 | 8.6 | 6 | 0.022 |
| WNG | 56.9 | 51.2 | −63.8 | 0.1 | 2.2 | 1.6 | 1.5 | 0.005 |
| ORC* | −17.6 | 12.5 | −3.5 | 0 | 7.1 | 12 | 11.7 | 0.039 |
| AMS* | −577.7 | −680.3 | −1983.6 | 2.8 | 3.9 | 7.1 | 9.6 | 0.019 |
| SBL | 11.5 | 12.4 | −83.8 | 0 | 3.1 | 6.2 | 8.4 | 0.016 |
| VAL | 130.7 | −42.8 | −25.4 | 0.1 | 6.9 | 12.1 | 11.8 | 0.035 |
| IRT* | 57 | 43.3 | −133.8 | 0.1 | 4.3 | 8.2 | 10.4 | 0.026 |
| BOU | 5.1 | 37.8 | −141.9 | 0.1 | 1.3 | 2 | 1.5 | 0.006 |
| NGK | −8.6 | 1.8 | −81.8 | 0 | 2.1 | 1.6 | 1.4 | 0.005 |
| BEL | 131.8 | 136.3 | 309.1 | 0.4 | 2.5 | 1.4 | 1.9 | 0.004 |
| HAD | −32.9 | 15.1 | 70.2 | 0 | 2.2 | 2.1 | 3.4 | 0.006 |
| FRD | 78.2 | −43.5 | 121.4 | 0.1 | 1.8 | 2.5 | 1.3 | 0.006 |
| PET | −292.7 | 256 | 129.4 | 0.6 | 2.6 | 5.1 | 4.2 | 0.013 |
| KEP | −23.8 | −45 | 86.6 | 0.2 | 4.8 | 6.2 | 8.2 | 0.023 |
| MAB* | 24.4 | −13.8 | 165.9 | 0 | 6.2 | 11.1 | 11.5 | 0.032 |
| DOU | 26.7 | −18 | 75.4 | 0.1 | 1.8 | 1.9 | 2.8 | 0.005 |
| CNB | 2.1 | 48 | 79.6 | 0.1 | 2.1 | 1.8 | 1.8 | 0.004 |
| BDV* | −17.4 | −11.9 | −46.1 | 0 | 3.8 | 6.9 | 9.2 | 0.019 |
| BFO* | 5.2 | −28.7 | −21.6 | 0.1 | 3.6 | 7 | 9.2 | 0.019 |
| FUR* | −4.8 | −5.5 | 6.9 | 0 | 3.6 | 1.9 | 1.6 | 0.005 |
| HRB | 36.3 | −20.5 | −86.9 | 0.1 | 5.4 | 9.3 | 10.7 | 0.025 |
| WIC | 12.7 | −3.5 | −16.9 | 0 | 4.2 | 7.9 | 9.9 | 0.021 |
| CLF | −59.3 | −15.3 | 99.6 | 0 | 1.8 | 2.5 | 1.5 | 0.007 |
| NCK* | −8.6 | 0.8 | −64.2 | 0 | 5.1 | 8.7 | 10.5 | 0.024 |
| GNA | −12.5 | −94.9 | 119.4 | 0.2 | 2.7 | 4.5 | 6.9 | 0.011 |
| HER | 30.5 | 8.1 | 26.6 | 0.1 | 2.6 | 1.6 | 2.3 | 0.01 |
| FRN | 9.3 | −16.6 | −246.6 | 0 | 3 | 2.6 | 4.4 | 0.007 |
| GNG | 5 | −38.5 | 173.5 | 0.1 | 3.2 | 6 | 8.3 | 0.014 |
| THY | −6.3 | −12.8 | −59.5 | 0 | 1.6 | 1.5 | 1.5 | 0.004 |
| TDC* | −377.5 | 524.3 | −429.3 | 2.1 | 3.3 | 6.4 | 8.7 | 0.037 |
| KHB | −282.9 | −430.5 | 613.6 | 1.1 | 3.3 | 6.1 | 8.3 | 0.014 |
| LON* | −18.3 | −3.9 | −36.1 | 0 | 4.7 | 8.9 | 10.5 | 0.023 |
| PST | 36.8 | −10.1 | 35.6 | 0 | 4.8 | 7.9 | 10 | 0.026 |
| BSL* | −71.9 | 30 | 42.5 | 0.1 | 2.4 | 2.6 | 5.1 | 0.006 |
| SUA* | 24 | −21.9 | −73.2 | 0.1 | 2.2 | 2.4 | 3.2 | 0.006 |
| GCK* | −29.5 | −44.4 | −88.1 | 0.1 | 3.3 | 6.4 | 8.5 | 0.016 |
| AAA* | 154.1 | 36 | −233.3 | 0.1 | 3.8 | 9.6 | 8 | 0.022 |

| IAGA code | $X_a$ (nT) | $Y_a$ (nT) | $Z_a$ (nT) | $D_a$ (°) | MSD($X_a$) (nT) | MSD($Y_a$) (nT) | MSD($Z_a$) (nT) | MSD($D_a$) (°) |
|---|---|---|---|---|---|---|---|---|
| TUC | −78.9 | −264.9 | 408.6 | 0.6 | 1.6 | 2.6 | 4.8 | 0.006 |
| DLR* | 120.5 | 80.8 | 52.9 | 0.2 | 7.3 | 10 | 11.4 | 0.023 |
| PAG* | −152.6 | −164.9 | −233.4 | 0.4 | 2.5 | 2.2 | 4.1 | 0.005 |
| MMB | −211.6 | 143.2 | 53.6 | 0.2 | 1.4 | 1.9 | 1.2 | 0.004 |
| KMH* | −32.1 | −52.2 | 177.6 | 0.3 | 6.4 | 4.2 | 6.9 | 0.023 |
| GLK* | −143.5 | −40.2 | −251.8 | 0.1 | 6.7 | 12.3 | 11.9 | 0.028 |
| AQU* | 9.9 | 39.4 | −11.6 | 0.1 | 3.8 | 7.1 | 9.3 | 0.017 |
| HBK* | 106.2 | −19.2 | 41.1 | 0.1 | 3.5 | 3 | 3.1 | 0.013 |
| DUR* | 49.8 | 56.2 | 25.7 | 0.1 | 4.6 | 8.9 | 10.5 | 0.02 |
| IZN* | 146.3 | −20.1 | 3.6 | 0.1 | 2.8 | 4.2 | 4.5 | 0.009 |
| BMT* | 323.1 | −615.2 | 151.5 | 1.2 | 2.8 | 4.7 | 5.8 | 0.009 |
| EBR | 1.7 | 6.3 | −4.2 | 0 | 2.9 | 5.5 | 7.7 | 0.012 |
| ASP | 47.2 | −19.6 | 35.3 | 0 | 2 | 2.4 | 2 | 0.005 |
| SPT | 11.7 | 9.6 | −26.6 | 0 | 1.5 | 1.4 | 1.5 | 0.003 |
| PEG* | −27.1 | 40.3 | −21.9 | 0.1 | 6.2 | 11.2 | 11.6 | 0.024 |
| LRM | −27.7 | −32 | 181.3 | 0.1 | 3.7 | 6.9 | 9.1 | 0.013 |
| TRW* | −6.2 | −28.7 | 113 | 0.1 | 6 | 10.4 | 11.3 | 0.033 |
| LZH* | 32 | 2.3 | −138.1 | 0 | 4.8 | 8.8 | 23.4 | 0.017 |
| TSU* | 48.5 | −57.5 | 80.3 | 0.2 | 5.8 | 9 | 10.8 | 0.036 |
| CYG | −51.7 | 51.8 | −99.8 | 0.1 | 4.9 | 9.5 | 10.8 | 0.018 |
| KAK | 10.9 | 14.2 | −96.1 | 0 | 1.1 | 2.1 | 1.2 | 0.004 |
| SFS | 4.6 | −8 | −59.2 | 0 | 2 | 2.8 | 2.2 | 0.006 |
| CTA | −438.2 | −84.1 | 184.9 | 0.1 | 2.4 | 3.1 | 4.7 | 0.006 |
| QSB* | 96.4 | −120.1 | −51.2 | 0.3 | 5 | 9.6 | 10.9 | 0.019 |
| TEO* | 7.5 | 42.4 | −112.7 | 0.1 | 8 | 12.9 | 12 | 0.027 |
| SHE* | 1018.9 | 540.1 | −1477.1 | 2.8 | 3.5 | 7.3 | 9.5 | 0.026 |
| TAN* | 288.3 | −58.7 | −190.6 | 0.1 | 5 | 8.5 | 10.4 | 0.022 |
| KNY | 5.7 | 53.4 | −48.5 | 0.1 | 1.1 | 1.6 | 1.6 | 0.003 |
| MID* | 859.9 | 223.2 | 1034.4 | 0.2 | 6.7 | 12 | 11.7 | 0.024 |
| SJG | −53.1 | 128.2 | 131.3 | 0.2 | 2.8 | 7.5 | 5.2 | 0.015 |
| VSS* | 68.3 | −54.7 | −33.4 | 0.1 | 4.2 | 6.2 | 8.4 | 0.02 |
| PIL* | 16.7 | −3 | −10.7 | 0 | 4.4 | 6.6 | 8.2 | 0.021 |
| KDU | 10.5 | −34.6 | 25.3 | 0.1 | 1.9 | 3.2 | 2.7 | 0.005 |
| CKI | −259.2 | −96.5 | −164.6 | 0.2 | 3.6 | 7 | 9.4 | 0.011 |
| HON | −164 | 88.3 | −326.4 | 0.2 | 1.5 | 2.2 | 1.7 | 0.005 |
| ASC | −499.6 | 269.4 | 11.4 | 0.4 | 3.3 | 6.7 | 9.5 | 0.019 |
| IPM* | 12 | 254.2 | −586.7 | 0.5 | 4.4 | 7.6 | 9.8 | 0.017 |
| GUI* | −3099.9 | −808.1 | −469.8 | 2.1 | 2.9 | 3.8 | 2.6 | 0.008 |

| IAGA code | $X_a$ (nT) | $Y_a$ (nT) | $Z_a$ (nT) | $D_a$ (°) | MSD($X_a$) (nT) | MSD($Y_a$) (nT) | MSD($Z_a$) (nT) | MSD($D_a$) (°) |
|---|---|---|---|---|---|---|---|---|
| LNP* | 44.5 | 47.8 | 37.8 | 0.1 | 6.1 | 11.2 | 11.5 | 0.018 |
| GZH* | 422.3 | 159.4 | −1504.6 | 0.3 | 6.3 | 11.4 | 11.7 | 0.017 |
| PPT | −890.6 | −1033.6 | −389 | 1.6 | 20.9 | 7.5 | 5.7 | 0.016 |
| API* | −8.1 | 233.4 | −866 | 0.4 | 5.9 | 8.7 | 9.5 | 0.015 |
| PHU* | 13.9 | 11.1 | −17.7 | 0 | 3.9 | 7.7 | 9.8 | 0.011 |
| ABG | −90.8 | 451.8 | 749.9 | 0.7 | 3.7 | 7.4 | 6.8 | 0.011 |
| TAM | 53.6 | −215.9 | −49.1 | 0.4 | 1.9 | 3 | 2.7 | 0.005 |
| HYB | 258.2 | 25.8 | 473.5 | 0 | 4.4 | 8.8 | 10.6 | 0.013 |
| CPL* | 64.3 | −48.7 | −158.5 | 0.1 | 6.9 | 12.2 | 11.7 | 0.018 |
| GAN* | −67.7 | 40.9 | 25.8 | 0.1 | 3.5 | 5.8 | 7.9 | 0.009 |
| BNG* | −80.3 | 12 | 342.8 | 0 | 4.7 | 9 | 11.1 | 0.016 |
| GUA | 123.7 | 78.4 | 49.3 | 0.1 | 2 | 2.9 | 1.9 | 0.005 |
| DLT | −51.2 | −42.3 | 89.5 | 0.1 | 7.4 | 10.2 | 10.5 | 0.014 |
| KOU | 110.8 | 98.2 | −39.2 | 0.3 | 2 | 2 | 3.6 | 0.004 |
| TTB* | 11.5 | −52.3 | 106.7 | 0.1 | 4.4 | 8.7 | 10.4 | 0.018 |
| MBO | 111.1 | 38 | 63.8 | 0.1 | 2.3 | 2.2 | 4.2 | 0.004 |
| AAE* | 724.3 | −107.6 | 534.6 | 0.2 | 9.9 | 4.6 | 5.6 | 0.007 |
| HUA* | 46.9 | 34.7 | −5.8 | 0.1 | 3.2 | 5.3 | 7.7 | 0.013 |

**Table A3.** Errors of the full model values of the EMF components (CHAOS + The1050) relative to observatory data.

| IAGA code | $\gamma(X)$ (%) | $X$ | $\gamma(Y)$ (%) | $Y$ | $\gamma(Z)$ (%) | $\Delta_D$ (°) |
|---|---|---|---|---|---|---|
| SIT | 0.4 | 14826.8 | 12.9 | 5535.6 | −1.7 | 2.41 |
| PAF | −4.5 | 10220.9 | −0.9 | −14775.3 | −0.6 | 1.22 |
| POD* | 0.1 | 11236.1 | 1.4 | 1694.9 | 0.1 | 0.12 |
| BRD* | 0.3 | 15098.8 | −2.9 | 1395.8 | 0.1 | 0.17 |
| KLI* | −0.4 | 13748.6 | 0.1 | 3765.6 | 0.2 | 0.06 |
| LER | 0.2 | 15013.6 | 7.1 | −613.6 | 0.2 | 0.24 |
| SPG* | −0.3 | 14450.8 | 0.1 | 2786.2 | 0.5 | 0.05 |
| NUR* | 0.3 | 14766.3 | 3.1 | 2252.2 | −0.4 | 1.09 |
| YAK* | −0.3 | 13467.6 | −17.1 | −4955.8 | 0.4 | 3.19 |
| UPS | 0.2 | 15153 | −0.6 | 1286.5 | 0 | 0.13 |
| LOV* | −0.5 | 15307.6 | −7.2 | 947.1 | −0.1 | 0.27 |
| BOX | 0 | 15295.2 | −1.8 | 3168 | 0.1 | 0.27 |
| MGD | 1 | 16772.1 | −17.3 | −4030.9 | 0 | 2.33 |
| NEW | −0.2 | 17464.6 | −0.9 | 4959.7 | 0.4 | 0.17 |
| OTT | −0.7 | 17492.2 | −4.4 | −4376.3 | −0.5 | 0.55 |
| ARS* | 1.1 | 15832.5 | 7.2 | 3609.5 | −0.2 | 0.83 |

| IAGA code | $\gamma(X)$ (%) | $X$ | $\gamma(Y)$ (%) | $Y$ | $\gamma(Z)$ (%) | $\Delta_D$ (°) |
|---|---|---|---|---|---|---|
| VIC | −0.3 | 18083.1 | −1.1 | 5576.9 | 0.5 | 0.2 |
| CZT | 6.7 | 10619.9 | 8.6 | −12235.4 | 0.2 | 3.08 |
| SHU | −2.2 | 19427.4 | 5.2 | 4155.6 | 0 | 0.74 |
| ESK | 0.1 | 17496 | 0.9 | −947.7 | 0 | 0.1 |
| NVS | −0.4 | 16283.3 | 0.6 | 2373.9 | 0 | 0.09 |
| MHV* | 3.5 | 16290.9 | −11.4 | 3907.4 | 0.3 | 1.54 |
| AIA* | −0.7 | 19692.4 | 1.5 | 5482.3 | 2 | 0.26 |
| HLP | −0.3 | 17519.6 | 6.1 | 1288 | 0.2 | 0.17 |
| STJ | −0.1 | 18863.8 | −0.3 | −6242.5 | 0.1 | 0.03 |
| EYR* | −0.2 | 19322.9 | 0.4 | 8349.1 | 0.1 | 0.04 |
| WNG | 0.1 | 18156.7 | −1 | 557 | 0 | 0.1 |
| ORC* | 0.2 | 17990.3 | −0.9 | 536.3 | −0.2 | 0.01 |
| AMS* | 2.4 | 13731.2 | −5 | −12036.6 | −3.5 | 1.6 |
| SBL | 0 | 19860.3 | 0.1 | −6283.4 | 0.1 | 0 |
| VAL | −0.1 | 19105.5 | 1.2 | −2387.4 | 0 | 0.1 |
| IRT* | −0.4 | 18418.4 | 0.7 | −1206.8 | 0.1 | 0.02 |
| BOU | 0.2 | 20593.8 | −2.6 | 3278.1 | 0.2 | 0.27 |
| NGK | 0 | 18854.3 | −0.7 | 904.4 | 0 | 0.1 |
| BEL | −0.2 | 18938.1 | 1.7 | 1761.3 | −0.2 | 0.02 |
| HAD | −0.1 | 19694.1 | 0.4 | −900.8 | 0.1 | 0.02 |
| FRD | 0 | 20936.7 | −0.6 | −3881.5 | −0.1 | 0.05 |
| PET | 0.8 | 21526.8 | 8.7 | −2312.4 | 0.8 | 0.47 |
| KEP | 0 | 15528.3 | −3.2 | −1961.6 | 0.3 | 0.22 |
| MAB* | −0.2 | 19882.5 | 27.2 | −65.2 | −0.4 | 0.06 |
| DOU | −0.3 | 20091.7 | 5.8 | 156.5 | 0 | 0.06 |
| CNB | −0.1 | 23170.2 | 0.3 | 5159.8 | 0 | 0.04 |
| BDV* | 0 | 20402.1 | −1.3 | 1314.6 | 0 | 0.05 |
| BFO* | 0 | 20975.3 | −0.2 | 799.1 | 0 | 0 |
| FUR* | 0 | 20943.1 | 0.8 | 826.9 | 0 | 0.06 |
| HRB | 0 | 20943 | −0.8 | 992.8 | 0.2 | 0.02 |
| WIC | −0.4 | 21007.2 | −0.9 | 1520.5 | 0 | 0.03 |
| CLF | 0.1 | 21128.9 | −6 | −213.3 | 0 | 0.05 |
| NCK* | 0 | 21051 | −2.6 | 890.9 | 0.2 | 0.06 |
| GNA | 0.1 | 23373.1 | 5.4 | −760.8 | −0.1 | 0.09 |
| HER | −0.3 | 9618.1 | 0.5 | −4523.7 | 0.1 | 0.07 |
| FRN | 0 | 22891.3 | −0.2 | 5481.5 | 0.1 | 0.01 |
| GNG | 0.1 | 24004.1 | −1.5 | −693.1 | 0 | 0.02 |
| THY | 0.1 | 21492.9 | −1.3 | 1388.2 | 0 | 0.11 |

| IAGA code | $\gamma(X)$ (%) | $X$ | $\gamma(Y)$ (%) | $Y$ | $\gamma(Z)$ (%) | $\Delta_D$ (°) |
|---|---|---|---|---|---|---|
| TDC* | 3.8 | 9609 | 12.8 | −3876.3 | −1.8 | 2.67 |
| KHB | 1.1 | 23308.4 | −8.2 | −5339.1 | −0.9 | 1.05 |
| LON* | −0.1 | 22372.7 | 0 | 1663.9 | 0 | 0.03 |
| PST | 0.1 | 18155.8 | 3.6 | 883.1 | 0.1 | 0.1 |
| BSL* | 0 | 23979.9 | −0.3 | −237.6 | −0.1 | 0.02 |
| SUA* | 0 | 22598.9 | 0.8 | 2113.3 | 0.1 | 0.03 |
| GCK* | 0.2 | 22674.6 | 2 | 1506.4 | 0.2 | 0.07 |
| AAA* | 0 | 24856.8 | −0.3 | 2115.8 | 0.5 | 0.03 |
| TUC | 0.2 | 24199.1 | 5.8 | 4158.2 | −0.8 | 0.57 |
| DLR* | 0 | 25127.3 | −1 | 3076 | 0 | 0.09 |
| PAG* | 0.7 | 23697.8 | 9.6 | 1716.6 | 0.6 | 0.36 |
| MMB | 0.8 | 25858.7 | −0.7 | −3991.6 | −0.4 | 0.13 |
| KMH* | 0.2 | 10621.6 | −2 | −3286 | 0.6 | 0.36 |
| GLK* | 0.8 | 24417.4 | 9.5 | 2809.3 | 0.8 | 0.62 |
| AQU* | 0 | 24087.3 | −1.3 | 913.1 | 0.1 | 0.02 |
| HBK* | −0.3 | 12343 | −1 | −3929.1 | −0.2 | 0.24 |
| DUR* | 0.1 | 24639.2 | −1.4 | 1555.5 | 0.1 | 0.05 |
| IZN* | −0.4 | 25073.1 | 1.7 | 2136.2 | 0 | 0.05 |
| BMT* | −1 | 28031 | −14.7 | −3871.1 | −0.4 | 1.18 |
| EBR | 0 | 25225.3 | 5.9 | 83.6 | 0 | 0 |
| ASP | 0 | 30022.7 | 0.2 | 2595.3 | 0 | 0.07 |
| SPT | 0 | 25916.5 | −0.4 | −750.1 | 0.1 | 0.04 |
| PEG* | 0.2 | 26411.2 | −1.9 | 1895.2 | 0.2 | 0.09 |
| LRM | 0 | 30217.1 | 15.5 | 149.6 | 0 | 0.03 |
| TRW* | 0.2 | 19238.1 | 4.4 | 1439.3 | 0.3 | 0.18 |
| LZH* | −0.1 | 30642.8 | −1.4 | −1210.7 | 0.1 | 0.05 |
| TSU* | 0.1 | 14048.8 | 0.4 | −2259.2 | 0 | 0.02 |
| CYG | 0.2 | 30065.8 | 1.1 | −4142.5 | 0.3 | 0.09 |
| KAK | −0.1 | 29745.7 | 0.4 | −3765.8 | 0.1 | 0.04 |
| SFS | 0 | 27431.6 | 0.7 | −979.5 | 0.2 | 0.07 |
| CTA | 1.2 | 31508.2 | 0.5 | 4204.2 | 0.4 | 0.11 |
| QSB* | −0.2 | 28828.3 | 7.3 | 1853.1 | 0.3 | 0.26 |
| TEO* | −0.2 | 27950.3 | 0.1 | 3116.8 | 0.3 | 0.02 |
| SHE* | −6.3 | 16139.7 | 12.6 | −4022.7 | −5.5 | 1.9 |
| TAN* | −1.4 | 19855.2 | −0.8 | −5235.1 | −0.7 | 0.21 |
| KNY | 0 | 32514 | 1 | −3548.7 | 0 | 0.01 |
| MID* | −3 | 27541 | −6.3 | 4157.3 | −4.1 | 0.59 |
| SJG | 0.6 | 26324.8 | −0.4 | −5849.9 | −0.5 | 0.11 |

| IAGA code | $\gamma(X)$ (%) | $X$ | $\gamma(Y)$ (%) | $Y$ | $\gamma(Z)$ (%) | $\Delta_D$ (°) |
|---|---|---|---|---|---|---|
| VSS* | 0 | 16765.6 | −0.6 | −6979.1 | −0.2 | 0.12 |
| PIL* | −0.1 | 18844.6 | −1.2 | −1763.3 | −0.3 | 0.04 |
| KDU | 0 | 35385.9 | 2.8 | 2110.5 | −0.1 | 0.16 |
| CKI | 0.5 | 34654 | −8.4 | −1343.6 | 0 | 0.2 |
| HON | 0.9 | 27080.6 | −2.2 | 4750.3 | 1.7 | 0.23 |
| ASC | 2 | 19894.2 | 7 | −5364 | −0.3 | 1.08 |
| IPM* | −1.2 | 25144.2 | −3 | 7122.7 | −2.4 | 0.48 |
| GUI* | 11.2 | 27417.1 | −20.1 | −3918.6 | 2.3 | 1.79 |
| LNP* | 0 | 36427.1 | 4.3 | −2097.4 | −0.1 | 0.14 |
| GZH* | −1.1 | 37871 | 14.5 | −1283 | 6.2 | 0.31 |
| PPT | 3.1 | 29302.7 | 17.6 | 5847.3 | −3.6 | 1.98 |
| API* | 0.5 | 32595.1 | −2.4 | 6901.8 | −4.1 | 0.29 |
| PHU* | 0 | 38958.3 | 0.7 | −806.9 | 0.1 | 0.02 |
| ABG | 0.2 | 38122.1 | −200.1 | 102.8 | −3.8 | 0.66 |
| TAM | −0.1 | 33636 | −35.5 | −96.4 | 0.2 | 0.2 |
| HYB | −0.5 | 39407.1 | 10.3 | −665.8 | −2.3 | 0.11 |
| CPL* | 0 | 39468.9 | 14.8 | −482.7 | 0.4 | 0.1 |
| GAN* | 0.4 | 37691 | 3.5 | −2822.1 | −0.2 | 0.13 |
| BNG* | −0.4 | 31960.5 | 18.2 | −517.5 | −0.2 | 0.16 |
| GUA | −0.3 | 35720.2 | −10.2 | 765 | −0.4 | 0.08 |
| DLT | 0.2 | 40787.7 | −6.5 | −464.2 | −0.7 | 0.05 |
| KOU | −0.3 | 26612.9 | 0.2 | −8576.5 | 0.1 | 0.08 |
| TTB* | −0.1 | 24738.5 | −0.6 | −9117.8 | 6 | 0.1 |
| MBO | −0.1 | 32015.9 | 1.5 | −4652.3 | −0.9 | 0.15 |
| AAE* | −2 | 36187.5 | 11.9 | 1047.4 | −32.6 | 0.22 |
| HUA* | −0.2 | 24745.8 | −0.2 | −1380.4 | −1.4 | 0.03 |

**Table A4.** Comparison of the obtained values with the results by Califf et al. (2022) (the values of the EMF components are given in geocentric spherical coordinates): $Br_{Cal}, B\theta_{Cal}, B\varphi_{Cal}$ are the values from the cited work; $|\Delta_{Br}|, |\Delta_{B\theta}|, |\Delta_{B\varphi}|$ are absolute differences between these values and the corrections we obtained (Table A2); err_Br, err_B$\theta$, err_B$\varphi$ are MSDs within which the absolute differences lie.

| IAGA code | $Br_{Cal}$ (nT) | $B\theta_{Cal}$ (nT) | $B\varphi_{Cal}$ (nT) | $\|\Delta_{Br}\|$ (nT) | $\|\Delta_{B\theta}\|$ (nT) | $\|\Delta_{B\varphi}\|$ (nT) | err_Br | err_B$\theta$ | err_B$\varphi$ |
|---|---|---|---|---|---|---|---|---|---|
| SIT | 85.6 | −27.2 | −16 | 5.6 | 7.2 | 1.3 | $2\sigma'$ | — | $1\sigma'$ |
| LER | −40.1 | 126.2 | 175.9 | 6 | 4.9 | 2.6 | $3\sigma'$ | $2\sigma'$ | $1\sigma'$ |
| UPS | 119.9 | −151.9 | −14.5 | 5.1 | 0.3 | 1.3 | $3\sigma'$ | $1\sigma'$ | $1\sigma'$ |
| BOX | 349.8 | −2.6 | 1.8 | 3.9 | 2.9 | 0.2 | $2\sigma'$ | $1\sigma'$ | $1\sigma'$ |
| MGD | −44.6 | 251.1 | −718.4 | 12 | 20 | 35.5 | $2\sigma'$ | — | — |
| NEW | 125.2 | 20.5 | 114.9 | 1.7 | 2.2 | 0.9 | $1\sigma'$ | $2\sigma'$ | $1\sigma'$ |

| IAGA code | $Br_{Cal}$ (nT) | $B\theta_{Cal}$ (nT) | $B\varphi_{Cal}$ (nT) | $\|\Delta_{Br}\|$ (nT) | $\|\Delta_{B\theta}\|$ (nT) | $\|\Delta_{B\varphi}\|$ (nT) | err_Br | err_$B\theta$ | err_$B\varphi$ |
|---|---|---|---|---|---|---|---|---|---|
| SHU | −29.5 | −415.9 | −234.4 | 0.4 | 1.4 | 0.9 | $1\sigma'$ | $1\sigma'$ | $1\sigma'$ |
| ESK | 60.1 | −20.2 | −34.6 | 1.3 | 0.2 | 2.8 | $1\sigma'$ | $1\sigma'$ | $2\sigma'$ |
| NVS | −18.7 | −77.6 | −55.1 | 1.7 | 2.6 | 1.3 | $1\sigma'$ | $2\sigma'$ | $1\sigma'$ |
| WNG | 73.4 | −68 | 49 | 9.8 | 10.9 | 2.2 | — | — | $2\sigma'$ |
| SBL | 88.6 | −11.5 | 9.3 | 4.8 | 0.3 | 3.1 | $1\sigma'$ | $1\sigma'$ | $1\sigma'$ |
| BOU | 139.2 | −0.9 | 37.6 | 2.7 | 4.7 | 0.2 | $2\sigma'$ | — | $1\sigma'$ |
| NGK | 78.1 | 12.3 | −0.8 | 3.8 | 4 | 2.6 | $3\sigma'$ | $2\sigma'$ | $2\sigma'$ |
| BEL | −311.7 | −127 | 135.3 | 2.1 | 3.8 | 1 | $2\sigma'$ | $2\sigma'$ | $1\sigma'$ |
| HAD | −67.5 | 31.7 | 14.6 | 2.6 | 1.5 | 0.5 | $1\sigma'$ | $1\sigma'$ | $1\sigma'$ |
| FRD | −110.6 | −83.2 | −44.4 | 11 | 5.4 | 0.9 | — | — | $1\sigma'$ |
| PET | −134.4 | 293.3 | 251.8 | 5.9 | 0.2 | 4.2 | $2\sigma'$ | $1\sigma'$ | $1\sigma'$ |
| KEP | −86.6 | 26.6 | −44.2 | 0.1 | 3.1 | 0.8 | $1\sigma'$ | $1\sigma'$ | $1\sigma'$ |
| DOU | −77.5 | −25.3 | −18 | 2 | 1.1 | 0 | $1\sigma'$ | $1\sigma'$ | $1\sigma'$ |
| CNB | −78.7 | −3.8 | 49 | 0.9 | 1.5 | 1 | $1\sigma'$ | $1\sigma'$ | $1\sigma'$ |
| WIC | 18.3 | −14.9 | −2.5 | 1.4 | 2.1 | 1 | $1\sigma'$ | $1\sigma'$ | $1\sigma'$ |
| CLF | −107 | 65.7 | −16 | 7.6 | 6.1 | 0.7 | — | — | $1\sigma'$ |
| HER | −26.3 | −29.5 | 7.3 | 0.2 | 1.1 | 0.8 | $1\sigma'$ | $1\sigma'$ | $1\sigma'$ |
| FRN | 235.7 | −5.4 | −16.9 | 10.9 | 4.7 | 0.3 | $3\sigma'$ | $2\sigma'$ | $1\sigma'$ |
| GNG | −164.8 | −0.9 | −38.5 | 8.7 | 4.6 | 0 | $2\sigma'$ | $2\sigma'$ | $1\sigma'$ |
| THY | 57.3 | 5.5 | −12.9 | 2.2 | 0.6 | 0.1 | $2\sigma'$ | $1\sigma'$ | $1\sigma'$ |
| KHB | −606.8 | 281 | −429.3 | 5.8 | 3.9 | 1.2 | $1\sigma'$ | $2\sigma'$ | $1\sigma'$ |
| PST | −32.3 | −36.1 | −11.5 | 3.2 | 0.8 | 1.4 | $1\sigma'$ | $1\sigma'$ | $1\sigma'$ |
| TUC | −419.5 | 82 | −265.2 | 11.1 | 1.9 | 0.3 | $3\sigma'$ | $2\sigma'$ | $1\sigma'$ |
| MMB | −47.1 | 207.2 | 144.4 | 5.8 | 4.5 | 1.2 | — | — | $1\sigma'$ |
| EBR | −4.9 | 1.5 | 5.4 | 9 | 3.2 | 0.9 | $2\sigma'$ | $2\sigma'$ | $1\sigma'$ |
| ASP | −40.6 | −53.2 | −19.2 | 5.4 | 5.9 | 0.4 | $3\sigma'$ | $3\sigma'$ | $1\sigma'$ |
| SPT | 26.9 | −13.7 | 9.1 | 0.4 | 1.9 | 0.5 | $1\sigma'$ | $2\sigma'$ | $1\sigma'$ |
| LRM | −173.7 | 28.8 | −33 | 7.7 | 1.5 | 1 | $1\sigma'$ | $1\sigma'$ | $1\sigma'$ |
| CYG | 97.2 | 50.1 | 52.7 | 2.7 | 1.2 | 0.9 | $1\sigma'$ | $1\sigma'$ | $1\sigma'$ |
| KAK | 98 | −14.3 | 14.4 | 2 | 3.1 | 0.2 | $2\sigma'$ | $3\sigma'$ | $1\sigma'$ |
| SFS | −153 | 93.4 | 31.9 | 212.2 | 98.2 | 39.9 | — | — | — |
| CTA | −176.1 | 437.6 | −83.9 | 9.7 | 0.2 | 0.2 | $3\sigma'$ | $1\sigma'$ | $1\sigma'$ |
| KNY | 39.4 | −4.4 | 52.4 | 9.1 | 1.5 | 1 | — | $2\sigma'$ | $1\sigma'$ |
| SJG | −127.2 | 51.6 | 131.3 | 4 | 1.8 | 3.1 | $1\sigma'$ | $1\sigma'$ | $1\sigma'$ |
| KDU | −20.8 | −11.3 | −33 | 4.5 | 0.8 | 1.6 | $2\sigma'$ | $1\sigma'$ | $1\sigma'$ |
| CKI | 169.6 | 259.2 | −97.2 | 5.4 | 0.2 | 0.7 | $1\sigma'$ | $1\sigma'$ | $1\sigma'$ |
| HON | 324.2 | 162 | 88.8 | 2.6 | 1.3 | 0.5 | $2\sigma'$ | $1\sigma'$ | $1\sigma'$ |
| ASC | −25.8 | 497.7 | 269.4 | 13.9 | 1.9 | 0 | $2\sigma'$ | $1\sigma'$ | $1\sigma'$ |

| IAGA code | $Br_{Cal}$ (nT) | $B\theta_{Cal}$ (nT) | $B\varphi_{Cal}$ (nT) | $\lvert\Delta_{Br}\rvert$ (nT) | $\lvert\Delta_{B\theta}\rvert$ (nT) | $\lvert\Delta_{B\varphi}\rvert$ (nT) | err_Br | err_B$\theta$ | err_B$\varphi$ |
|---|---|---|---|---|---|---|---|---|---|
| TAM | 59 | −56.5 | −218.8 | 10 | 2.8 | 2.9 | — | $2\sigma'$ | $1\sigma'$ |
| HYB | −468.3 | −270.5 | 26.8 | 5.7 | 13.3 | 1 | $1\sigma'$ | — | $1\sigma'$ |
| GUA | −54.2 | −126.1 | 78.9 | 4.7 | 2.5 | 0.5 | $3\sigma'$ | $2\sigma'$ | $1\sigma'$ |
| DLT | −137.6 | 56.5 | −44.8 | 48.2 | 5.2 | 2.5 | — | $1\sigma'$ | $1\sigma'$ |
| KOU | 39.7 | −112.6 | 99.8 | 0.5 | 1.8 | 1.6 | $1\sigma'$ | $1\sigma'$ | $1\sigma'$ |

**Table A5.** Comparison of the model values of the crustal field components according to The1050 with the values we obtained (Table A2).

| IAGA code | X_The1050 | | Y_The1050 | | Z_The1050 | |
|---|---|---|---|---|---|---|
| | Δ (nT) | $\delta$ (%) | Δ (nT) | $\delta$ (%) | Δ (nT) | $\delta$ (%) |
| SIT | 60 | 145.7 | 717.3 | 554.5 | −910.9 | 7694.8 |
| PAF | −456.1 | 223.1 | 136 | 103.1 | 267.4 | 648 |
| POD* | 12.9 | 7.2 | 22.8 | 1.7 | 72.5 | 225.1 |
| BRD* | 50.3 | 129.5 | −40.9 | 9.3 | 49.8 | 448.4 |
| KLI* | −53.9 | 42.8 | 2.3 | 0.5 | 87.7 | 267.3 |
| LER | 30.9 | 46.7 | −43 | 0.4 | 125.3 | 608.5 |
| SPG* | −45.6 | 62 | 1.9 | 0.6 | 234.5 | 1146.8 |
| NUR* | 42 | 58.4 | 66.1 | 16.6 | −174.5 | 852.4 |
| YAK* | −40.1 | 28.2 | 847.8 | 173.6 | 251.6 | 772.9 |
| UPS | 26.2 | 38.2 | −8.8 | 1.7 | 9.1 | 44.2 |
| LOV* | −71.5 | 106.2 | −68 | 13.1 | −52.4 | 254.7 |
| BOX | −6.8 | 6.1 | −56.7 | 11.9 | 52.6 | 159 |
| MGD | 166.5 | 157.9 | 699.7 | 139.1 | −18.4 | 55.4 |
| NEW | −31.4 | 96 | −43.1 | 32.8 | 184.1 | 1624.9 |
| OTT | −122.4 | 389.9 | 192.1 | 138.6 | −279.4 | 2455.1 |
| ARS* | 170.6 | 145.9 | 261.6 | 60.4 | −81.9 | 248.3 |
| VIC | −55.3 | 176.7 | −61.1 | 54.1 | 255 | 2235.6 |
| CZT | 710.6 | 507.7 | −1054.7 | 959.3 | −78.4 | 181.5 |
| SHU | −422.6 | 1375.1 | 215 | 126.3 | 27.4 | 223.9 |
| ESK | 10 | 17.8 | −9.3 | 0.2 | 0.5 | 2.2 |
| NVS | −67.4 | 55.8 | 14.6 | 1.7 | −10.6 | 32.4 |
| MHV* | 573.4 | 571.8 | −444.7 | 90.8 | 129.6 | 387.4 |
| AIA* | −134.9 | 179.8 | 83 | 31 | −649.4 | 1418.5 |
| HLP | −55.8 | 97 | 77.5 | 16 | 118.2 | 564.3 |
| STJ | −13.9 | 50.1 | 20.4 | 22 | 40.9 | 351.5 |
| EYR* | −35.5 | 30.5 | 35.1 | 13.7 | −54.3 | 130.8 |
| WNG | 17.7 | 32.6 | −6.2 | 0.8 | −6.4 | 30.5 |

| IAGA code | X_The1050 | | Y_The1050 | | Z_The1050 | |
|---|---|---|---|---|---|---|
| | Δ (nT) | δ (%) | Δ (nT) | δ (%) | Δ (nT) | δ (%) |
| ORC* | 28.8 | 41.6 | −3.5 | 0.1 | 56.2 | 120.7 |
| AMS* | 330.7 | 241.4 | 603.2 | 321.6 | 1697.1 | 4112.1 |
| SBL | 2.8 | 10.5 | −8 | 9 | 43.9 | 373 |
| VAL | −26.7 | 54.1 | −28.8 | 2.9 | 8.6 | 40.3 |
| IRT* | −71.9 | 68 | −8.8 | 0.7 | 59.8 | 180.1 |
| BOU | 35.9 | 134.6 | −85.8 | 44.1 | 97.8 | 838.7 |
| NGK | −2.5 | 4.9 | −7.5 | 1.2 | 18.5 | 86.9 |
| BEL | −41.7 | 78.9 | 29.3 | 6.5 | −78.8 | 371.5 |
| HAD | −26.8 | 55.5 | −3.9 | 0.1 | 25.1 | 116.3 |
| FRD | −5.7 | 22.6 | 23.9 | 17.6 | −41.1 | 347 |
| PET | 172.9 | 227.8 | −206 | 35.6 | 392.6 | 1124.5 |
| KEP | −0.1 | 0.2 | 64.6 | 10.8 | −58.9 | 126.9 |
| MAB* | −41.7 | 86.6 | −17.2 | 1.7 | −161.1 | 747.3 |
| DOU | −63.3 | 132.8 | 20.3 | 1.8 | 12.2 | 56.5 |
| CNB | −29.4 | 37.3 | 17.9 | 5.1 | −22 | 64.1 |
| BDV* | −3.8 | 8.1 | −17.5 | 3.1 | 19.1 | 88.3 |
| BFO* | 3.7 | 8.1 | −1.7 | 0.2 | −4.5 | 20.7 |
| FUR* | 6.9 | 15 | 6.3 | 1 | −16.5 | 75.4 |
| HRB | −9.9 | 21.4 | −7.7 | 1.6 | 73.4 | 337 |
| WIC | −86.9 | 189.6 | −13.3 | 2.6 | 15.2 | 69.6 |
| CLF | 27.8 | 62.7 | 31.8 | 2.2 | −13.8 | 63.1 |
| NCK* | 3.6 | 7.9 | −23.3 | 4.7 | 66.7 | 305.4 |
| GNA | 17 | 22.3 | −41 | 1.4 | 41.8 | 121.6 |
| HER | −26.7 | 19.8 | −23.3 | 8.9 | −29.4 | 51.4 |
| FRN | −1.3 | 6 | −10.8 | 10.5 | 53 | 434.6 |
| GNG | 13.7 | 18.3 | 10.3 | 0.3 | 24.6 | 71.3 |
| THY | 26.3 | 58.9 | −17.9 | 3.7 | 19.1 | 87.2 |
| TDC* | 366.2 | 374.1 | −494.2 | 203.2 | 409.8 | 958.9 |
| KHB | 259.7 | 355.2 | 439.5 | 128.4 | −448.7 | 1270.6 |
| LON* | −13.2 | 31.1 | −0.2 | 0 | −23.2 | 104.2 |
| PST | 18.5 | 30.3 | 32.2 | 2.1 | −13.5 | 27 |
| BSL* | 0.5 | 2.4 | 0.3 | 0 | −27.2 | 218.5 |
| SUA* | 6.9 | 16.2 | 16.6 | 4.3 | 35.5 | 159.9 |
| GCK* | 44 | 105.1 | 29.9 | 6.9 | 89.6 | 401.9 |
| AAA* | 2.1 | 2.9 | −6.9 | 0.9 | 246.3 | 699.3 |
| TUC | 60.2 | 290.6 | 239.9 | 186.4 | −321.5 | 2571.3 |
| DLR* | −2.8 | 14.2 | −31 | 13.2 | 3 | 24 |

| IAGA code | X_The1050 | | Y_The1050 | | Z_The1050 | |
|---|---|---|---|---|---|---|
| | Δ (nT) | δ (%) | Δ (nT) | δ (%) | Δ (nT) | δ (%) |
| PAG* | 167.6 | 423.8 | 164.4 | 41.3 | 238.6 | 1050.9 |
| MMB | 198.2 | 423.5 | 26.3 | 9.4 | −161.7 | 564.8 |
| KMH* | 25.4 | 19.8 | 65.1 | 16.1 | −147.9 | 259.5 |
| GLK* | 188.7 | 121.1 | 267.2 | 20.2 | 319.7 | 360.2 |
| AQU* | −6.6 | 17.4 | −12.7 | 2.4 | 29.2 | 127.2 |
| HBK* | −36.1 | 31 | 38 | 11.7 | 43.1 | 73.6 |
| DUR* | 13.6 | 36.5 | −21.1 | 4.1 | 27.2 | 117.6 |
| IZN* | −113.1 | 299.4 | 37.8 | 10.4 | −13.8 | 59.6 |
| BMT* | −293.5 | 202.4 | 570 | 51.9 | −180.6 | 215.8 |
| EBR | 0.5 | 1.4 | 14.6 | 1 | −8.4 | 35.6 |
| ASP | −11.1 | 20.1 | 5.8 | 0.8 | 12.3 | 32.3 |
| SPT | −8.6 | 25.6 | 2.7 | 0 | 22.8 | 93.6 |
| PEG* | 42.8 | 124.3 | −35.4 | 9.1 | 56.8 | 236.6 |
| LRM | −1.2 | 2.3 | 23.5 | 0.2 | −11 | 28.7 |
| TRW* | 35.9 | 35.9 | 64 | 2.2 | −51 | 50.1 |
| LZH* | −33.8 | 26.1 | 14.2 | 0.6 | 64.4 | 73.7 |
| TSU* | 16.9 | 15.8 | −9.6 | 1.4 | −13.4 | 22.6 |
| CYG | 71.4 | 58.5 | −45.2 | 5.6 | 131.2 | 145.2 |
| KAK | −28.5 | 74.3 | −14.4 | 5.2 | 26.3 | 83 |
| SFS | 2.5 | 8.1 | −7.6 | 0.1 | 63.5 | 247.7 |
| CTA | 385 | 788.4 | 20.5 | 5.4 | −156.2 | 380.1 |
| QSB* | −59 | 47.9 | 134.3 | 9.9 | 92.1 | 93.2 |
| TEO* | −64.6 | 409.6 | 3.8 | 1.7 | 94.8 | 654.1 |
| SHE* | −1019.4 | 1355.9 | −507.7 | 181.2 | 1412.6 | 3092.3 |
| TAN* | −267.7 | 411.1 | 41.1 | 18.1 | 197.1 | 400.9 |
| KNY | −1.3 | 3.8 | −37.8 | 13.8 | 7 | 20.6 |
| MID* | −819.9 | 1562.7 | −261.4 | 62.4 | −1051.3 | 1820.4 |
| SJG | 160.8 | 303.8 | 23.6 | 10.8 | −120.3 | 205.1 |
| VSS* | 3.7 | 3.6 | 40.4 | 16.5 | 34.8 | 32.5 |
| PIL* | −25.2 | 28.5 | 20.6 | 2.8 | 35.8 | 29.3 |
| KDU | 0.4 | 1 | 56.5 | 6.2 | 21.2 | 43.2 |
| CKI | 175.8 | 337.3 | 112.1 | 6.1 | −11.1 | 19.3 |
| HON | 233.8 | 468.4 | −104.1 | 34.3 | 353.3 | 566 |
| ASC | 387.6 | 694.2 | −374.2 | 164.7 | 61 | 110.6 |
| IPM* | −290.5 | 588.5 | −215 | 116.4 | 460.6 | 697.4 |
| GUI* | 3076.3 | 12575 | 789 | 217.3 | 528 | 1590.2 |
| LNP* | 0.8 | 0.9 | −89.8 | 8.5 | −33 | 27.8 |

| IAGA code | X_The1050 | | Y_The1050 | | Z_The1050 | |
|---|---|---|---|---|---|---|
| | Δ (nT) | δ (%) | Δ (nT) | δ (%) | Δ (nT) | δ (%) |
| GZH* | −429.5 | 473.6 | −185.6 | 11.6 | 1538.7 | 1279.4 |
| PPT | 910.6 | 1971 | 1031.4 | 516.3 | 694.3 | 919.2 |
| API* | 163.4 | 358.7 | −167.4 | 78 | 820.7 | 1056 |
| PHU* | −18.7 | 22 | −5.8 | 0.2 | 21.2 | 15.4 |
| ABG | 79.2 | 118.5 | −440.5 | 1.4 | −750.6 | 581.4 |
| TAM | −46.1 | 51.5 | 137.5 | 3.6 | 42.2 | 24.1 |
| HYB | −190.3 | 291.5 | −68 | 1 | −396.7 | 278.6 |
| CPL* | −9.6 | 14.8 | −72.3 | 1.1 | 76.8 | 53.4 |
| GAN* | 147.2 | 360.2 | −99.5 | 16.7 | 25.3 | 20.7 |
| BNG* | −130.4 | 323.5 | −93.8 | 6.5 | 16.8 | 12.2 |
| GUA | −105.3 | 266.5 | −77.9 | 1.3 | −28.4 | 15.2 |
| DLT | 68.8 | 92.8 | 29.7 | 0.6 | −58.1 | 17.3 |
| KOU | −72 | 173.2 | −18.8 | 15 | 8.1 | 4.1 |
| TTB* | −24.5 | 59.1 | 50.8 | 45.1 | −85.3 | 21.7 |
| MBO | −30.6 | 78.2 | −69.2 | 18.5 | −43 | 11.4 |
| AAE* | −729 | 1880.7 | 123.5 | 12.4 | −531.3 | 79.2 |
| HUA* | −37.5 | 96.6 | 2.3 | 0.5 | 4.1 | 0.3 |

**Table A6.** Comparison of the model values of the crustal field components according to WDMAM with the values we obtained (Table A2).

| IAGA code | X_WDMAM | | Y_WDMAM | | Z_WDMAM | |
|---|---|---|---|---|---|---|
| | Δ (nT) | δ (%) | Δ (nT) | δ (%) | Δ (nT) | δ (%) |
| SIT | −35.4 | 85.9 | 217.5 | 168.2 | −358.4 | 3027.3 |
| PAF | −455.7 | 222.9 | 146.8 | 111.4 | 290.5 | 704.1 |
| POD* | −14.8 | 8.3 | 25.9 | 1.9 | −42.3 | 131.5 |
| BRD* | 64.2 | 165.3 | −8.5 | 1.9 | 44.1 | 397.6 |
| KLI* | −45.5 | 36.1 | 56.9 | 12.3 | 41.8 | 127.5 |
| LER | 65.1 | 98.3 | −123.6 | 1.1 | 189.6 | 920.3 |
| SPG* | −110.4 | 150.2 | −3.2 | 0.9 | 165.8 | 810.8 |
| NUR* | 48.6 | 67.7 | 22.4 | 5.6 | −200.4 | 978.6 |
| YAK* | 72.5 | 50.9 | 616.6 | 126.2 | 409.4 | 1257.6 |
| UPS | 29.3 | 42.7 | −20.3 | 3.8 | 44 | 214 |
| LOV* | −75.8 | 112.7 | −37 | 7.2 | 2.2 | 10.9 |
| BOX | −10.1 | 9 | −66.7 | 14 | 12.2 | 36.8 |
| MGD | 134.7 | 127.7 | 689.7 | 137.1 | 40.1 | 120.5 |
| NEW | −13.4 | 41.1 | −39.4 | 30 | 213.9 | 1887.9 |

| IAGA code | X_WDMAM | | Y_WDMAM | | Z_WDMAM | |
|---|---|---|---|---|---|---|
| | Δ (nT) | δ (%) | Δ (nT) | δ (%) | Δ (nT) | δ (%) |
| OTT | −91.8 | 292.4 | 164.5 | 118.7 | −278.4 | 2446.2 |
| ARS* | 75.2 | 64.3 | −247.9 | 57.2 | 30.6 | 92.7 |
| VIC | −70.1 | 224.3 | −96 | 84.9 | 238.5 | 2091.5 |
| CZT | 795.3 | 568.2 | −1041.5 | 947.3 | −138 | 319.1 |
| SHU | −414.2 | 1347.9 | 225.9 | 132.6 | 96 | 785 |
| ESK | 49.8 | 89.3 | −24.5 | 0.5 | 37.7 | 179.5 |
| NVS | −58.4 | 48.3 | −25.3 | 3 | −4.5 | 13.7 |
| MHV* | 572.3 | 570.7 | −626.1 | 127.8 | 105.6 | 315.7 |
| AIA* | −111.9 | 149.2 | 173.5 | 64.9 | −697.8 | 1524.1 |
| HLP | −78 | 135.6 | 109 | 22.5 | 116.2 | 554.9 |
| STJ | 12.6 | 45.2 | 10.9 | 11.7 | 91.4 | 784.8 |
| EYR* | −45.6 | 39.2 | 24.8 | 9.7 | −51.2 | 123.3 |
| WNG | 25.3 | 46.5 | −12 | 1.5 | 7.7 | 36.7 |
| ORC* | −1 | 1.5 | −24.5 | 1 | 44.5 | 95.5 |
| AMS* | 565.6 | 412.9 | 563.6 | 300.5 | 1805.7 | 4375.3 |
| SBL | 17 | 64.7 | −5.5 | 6.1 | 4.8 | 41.2 |
| VAL | −48.1 | 97.2 | −30.8 | 3.1 | −2.3 | 10.6 |
| IRT* | −37.6 | 35.6 | 27.6 | 2.2 | 14.9 | 44.8 |
| BOU | 41.8 | 156.5 | −127.6 | 65.6 | 16.2 | 139.2 |
| NGK | −12 | 23 | −7.5 | 1.2 | 27.5 | 129.2 |
| BEL | −15.8 | 29.9 | 55.8 | 12.5 | −51.3 | 241.8 |
| HAD | −53.6 | 111.3 | −5.2 | 0.1 | 24.4 | 113.5 |
| FRD | −14 | 55.7 | 45.1 | 33.2 | −106.1 | 896.9 |
| PET | 142.4 | 187.6 | −209.6 | 36.2 | 520.7 | 1491.7 |
| KEP | 39.6 | 56.4 | 64.6 | 10.8 | −27.2 | 58.7 |
| MAB* | −37.5 | 77.9 | −28.8 | 2.9 | −171.5 | 795.6 |
| DOU | −75.8 | 159.1 | 4.3 | 0.4 | 6.6 | 30.5 |
| CNB | −35.9 | 45.5 | −30.7 | 8.8 | −20.2 | 59 |
| BDV* | −13.4 | 28.2 | −37.2 | 6.6 | −20.2 | 93.3 |
| BFO* | 18.4 | 40.6 | 4.9 | 0.6 | −22.7 | 104.2 |
| FUR* | 4.7 | 10.3 | 9.8 | 1.5 | 3.9 | 18 |
| HRB | −20.4 | 44.2 | −17.6 | 3.7 | 36 | 165.2 |
| WIC | −77.2 | 168.5 | −16.3 | 3.1 | 33.6 | 154.3 |
| CLF | 20.5 | 46.2 | 43.2 | 3.1 | −20.6 | 93.9 |
| NCK* | 6.1 | 13.4 | −29.3 | 5.8 | 67.9 | 311 |
| GNA | 40 | 52.5 | −65.6 | 2.2 | 49.5 | 144 |
| HER | −13.6 | 10.1 | −3.4 | 1.3 | −17.1 | 29.9 |

| IAGA code | X_WDMAM | | Y_WDMAM | | Z_WDMAM | |
|---|---|---|---|---|---|---|
| | Δ (nT) | δ (%) | Δ (nT) | δ (%) | Δ (nT) | δ (%) |
| FRN | −34.1 | 150.8 | 51.2 | 49.7 | 93.1 | 764.2 |
| GNG | 11.2 | 14.9 | 6.6 | 0.2 | 53.4 | 154.7 |
| THY | 12.7 | 28.6 | −19.9 | 4.2 | 29.2 | 133.3 |
| TDC* | 373.7 | 381.8 | −477.1 | 196.2 | 406.4 | 950.9 |
| KHB | 273.9 | 374.6 | 402.6 | 117.6 | −490.8 | 1389.8 |
| LON* | −6.1 | 14.4 | −13.2 | 2.7 | −27 | 121.6 |
| PST | 21.1 | 34.5 | 12.2 | 0.8 | 7.2 | 14.3 |
| BSL* | 0.3 | 1.5 | −3.3 | 0.5 | −10.2 | 81.8 |
| SUA* | 0.2 | 0.5 | −4.5 | 1.2 | 6.8 | 30.7 |
| GCK* | 54.6 | 130.5 | 20.4 | 4.7 | 79.7 | 357.5 |
| AAA* | −13.2 | 18.2 | −13.5 | 1.7 | 272.9 | 775 |
| TUC | 46.4 | 224 | 211 | 163.9 | −349 | 2790.8 |
| DLR* | −15.1 | 75.6 | −39.6 | 16.9 | 6.2 | 48.7 |
| PAG* | 162.9 | 411.8 | 163.2 | 41 | 213.1 | 938.4 |
| MMB | 216 | 461.5 | 74.8 | 26.9 | −182.2 | 636 |
| KMH* | 28.3 | 22 | 62.5 | 15.5 | −130.1 | 228.3 |
| GLK* | 125.1 | 80.2 | 227.2 | 17.2 | 359.8 | 405.4 |
| AQU* | −17.7 | 46.3 | 2.4 | 0.5 | 33.4 | 145.3 |
| HBK* | −38 | 32.6 | 12.2 | 3.7 | 89.8 | 153.4 |
| DUR* | 19 | 50.7 | −23 | 4.5 | 43.1 | 186.2 |
| IZN* | −121.8 | 322.5 | 48.4 | 13.4 | −18.5 | 79.9 |
| BMT* | −322.7 | 222.6 | 592.5 | 54 | −159.8 | 190.9 |
| EBR | −4.1 | 11.7 | 15.3 | 1.1 | −6.8 | 28.8 |
| ASP | −75 | 135.6 | −19.7 | 2.8 | 8.7 | 22.8 |
| SPT | −2.4 | 7.2 | −8.8 | 0.1 | 29 | 119.3 |
| PEG* | 47.2 | 137 | −43.4 | 11.2 | 56.7 | 236.4 |
| LRM | −18.2 | 33.5 | 31.9 | 0.3 | 12.8 | 33.5 |
| TRW* | 50 | 50 | 67.6 | 2.4 | −67 | 65.8 |
| LZH* | −34.7 | 26.8 | 11.5 | 0.4 | 69.5 | 79.6 |
| TSU* | 12.7 | 11.9 | 8 | 1.2 | −26.4 | 44.5 |
| CYG | 56.5 | 46.3 | −46.2 | 5.7 | 73.5 | 81.3 |
| KAK | −31.7 | 82.9 | −49.3 | 18 | −13.7 | 43.2 |
| SFS | −10 | 32.6 | −17.7 | 0.2 | 51.8 | 201.9 |
| CTA | 354.7 | 726.4 | 19.2 | 5 | −123.1 | 299.5 |
| QSB* | −44.3 | 36 | 139.7 | 10.3 | 46.9 | 47.5 |
| TEO* | −75.2 | 476.5 | 2.4 | 1.1 | 96.7 | 666.6 |
| SHE* | −993.4 | 1321.3 | −517.2 | 184.6 | 1401.5 | 3067.9 |

| IAGA code | X_WDMAM | | Y_WDMAM | | Z_WDMAM | |
|---|---|---|---|---|---|---|
| | Δ (nT) | δ (%) | Δ (nT) | δ (%) | Δ (nT) | δ (%) |
| TAN* | −265.5 | 407.7 | 38.1 | 16.8 | 200.1 | 406.8 |
| KNY | 2 | 5.8 | −58.6 | 21.4 | −3.1 | 9 |
| MID* | −810.8 | 1545.4 | −218.3 | 52.1 | −1055.4 | 1827.6 |
| SJG | 182.3 | 344.5 | −71.4 | 32.6 | −38.2 | 65.1 |
| VSS* | −15.3 | 14.7 | 49.4 | 20.1 | 36.9 | 34.5 |
| PIL* | −31.6 | 35.7 | 21.8 | 3 | 59.2 | 48.4 |
| KDU | 11.8 | 28.9 | 49.9 | 5.5 | 32.9 | 67.1 |
| CKI | 221.3 | 424.5 | 100.8 | 5.5 | 78.2 | 135.6 |
| HON | 158.3 | 317 | 12.3 | 4.1 | 409.8 | 656.6 |
| ASC | 553.9 | 992.1 | −351.9 | 154.9 | −6.8 | 12.3 |
| IPM* | −294.8 | 597.1 | −301.6 | 163.2 | 404.9 | 613.1 |
| GUI* | 3089.4 | 12628.5 | 728.6 | 200.7 | 640.8 | 1929.7 |
| LNP* | −1.5 | 1.6 | −45 | 4.2 | −62.4 | 52.6 |
| GZH* | −418.2 | 461.1 | −149 | 9.3 | 1425.7 | 1185.5 |
| PPT | 850.3 | 1840.5 | 1129.9 | 565.6 | 673.4 | 891.6 |
| API* | 140.8 | 309 | −174.4 | 81.3 | 671.4 | 864 |
| PHU* | −16.3 | 19.2 | −4.4 | 0.2 | 48.3 | 35.2 |
| ABG | 74.8 | 111.9 | −443.4 | 1.4 | −739.5 | 572.8 |
| TAM | −40.1 | 44.8 | 143.3 | 3.7 | 41.1 | 23.4 |
| HYB | −197.5 | 302.7 | −69.9 | 1 | −406.7 | 285.6 |
| CPL* | −14.8 | 22.7 | −40.1 | 0.6 | 76 | 52.8 |
| GAN* | 118.6 | 290.2 | −153.3 | 25.7 | −32.5 | 26.6 |
| BNG* | −132.5 | 328.7 | −133.4 | 9.2 | 63.9 | 46.3 |
| GUA | −147.1 | 372.2 | −67.6 | 1.1 | −63 | 33.8 |
| DLT | 73.6 | 99.3 | 51.7 | 1.1 | −36 | 10.7 |
| KOU | −78.5 | 189 | −29.4 | 23.5 | 0.6 | 0.3 |
| TTB* | 15.5 | 37.3 | 51.2 | 45.5 | −53.4 | 13.6 |
| MBO | −40.3 | 103 | −60.9 | 16.3 | −35.1 | 9.3 |
| AAE* | −732.2 | 1889 | 129.8 | 13 | −519.4 | 77.5 |
| HUA* | −41.9 | 107.9 | 5.7 | 1.2 | −21.2 | 1.6 |

**Table A7.** Comparison of the model values of the crustal field components according to xDLFI with the values we obtained (Table A2).

| IAGA code | X_xDLFI | | Y_xDLFI | | Z_xDLFI | |
|---|---|---|---|---|---|---|
| | Δ (nT) | δ (%) | Δ (nT) | δ (%) | Δ (nT) | δ (%) |
| SIT | 271.1 | 658.4 | −101.4 | 78.4 | −35.7 | 301.7 |
| PAF | −449.1 | 219.7 | 170.6 | 129.4 | 338.7 | 821 |
| POD* | −119.5 | 67.1 | −124.9 | 9.2 | 125.9 | 391.1 |
| BRD* | −287 | 738.7 | −44.8 | 10.2 | −33.5 | 301.9 |
| KLI* | −24.4 | 19.4 | −186 | 40.3 | 13.2 | 40.4 |
| LER | 39.6 | 59.9 | −155.4 | 1.4 | −106.3 | 516 |
| SPG* | −95.9 | 130.4 | −75.4 | 21.8 | 284.6 | 1391.8 |
| NUR* | −259.5 | 361 | 42.5 | 10.7 | 87.4 | 427 |
| YAK* | −45.7 | 32.1 | 1068.1 | 218.7 | 522.4 | 1604.9 |
| UPS | −60.4 | 88.2 | 17.2 | 3.2 | 323.6 | 1575.2 |
| LOV* | −87.8 | 130.5 | −3.2 | 0.6 | −107.2 | 520.9 |
| BOX | 46.3 | 41.2 | −36.4 | 7.6 | 232.7 | 703.4 |
| MGD | 311.8 | 295.6 | 730.9 | 145.3 | 4.2 | 12.5 |
| NEW | 60.2 | 184.5 | −90.2 | 68.7 | 141.9 | 1252.5 |
| OTT | −214.2 | 682.1 | 115.2 | 83.2 | −36.1 | 317.5 |
| ARS* | −210.2 | 179.7 | 165.2 | 38.1 | −304.3 | 922.3 |
| VIC | −69.9 | 223.6 | 35.7 | 31.6 | 420.7 | 3688.7 |
| CZT | 724.5 | 517.6 | −971.6 | 883.7 | −493.7 | 1142 |
| SHU | 22.6 | 73.4 | 788.1 | 462.9 | −30.3 | 248.2 |
| ESK | 3.4 | 6.2 | 1.7 | 0 | 113.6 | 540.6 |
| NVS | 14.7 | 12.2 | −28.6 | 3.4 | −105.8 | 322.3 |
| MHV* | 368.4 | 367.4 | −485.3 | 99.1 | 187 | 559.1 |
| AIA* | −121.2 | 161.6 | 186.3 | 69.6 | −520.7 | 1137.3 |
| HLP | −90.1 | 156.6 | 339.2 | 69.9 | 207 | 988.4 |
| STJ | −65.1 | 234 | 81.4 | 87.7 | 34.2 | 294.1 |
| EYR* | 26.4 | 22.7 | 62.2 | 24.4 | −163.8 | 394.3 |
| WNG | −11.2 | 20.7 | −12.2 | 1.5 | 60.1 | 284.8 |
| ORC* | −55.8 | 80.4 | −36.4 | 1.5 | 88.9 | 190.8 |
| AMS* | 707.6 | 516.6 | 474.7 | 253.1 | 2389 | 5788.7 |
| SBL | 43.4 | 165.5 | −103 | 115.4 | 69.6 | 590.7 |
| VAL | −53.9 | 109.1 | −34.1 | 3.4 | 80.2 | 374.3 |
| IRT* | −42 | 39.7 | −106 | 8.4 | −13.2 | 39.8 |
| BOU | −7.5 | 28 | −113.2 | 58.2 | 137.6 | 1180.7 |
| NGK | 35.2 | 67.7 | −105.9 | 16.8 | −47 | 221.2 |
| BEL | 31.8 | 60.1 | −11.4 | 2.5 | −350.5 | 1652.1 |

| IAGA code | X_xDLFI | | Y_xDLFI | | Z_xDLFI | |
|---|---|---|---|---|---|---|
| | Δ (nT) | δ (%) | Δ (nT) | δ (%) | Δ (nT) | δ (%) |
| HAD | −37.2 | 77.1 | 0.4 | 0 | −76.3 | 354.1 |
| FRD | −113.8 | 453.6 | 14 | 10.3 | −44.4 | 374.9 |
| PET | 237.1 | 312.4 | −374.7 | 64.8 | 243.4 | 697.4 |
| KEP | 7.3 | 10.4 | 99.7 | 16.6 | −113.5 | 244.3 |
| MAB* | 39 | 81.2 | −1.6 | 0.2 | −157 | 728.3 |
| DOU | −30.8 | 64.7 | 25.8 | 2.3 | −80.1 | 370.8 |
| CNB | −22.8 | 28.9 | −24.8 | 7.1 | −17.8 | 51.8 |
| BDV* | −22.7 | 48 | −53.6 | 9.5 | 24.6 | 113.8 |
| BFO* | −40 | 87.9 | −14.3 | 1.9 | 12.2 | 55.7 |
| FUR* | 32.2 | 70.6 | 23.4 | 3.7 | −21.5 | 98.4 |
| HRB | −67.6 | 146.6 | 13.3 | 2.8 | 64.1 | 294.3 |
| WIC | −18.5 | 40.3 | −63.2 | 12.2 | −0.8 | 3.6 |
| CLF | 78 | 176.2 | 10.3 | 0.7 | −67.6 | 308 |
| NCK* | −69.8 | 153.4 | −43.8 | 8.7 | 104.7 | 479.7 |
| GNA | 44.6 | 58.6 | 55.8 | 1.9 | 61.6 | 179.3 |
| HER | −22.6 | 16.7 | −19.4 | 7.4 | −34.6 | 60.5 |
| FRN | 75.5 | 334.1 | 65 | 63.1 | 146.9 | 1205.6 |
| GNG | 15.7 | 21 | 28.2 | 0.9 | −55.5 | 160.9 |
| THY | 12.9 | 28.8 | −16.4 | 3.4 | 75.3 | 343.3 |
| TDC* | 390.2 | 398.5 | −479.8 | 197.3 | 443.2 | 1037.2 |
| KHB | 221.4 | 302.7 | 429.1 | 125.3 | −710.4 | 2011.5 |
| LON* | −15.4 | 36.3 | −52.5 | 10.7 | 70 | 315.2 |
| PST | 63.9 | 104.7 | −8.9 | 0.6 | −125.5 | 250.9 |
| BSL* | −3.4 | 16.2 | −4 | 0.6 | −41.4 | 332.9 |
| SUA* | −43 | 100.9 | 30.7 | 8 | 25.2 | 113.7 |
| GCK* | 42.6 | 101.7 | 43.4 | 10 | 86.3 | 386.9 |
| AAA* | −142.2 | 195.7 | 35.7 | 4.4 | 223.8 | 635.5 |
| TUC | 139.9 | 675.8 | 207.8 | 161.5 | −374.2 | 2992.3 |
| DLR* | −34.2 | 171.1 | −37.1 | 15.8 | −12.3 | 97.4 |
| PAG* | 117.2 | 296.3 | 132.5 | 33.3 | 160.5 | 706.9 |
| MMB | 269.4 | 575.8 | −48 | 17.2 | −223.5 | 780.5 |
| KMH* | 64.5 | 50.1 | 17.1 | 4.2 | −171.1 | 300.2 |
| GLK* | 156.3 | 100.3 | 139.5 | 10.6 | 210.9 | 237.6 |
| AQU* | 2.2 | 5.8 | −34.6 | 6.5 | 28.7 | 125 |
| HBK* | −41.6 | 35.7 | −4.8 | 1.5 | −116.8 | 199.4 |
| DUR* | −12.1 | 32.3 | −32.7 | 6.4 | −62.7 | 271.1 |
| IZN* | −127.1 | 336.5 | 17.5 | 4.8 | −29.7 | 128.5 |

| IAGA code | X_xDLFI | | Y_xDLFI | | Z_xDLFI | |
|---|---|---|---|---|---|---|
| | Δ (nT) | δ (%) | Δ (nT) | δ (%) | Δ (nT) | δ (%) |
| BMT* | −351.3 | 242.3 | 587.1 | 53.5 | −170.9 | 204.2 |
| EBR | 3 | 8.5 | −14.5 | 1 | −19.4 | 82 |
| ASP | −11 | 19.8 | 52.5 | 7.3 | −96.9 | 254.5 |
| SPT | −9.7 | 29 | −5.9 | 0.1 | 0.4 | 1.5 |
| PEG* | 60.8 | 176.5 | −9.7 | 2.5 | −47.1 | 196.1 |
| LRM | −109 | 200.8 | −11.1 | 0.1 | −73.2 | 190.8 |
| TRW* | 24.7 | 24.7 | 145.3 | 5.1 | −17.4 | 17.1 |
| LZH* | −133.8 | 103.5 | 49.3 | 1.9 | 36.6 | 41.9 |
| TSU* | −16.3 | 15.3 | 91 | 13.1 | −2.6 | 4.4 |
| CYG | 52.6 | 43.1 | −42 | 5.2 | 156.7 | 173.4 |
| KAK | −9.8 | 25.5 | −84.4 | 30.8 | 122.6 | 386.6 |
| SFS | 32.8 | 107.2 | 5.5 | 0.1 | 84.8 | 330.6 |
| CTA | 463.8 | 949.8 | 146.8 | 38.4 | −86.5 | 210.5 |
| QSB* | −56.5 | 45.8 | 153.8 | 11.3 | 68.8 | 69.6 |
| TEO* | −17.1 | 108.6 | −24.2 | 10.7 | 53.3 | 367.4 |
| SHE* | −1048.2 | 1394.2 | −567.6 | 202.6 | 1448.7 | 3171.2 |
| TAN* | −411.1 | 631.4 | 25.2 | 11.1 | 315.6 | 641.8 |
| KNY | −1.6 | 4.5 | −86.6 | 31.7 | −25.9 | 76.1 |
| MID* | −877.2 | 1672 | −297.7 | 71.1 | −909 | 1574.1 |
| SJG | 21.8 | 41.1 | −51.5 | 23.5 | −215.9 | 368.2 |
| VSS* | −50 | 48.2 | 79.6 | 32.4 | 27.6 | 25.8 |
| PIL* | 11.6 | 13.1 | 12.7 | 1.8 | −9.4 | 7.7 |
| KDU | −39.6 | 97.1 | 101.1 | 11.1 | 65.1 | 132.9 |
| CKI | 179.4 | 344.2 | 51.8 | 2.8 | 64.9 | 112.5 |
| HON | 177 | 354.5 | −97.2 | 32 | 309.4 | 495.6 |
| ASC | 389.7 | 697.9 | −344.6 | 151.7 | 55.8 | 101.2 |
| IPM* | −111.6 | 226 | −354.8 | 192 | 990.3 | 1499.4 |
| GUI* | 3056.9 | 12495.6 | 796.2 | 219.3 | 529 | 1593 |
| LNP* | −32.4 | 35.4 | −24.3 | 2.3 | −32.8 | 27.6 |
| GZH* | −286.4 | 315.8 | −226.8 | 14.2 | 1708.9 | 1421 |
| PPT | 915.5 | 1981.6 | 1234.9 | 618.1 | 296.4 | 392.5 |
| API* | −24.3 | 53.3 | −320.1 | 149.1 | 873.6 | 1124.2 |
| PHU* | 5.8 | 6.9 | −9.3 | 0.3 | 90.6 | 66 |
| ABG | 97.8 | 146.4 | −481.1 | 1.5 | −772.2 | 598.1 |
| TAM | −72.4 | 80.9 | 183.8 | 4.7 | 111.2 | 63.4 |
| HYB | −195.8 | 300 | 0.5 | 0 | −265.5 | 186.4 |
| CPL* | 65.7 | 100.9 | −20.8 | 0.3 | 330.6 | 229.7 |

| IAGA code | X_xDLFI | | Y_xDLFI | | Z_xDLFI | |
|---|---|---|---|---|---|---|
| | Δ (nT) | δ (%) | Δ (nT) | δ (%) | Δ (nT) | δ (%) |
| GAN* | 106 | 259.5 | −67.3 | 11.3 | 60.8 | 49.8 |
| BNG* | −185.7 | 460.8 | 38.6 | 2.7 | −105.6 | 76.7 |
| GUA | −157.7 | 399 | −76.4 | 1.2 | −67.1 | 35.9 |
| DLT | 30.8 | 41.6 | 51.1 | 1.1 | −100.6 | 29.9 |
| KOU | −27 | 65 | −36.2 | 29 | −62.5 | 31.5 |
| TTB* | 17.1 | 41.4 | 55.5 | 49.3 | −68.4 | 17.4 |
| MBO | −134.2 | 343.3 | −29.5 | 7.9 | 33.3 | 8.9 |
| AAE* | −719.4 | 1856 | 102.2 | 10.2 | −547.8 | 81.7 |
| HUA* | −23.6 | 60.7 | −4.8 | 1 | 65.3 | 5 |

**Table A8.** Comparison of the model values of the crustal field components according to EMM2017 with the values we obtained (Table A2).

| IAGA code | X_ EMM2017 | | Y_ EMM2017 | | Z_ EMM2017 | |
|---|---|---|---|---|---|---|
| | Δ (nT) | δ (%) | Δ (nT) | δ (%) | Δ (nT) | δ (%) |
| SIT | 42.9 | 104.3 | 7.1 | 5.5 | 10.3 | 87.1 |
| PAF | −481.5 | 235.5 | 115.8 | 87.8 | 247.8 | 600.6 |
| POD* | 107.5 | 60.3 | 81 | 6 | 47.6 | 147.8 |
| BRD* | 24.6 | 63.3 | 138.5 | 31.4 | 60.9 | 548.6 |
| KLI* | −28.1 | 22.3 | 17.1 | 3.7 | 20.7 | 63 |
| LER | 170.9 | 258.2 | −213.3 | 1.9 | 72.7 | 352.9 |
| SPG* | 9.9 | 13.4 | −76 | 22 | 248.9 | 1217.2 |
| NUR* | −281.9 | 392.3 | −2.7 | 0.7 | 227.9 | 1113 |
| YAK* | 32.7 | 23 | 445 | 91.1 | 3647.1 | 11204.2 |
| UPS | 22.2 | 32.4 | −31.5 | 5.9 | 96.3 | 468.8 |
| LOV* | −59.8 | 88.9 | −46.5 | 9 | −47.8 | 232.4 |
| BOX | 87.7 | 78 | 2.5 | 0.5 | 184.2 | 556.8 |
| MGD | 227.8 | 216 | 664.9 | 132.2 | −64.9 | 194.9 |
| NEW | 25.2 | 77.2 | −9.6 | 7.3 | 201.6 | 1779.4 |
| OTT | −133 | 423.6 | 119.7 | 86.4 | −273.2 | 2400.5 |
| ARS* | −161.6 | 138.2 | 3.7 | 0.9 | −94.9 | 287.8 |
| VIC | 10 | 31.8 | 7.2 | 6.4 | 309.3 | 2712.4 |
| CZT | 563.7 | 402.7 | −1000.2 | 909.7 | −161.1 | 372.8 |
| SHU | −361.1 | 1175.1 | 141.1 | 82.9 | −46.7 | 382.3 |
| ESK | 5.2 | 9.4 | 30.7 | 0.6 | 13.8 | 65.6 |
| NVS | −106 | 87.8 | −3.5 | 0.4 | 32.1 | 97.6 |
| MHV* | 682.8 | 680.9 | −460.2 | 93.9 | 281.7 | 842 |

| IAGA code | X_ EMM2017 | | Y_ EMM2017 | | Z_ EMM2017 | |
|---|---|---|---|---|---|---|
| | Δ (nT) | δ (%) | Δ (nT) | δ (%) | Δ (nT) | δ (%) |
| AIA* | −185.1 | 246.8 | 140.5 | 52.5 | −668.1 | 1459.2 |
| HLP | 61.3 | 106.5 | 93.9 | 19.3 | 156.2 | 745.9 |
| STJ | −53.8 | 193.7 | −44 | 47.4 | 96.8 | 831.4 |
| EYR* | 2.7 | 2.3 | 16 | 6.3 | −131.4 | 316.2 |
| WNG | 6.1 | 11.2 | −41 | 5 | 32.1 | 152.1 |
| ORC* | 68.1 | 98.1 | −108.2 | 4.4 | 155.3 | 333.5 |
| AMS* | 604.4 | 441.2 | 653.8 | 348.6 | 2058 | 4986.6 |
| SBL | 2.6 | 9.9 | −0.4 | 0.4 | 2.7 | 22.5 |
| VAL | −97.9 | 197.9 | −68.4 | 6.8 | 90.5 | 422 |
| IRT* | −2.6 | 2.4 | 20 | 1.6 | 123.6 | 372.2 |
| BOU | 75.3 | 282.1 | −60.2 | 31 | 93.7 | 803.9 |
| NGK | 9.5 | 18.3 | −9.9 | 1.6 | 25 | 117.6 |
| BEL | −204.7 | 387.5 | 0 | 0 | −4.5 | 21.3 |
| HAD | 22.7 | 47.2 | 9 | 0.2 | −78 | 362.1 |
| FRD | 0.7 | 2.8 | 36.8 | 27.1 | −92 | 777.3 |
| PET | −38.5 | 50.7 | −331.7 | 57.3 | −184 | 527.2 |
| KEP | 5.2 | 7.4 | 16.7 | 2.8 | 5.6 | 12.1 |
| MAB* | −103.8 | 215.8 | 7.2 | 0.7 | −52.1 | 241.8 |
| DOU | −71 | 149.1 | 13.7 | 1.2 | −25.9 | 119.9 |
| CNB | 23.7 | 30.1 | −96.2 | 27.5 | −14.8 | 43.2 |
| BDV* | 42.8 | 90.5 | −19 | 3.4 | 21.5 | 99.2 |
| BFO* | −3.7 | 8.2 | 9.9 | 1.3 | −3.9 | 17.8 |
| FUR* | 1.5 | 3.3 | 6.1 | 1 | −21.9 | 100.3 |
| HRB | −7.4 | 16 | 39.8 | 8.3 | 88.5 | 406.5 |
| WIC | −18 | 39.2 | 2.2 | 0.4 | −21.9 | 100.3 |
| CLF | 52.1 | 117.6 | −24 | 1.7 | −41.6 | 189.6 |
| NCK* | 0.5 | 1.2 | −30.4 | 6.1 | −9.1 | 41.5 |
| GNA | 110.8 | 145.6 | 29.6 | 1 | −64.2 | 186.7 |
| HER | −13.1 | 9.7 | −9.3 | 3.5 | 2.3 | 3.9 |
| FRN | 110 | 486.8 | 27.8 | 27 | 147.3 | 1209 |
| GNG | 51.3 | 68.5 | 7.8 | 0.3 | 16.7 | 48.5 |
| THY | −17.3 | 38.7 | 4.1 | 0.8 | 7.5 | 34.3 |
| TDC* | 384 | 392.2 | −534.4 | 219.7 | 447.9 | 1048.1 |
| KHB | 267.6 | 365.9 | 449.7 | 131.4 | −533.3 | 1509.9 |
| LON* | 9 | 21.2 | −1.4 | 0.3 | −30.4 | 136.7 |
| PST | −1.8 | 3 | 11.8 | 0.8 | 42.3 | 84.6 |
| BSL* | −41.9 | 201.4 | 12 | 1.8 | −67.3 | 541.1 |

| IAGA code | X_ EMM2017 | | Y_ EMM2017 | | Z_ EMM2017 | |
|---|---|---|---|---|---|---|
| | Δ (nT) | δ (%) | Δ (nT) | δ (%) | Δ (nT) | δ (%) |
| SUA* | 41.7 | 97.9 | 50.3 | 13 | 88.7 | 399.7 |
| GCK* | 44.7 | 106.9 | 46.6 | 10.7 | 70.7 | 316.8 |
| AAA* | −51.6 | 71.1 | 31.8 | 3.9 | 283.3 | 804.3 |
| TUC | 102.1 | 493.3 | 193.1 | 150.1 | −389.4 | 3113.6 |
| DLR* | −73.1 | 365.8 | −71.2 | 30.3 | 0.7 | 5.3 |
| PAG* | 190.6 | 481.7 | 165.4 | 41.6 | 251.4 | 1107.3 |
| MMB | 206.6 | 441.6 | −75.9 | 27.3 | −84.6 | 295.5 |
| KMH* | 30.3 | 23.5 | 30.1 | 7.4 | −163.4 | 286.8 |
| GLK* | 99.8 | 64 | 209.2 | 15.8 | 371.2 | 418.2 |
| AQU* | 15.6 | 40.8 | 6.3 | 1.2 | −24 | 104.3 |
| HBK* | −67 | 57.5 | 20.1 | 6.2 | −43.2 | 73.9 |
| DUR* | −11.3 | 30.1 | 1.9 | 0.4 | 14.2 | 61.3 |
| IZN* | −73.1 | 193.4 | −31.3 | 8.7 | 3.8 | 16.7 |
| BMT* | −309.6 | 213.6 | 646.1 | 58.9 | −197.7 | 236.1 |
| EBR | −11 | 31.1 | 43.8 | 3.1 | −7.3 | 31 |
| ASP | 5.6 | 10.1 | −1.4 | 0.2 | −26.9 | 70.5 |
| SPT | −27.3 | 81.7 | 16.6 | 0.2 | 14.9 | 61.4 |
| PEG* | 36.8 | 106.9 | −2 | 0.5 | −15.5 | 64.4 |
| LRM | 51.9 | 95.5 | 1.8 | 0 | −131 | 341.5 |
| TRW* | 31.2 | 31.2 | 78.3 | 2.7 | −129.8 | 127.5 |
| LZH* | −35.5 | 27.4 | 22.6 | 0.9 | 76.8 | 88 |
| TSU* | −33.5 | 31.4 | 25.4 | 3.7 | −92.3 | 155.7 |
| CYG | 56.5 | 46.3 | −39.9 | 4.9 | 52.8 | 58.4 |
| KAK | −37.9 | 98.8 | −23.7 | 8.7 | 50.3 | 158.5 |
| SFS | −15 | 49.1 | 45.8 | 0.6 | 63.2 | 246.5 |
| CTA | 424.3 | 868.8 | 28 | 7.3 | −99.8 | 242.8 |
| QSB* | −65.4 | 53.1 | 139.8 | 10.3 | 93.8 | 94.9 |
| TEO* | 16.2 | 102.4 | −13.1 | 5.8 | 110.1 | 759.2 |
| SHE* | −1004.2 | 1335.6 | −521.9 | 186.3 | 1451.5 | 3177.5 |
| TAN* | −282 | 433.2 | 36.9 | 16.3 | 179.2 | 364.4 |
| KNY | 31.7 | 90.5 | −89.7 | 32.8 | 45.3 | 133 |
| MID* | −854 | 1627.7 | −246.7 | 58.9 | −970.5 | 1680.6 |
| SJG | −17.7 | 33.4 | −111.1 | 50.7 | 9.4 | 16 |
| VSS* | 25.5 | 24.5 | 48.8 | 19.8 | 60.8 | 56.8 |
| PIL* | −36.3 | 41.1 | 33.9 | 4.7 | 1.3 | 1.1 |
| KDU | 2.7 | 6.6 | 25.2 | 2.8 | 4.8 | 9.9 |
| CKI | 231.3 | 443.7 | 102 | 5.5 | 187.8 | 325.6 |

| IAGA code | X_ EMM2017 | | Y_ EMM2017 | | Z_ EMM2017 | |
|---|---|---|---|---|---|---|
| | Δ (nT) | δ (%) | Δ (nT) | δ (%) | Δ (nT) | δ (%) |
| HON | 140.5 | 281.4 | −50 | 16.5 | 398.5 | 638.4 |
| ASC | 542.3 | 971.2 | −300.5 | 132.3 | −11.7 | 21.2 |
| IPM* | −65 | 131.7 | −210.3 | 113.8 | 581.2 | 879.9 |
| GUI* | 3037.8 | 12417.6 | 710.4 | 195.6 | 546.8 | 1646.9 |
| LNP* | −12.5 | 13.6 | −70.7 | 6.7 | −43.9 | 37 |
| GZH* | −424.2 | 467.7 | −223.2 | 14 | 1571.4 | 1306.7 |
| PPT | 928.8 | 2010.3 | 978.5 | 489.8 | 475.3 | 629.2 |
| API* | 88 | 193.1 | −339.4 | 158.1 | 781.3 | 1005.4 |
| PHU* | −23 | 27 | −18.6 | 0.7 | 31.2 | 22.7 |
| ABG | 100.3 | 150.1 | −393 | 1.2 | −704.1 | 545.4 |
| TAM | −50.1 | 56 | 163.1 | 4.2 | 2.9 | 1.7 |
| HYB | −188.5 | 288.8 | 79.7 | 1.1 | −573 | 402.3 |
| CPL* | −59.6 | 91.4 | 73.6 | 1.1 | 89.9 | 62.5 |
| GAN* | 121.3 | 296.9 | −55.4 | 9.3 | 13 | 10.6 |
| BNG* | −99.5 | 247 | −163.3 | 11.3 | −19.3 | 14 |
| GUA | −137.1 | 347 | −80.6 | 1.3 | 3.3 | 1.7 |
| DLT | 63.5 | 85.7 | 72.5 | 1.6 | −67.6 | 20.1 |
| KOU | −131 | 315.2 | −122.9 | 98.5 | −104.4 | 52.6 |
| TTB* | 6.8 | 16.4 | 26.9 | 23.9 | −26.2 | 6.6 |
| MBO | −71.5 | 182.8 | −30.1 | 8 | −77.5 | 20.6 |
| AAE* | −725.6 | 1872 | 106.2 | 10.6 | −564.8 | 84.2 |
| HUA* | −18.1 | 46.7 | 33.7 | 7.1 | −30.7 | 2.4 |

**Figure A1.** Variations of the monthly means of the residual field relative to the medians over 1998-2025: *X* component (left panel), *Y* component (center panel) and *Z* component (right panel); data gaps are marked in yellow. The observatories are sorted by decreasing quasi-dipole geomagnetic latitude.

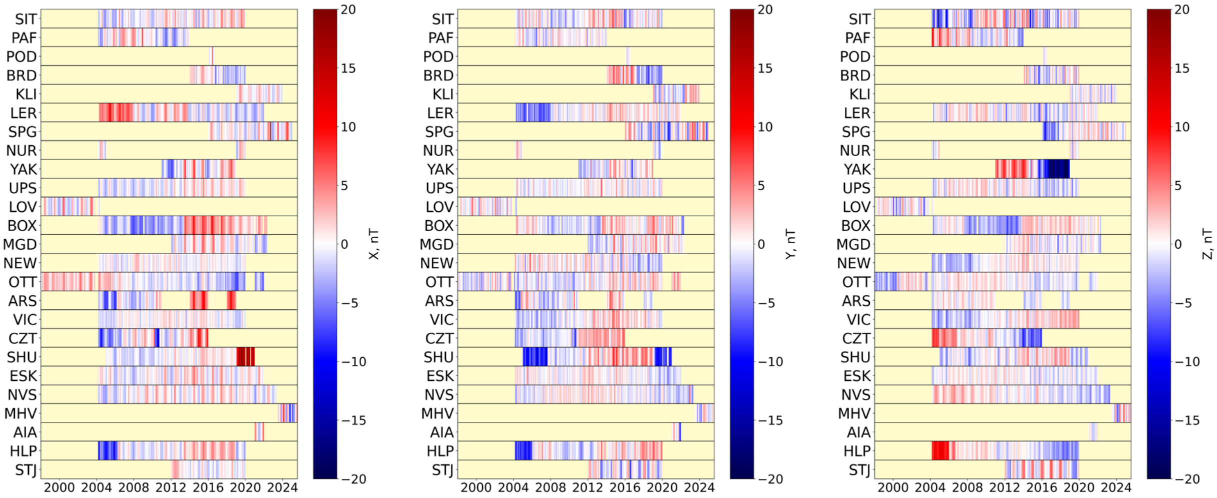


(continued)

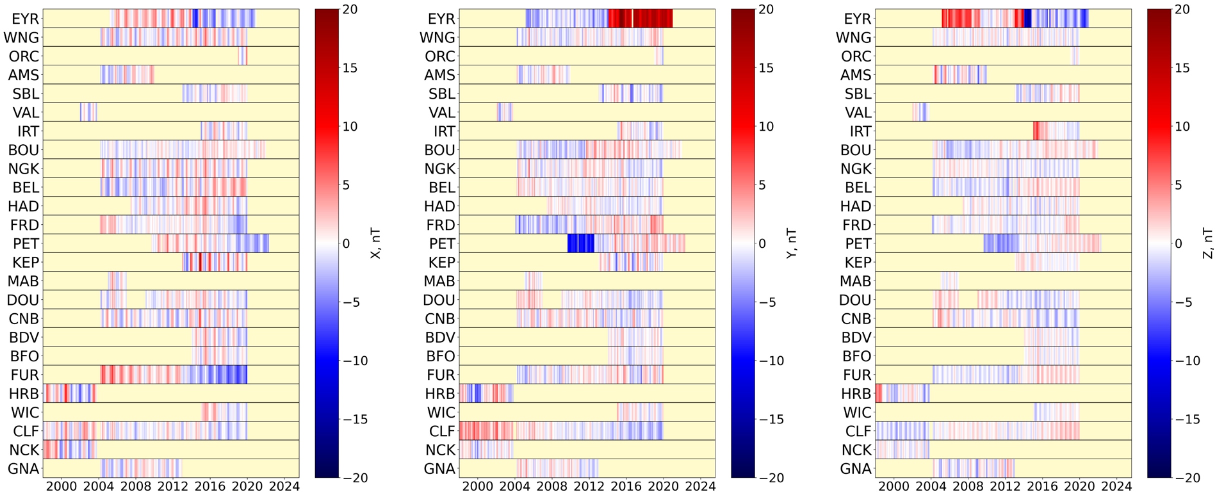


(continued)

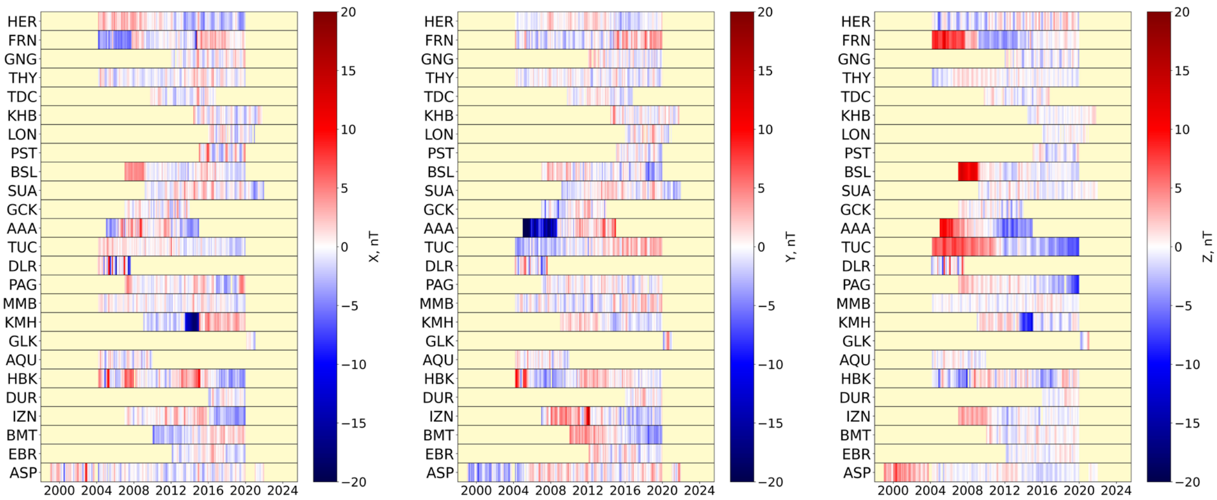

(continued)

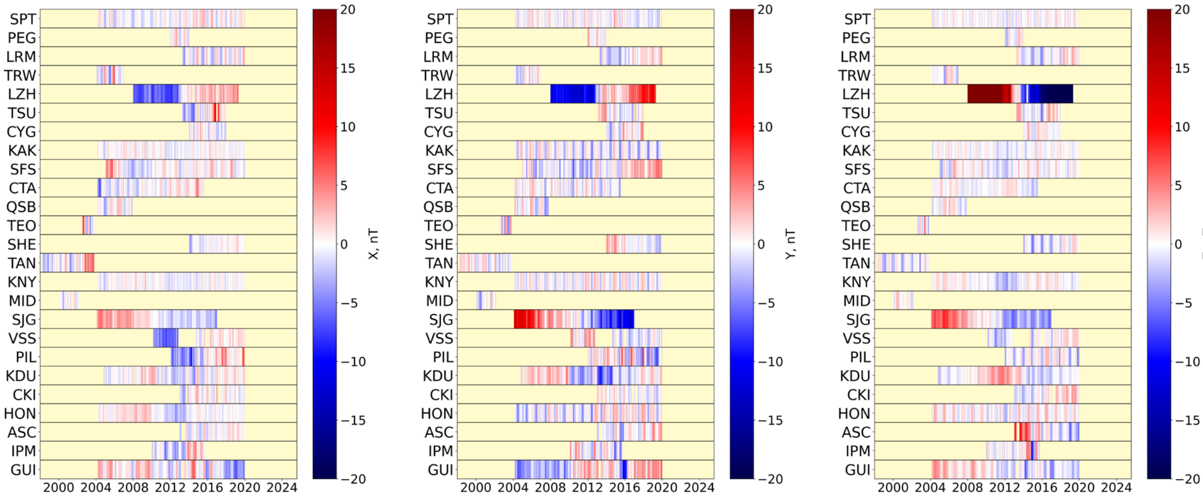


(continued)

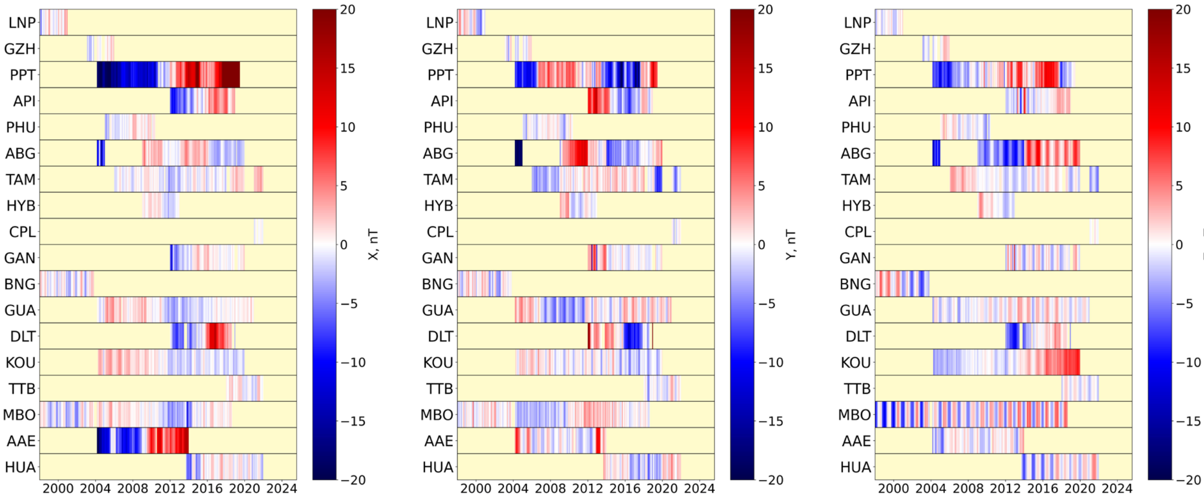


***CORRESPONDING AUTHOR: Mikhail NANOV**,
Geophysical Monitoring Sector, Geophysical Center of the Russian Academy of Sciences, Moscow, Russian Federation
e-mail: m.nanov@gcras.ru